Bralower, T.J., Premoli Silva, I., Malone, M.J., et al., 2002
Proceedings of the Ocean Drilling Program, Initial Reports Volume 198

8. Site 1212[1]

Shipboard Scientific Party[2]

PRINCIPAL RESULTS

Background

Site 1212 is located in middle bathyal (2681 m) water depth on the southern flank of the Southern High of Shatsky Rise. The site is at the location of Deep Sea Drilling Project (DSDP) Site 47 (Fischer, Heezen, et al., 1971). Hole 47.2 was cored with rotary core barrel (RCB) penetrating 129.2 m of predominantly soft sediments, which frequently were so fluid that cores could not be easily opened. The hole terminated at a hard layer interpreted as chert. The recovered sediments, mainly nannofossil ooze and chalk are Pleistocene to late early Maastrichtian in age. Site 1212 also lies ~1.3 km to the northwest of DSDP Site 577.

According to the drilling record from Hole 47.2 (Fischer, Heezen, et al., 1971), the uppermost seismic reflector correlates with a major unconformity between the upper Miocene and the lower Oligocene. The next highest reflector corresponds to the uppermost chert horizon in the Maastrichtian. The interval between the two reflectors contains a Paleogene to uppermost Cretaceous section with minor unconformities. The lower Eocene to the Cretaceous/Tertiary (K/T) boundary section in Hole 47.2 was apparently complete and included the Paleocene/Eocene (P/E) boundary. The K/T boundary was described as heavily disturbed by coring, but the described planktonic foraminiferal faunal succession was complete (Douglas, 1971). Abundant fragments of *Inoceramus* shells were recorded from the highly disturbed nannofossil ooze in the lowermost core taken (Core 47.2-14; 128.0 to 129.2 meters below seafloor [mbsf]). Stable isotope analyses on single planktonic species have been performed on samples from this site and from other Shatsky Rise sites including Sites 305 and 306, and the first paleotemperature curves for the Northern Pacific were constructed for the entire Pleistocene to Cretaceous interval (Douglas and Savin, 1971, 1975). Paleo-

[1]Examples of how to reference the whole or part of this volume.
[2]Shipboard Scientific Party addresses.

Ms 198IR-108

cene–Eocene Thermal Maximum (PETM) excursion isotope values were identified on single specimen and multispecimen analyses of foraminifers from Hole 47.2 by Stott (1992). This interval was described as highly disturbed by drilling.

Site 1212 is the third shallowest site in the Shatsky Rise depth transect. The site is ~300 m deeper than Site 1209 (2387 m) and 230 m shallower than Site 1211, the deepest site drilled on the Southern High; Central High Site 1208 at 3346 m is ~670 m deeper then Site 1212. The objective at Site 1212 was to recover a complete and undisturbed record of the Hole 47.2 sequence with advanced piston corer (APC) double coring. As part of the Shatsky Rise depth transect, drilling at Site 1212 addresses a number of leg-related objectives.

Holes 1212A and 1212B were cored with the APC. Hole 1212A terminated at 101.6 mbsf at the uppermost chert layer in the upper Maastrichtian. In Hole 1212B, 11 chert layers were penetrated with XCB center bit drilling and a total of 207.6 mbsf was cored, reaching the upper Albian.

Summary of Results

Coring at Site 1212 recovered three lithologic units that have been separated based on sediment composition and color variation (Fig. **F1**). Lithologic Unit I ranges from Holocene to middle Miocene (0 to ~15.1 Ma; 0–63.0 mbsf) and consists of nannofossil ooze with clay, clayey nannofossil ooze with foraminifers, and clayey nannofossil ooze, light gray to light olive gray in color. This unit has a higher clay content than underlying units. Two subunits are distinguished. Subunit IA (Holocene to upper Pliocene; 0 to ~3 Ma; 0–35.9 mbsf) is characterized by interbedded light gray nannofossil ooze with clay and light olive-gray clayey nannofossil ooze with foraminifers expressed as decimeter-scale light/dark alternations. The clay and foraminiferal content varies from 5% to 35% and from 0% to 32%, respectively. Minor components include siliceous microfossils (diatoms, radiolarians, silicoflagellates, and sponge spicules) and rare ash layers. Subunit IB (upper Pliocene to middle Miocene; ~3 to ~15.1 Ma; 35.9–63.0 mbsf) consists of light gray nannofossil ooze with clay and light olive-gray clayey nannofossil ooze and contains subtler decimeter-scale light/dark alternations. Siliceous microfossils are present but considerably rarer than in Subunit IA. Ash layers are absent.

An unconformity from middle Miocene to lower middle Eocene separates lithologic Unit I from Unit II (see **"Biostratigraphy,"** p. 56, in "Special Syntheses" in the "Leg 198 Summary" chapter). Lithologic Unit II ranges from lower middle Eocene to lowermost Paleocene (~43.6 to 65 Ma; 63.0–102.2 mbsf) and consists of alternating pale yellowish brown nannofossil ooze with clay and pale orange to grayish orange nannofossil ooze (Subunit IIA; lower middle Eocene to the P/E boundary; 43.6 to 55.5 Ma; 63.0–79.9 mbsf), and very pale yellowish brown nannofossil ooze with clay interbedded with very pale orange nannofossil ooze (Subunit IIB: P/E boundary to K/T boundary; 55.5 to 65.0 Ma; 79.9–102.2 mbsf). A number of minor diastems occur in this interval as indicated by thin, darker horizons.

Lithologic Unit III ranges from uppermost Maastrichtian to upper Albian (65 to ~100 Ma; 102.2–207.6 mbsf) and consists of soft, white nannofossil ooze and nannofossil ooze with foraminifers interbedded with chert. The unit has extremely high carbonate content and is frequently highly disturbed by drilling because of its fluid nature. Eleven chert lay-

F1. Coring results, p. 30.

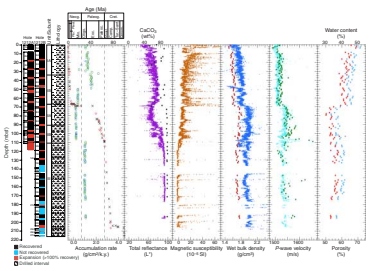

ers were penetrated. Two significant unconformities are found toward the base of this unit, separating the upper Campanian from the Coniacian and the Coniacian from the upper Albian.

The Site 1212 stratigraphic section shows broad similarity to the sections recovered at previously drilled Sites 1209–1211 suggesting, in general, common sedimentation histories. In particular, the critical boundaries, the P/E and K/T, show a similar sequence of lithologies. In addition, sedimentation rates throughout the Site 1212 section are generally comparable with the rates estimated at Sites 1209 and 1210, whereas they are higher than at Site 1211 in certain intervals (e.g., Paleocene–Campanian) (Figs. F2, F3). The major difference is the ~30-m.y. unconformity between lithologic Units I and II, a gap that is longer in duration than the major Neogene–Paleogene unconformity at other Southern High sites. Additional unconformities and condensed intervals in the Site 1212 section may be located in shore-based biostratigraphic investigations.

Highlights

The stratigraphic record at Site 1212 reveals differences from the records at Sites 1209, 1210, and 1211 that are not related to water depth. For example, the major Miocene–Eocene unconformity spans the lower Oligocene through mid-middle Eocene, an interval largely preserved at the other sites, including Site 1211, which is situated 230 m deeper than Site 1212. This suggests that the missing section at Site 1212 is not a result of dissolution. The site lies near the top of a canyon and in an area of the Southern High where the stratigraphy is complex (Sliter and Brown, 1993). Thus, it is possible that mass wasting has removed part of the section in the vicinity of Site 1212.

The major highlight of coring at Site 1212 is similar to the highlights at Sites 1209, 1210, and 1211—namely, the recovery of all of the critical intervals, most in both holes. One exception is the Eocene/Oligocene (E/O) boundary, which lies within the Miocene–Eocene unconformity. Although coring of Cretaceous sediments was limited, the results from Site 1212 are meaningful with regard to the geologic history of Shatsky Rise.

Recovery of Critical Events

Coring at Site 1212 recovered the PETM, the biotic event in the mid-Paleocene, the K/T boundary, and the mid-Maastrichtian deepwater event (MME). The PETM at Site 1212 is lithologically similar to Sites 1209 and 1210, corresponding to a 9-cm interval of yellowish brown clayey nannofossil ooze. This lithology has a sharp contact with underlying pale orange nannofossil ooze, and a gradational contact with overlying pale orange nannofossil ooze. Preliminary biostratigraphic investigation suggests that the sequence is similarly expanded to the Sites 1209 and 1210 PETM sections and that similar changes in assemblages and microfossil preservation occur within the event. For example, the abundance of *Fasciculithus* decreases sharply near the onset of the event, and excursion foraminifers (e.g., Kelly et al., 1996) have been observed. The base of the PETM event, however, appears to correspond to an unconformity. Foraminifers in Sample 198-1212B-9H-5, 77–78 cm, include *Globanomalina pseudomenardii,* the last occurrence (LO) of which defines the top of Zone P4 at 55.9 Ma, ~0.4 m.y. before the onset of the event. The significance of this unconformity in terms of stratigra-

F2. Age-depth curves based on shipboard biostratigraphy, Sites 1209–1212, p. 31.

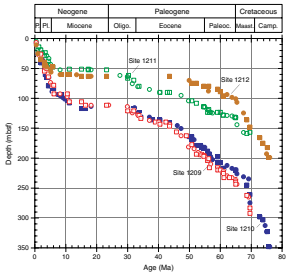

F3. Summary of lithostratigraphy, Sites 1207–1214, p. 32.

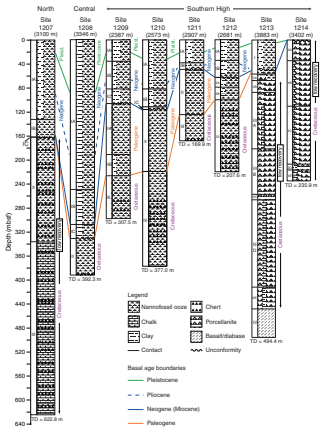

phy and paleoceanographic interpretation of the PETM is currently not understood.

The mid-Paleocene event was recovered in Hole 1212B. The event appears to be slightly more expanded than at other sites although the sediments in this interval are considerably lighter in color than the equivalent interval elsewhere. As at the other sites, this interval is characterized by dissolved nannofloras and planktonic foraminiferal assemblages as well as an abundance of phillipsite and fish teeth. The first occurrence (FO) of the nannolith *Heliolithus kleinpellii* lies within the event that also corresponds to a nearly monogeneric planktonic foraminiferal assemblage of *Igorina*.

The K/T boundary interval is lighter in color than at the other sites, and the sediments near the boundary appear to be somewhat less indurated. Ooze immediately underlying the boundary correlates to uppermost Maastrichtian nannofossil Zone CC26 based on the presence of *Micula prinsii*. The paleontological boundary has been bioturbated, and careful sampling of burrows of lowermost Danian sediment that extend 10 cm into the uppermost Maastrichtian yields ~100-µm-sized, amber to olive-green spherules as well as tiny planktonic foraminifers possibly representing basal Paleocene Zone P0. Planktonic foraminifers in the lowermost Danian correspond to Zone Pα. The identical faunal and floral changes are observed in the boundary interval as at the other sites, and the lower Danian interval, in particular, appears rather expanded and remarkably undisturbed.

Site 1212 is located close to Site 577 where the K/T boundary was triple cored during Leg 86 (i.e., Wright et al., 1985). Lithologically, the K/T boundary recovered in Holes 577, 577A, and 577B are similar although not identical to the Site 1212 record. The main difference between the sections is the degree of bioturbation and thickness of the bioturbated layer, and the thickness and color of the lowermost Paleocene foraminiferal ooze layer. Lighter color is associated with an increase in thickness of the basal layer from 10 cm in Hole 577A to more than 15 cm in Hole 577. Smear slide analysis for Site 577 showed that planktonic foraminifers are abundant (up to 35%) from basal Paleocene to ~60–70 cm above the K/T, whereas above and below this interval they rarely exceed 1%. At Site 1212, abundant foraminifers are found in smear slides only in the lowermost 10–20 cm of the Paleocene.

A detailed study of planktonic foraminiferal biostratigraphy and assemblages across the K/T boundary at Site 577 was conducted by Gerstel et al. (1986). These authors illustrated the same evolutionary trends and succession of events as found at Site 1212 and other Leg 198 sites. Gerstel et al. (1986) argued that the presence of *Parvularugoglobigerina eugubina* below the K/T boundary was evolutionary. However, we have noticed that (1) the distribution of *P. eugubina* below the boundary is confined to the burrows associated with tektite-like spherules and (2) it is preceded in the deepest burrows by the tiny *Guembelitria* assemblage reminiscent of the P0 zonal fauna. Moreover, the Site 1212 record shows that the tektite-like spherules are concentrated in the first few centimeters (2–3 cm) above the K/T boundary, and their record above is related to the intense burrowing. Nannofossil assemblages across the boundary at Site 577 were described in detail by Monechi (1985), who documented a similar sequence of events to that found at Site 1212 and other Leg 198 sites.

Cretaceous History of the Southern High

The Maastrichtian–Campanian section at Site 1212 is underlain by a thin layer of clay and glauconite-rich ooze of Coniacian age (planktonic foraminiferal Zone KS23; top of Section 198-1212B-24H-6), which in turn is underlain by ooze of late Albian age (Zones KS 16–17; base of Section 198-1212B-24H-6 to Section 27H-CC). Albian sediment has been recovered at a number of other sites on Shatsky Rise, including Sites 1207 and 1213 and DSDP Sites 305 and 306 (Luterbacher, 1975). Coniacian to upper Cenomanian sediment, however, is extremely rare on Shatsky Rise as noted by Sliter (1992), who also reevaluated the planktonic foraminiferal biostratigraphy of Site 305 and found an unconformity in this interval. Sliter (1992) proposed that the Coniacian to Cenomanian interval was widely unconformable as a result of deep-sea erosion or dissolution. Coring results from Site 1212 and other Leg 198 sites confirm this conclusion. The fact that the one site where the Cenomanian to Coniacian interval is partially recovered, Site 1207 on the Northern High, lies at greater depth (3101 m) than Sites 1212 and 305 (2903 m) where it is unconformable, suggests that erosion is the likely cause of the regional unconformity. In addition, seismic line TN037-17A, which crosses Sites 1209, 1210, and 1211, shows a prominent unconformity (Reflector R1) that likely correlates to the Cenomanian to Coniacian interval, where mid-Cretaceous dipping horizons are cut by horizontal uppermost Cretaceous horizons (see lines 14A and 17A in oversized Figure F8, p. 14, in Klaus and Sager, this volume). Thus, the stratigraphy of Site 1212 has important implications for the Cretaceous history of Shatsky Rise.

BACKGROUND AND OBJECTIVES

Site 1212 is located at 2682.5 m water depth on the southwestern flank of the Southern High of Shatsky Rise. The site is located close to DSDP Site 47. Thus, the stratigraphic sequence is known, although significant disturbance in Cenozoic and Upper Cretaceous sediments resulting from RCB drilling at Site 47 has blurred the signal of short-term events, such as the PETM and the K/T boundary.

The drilled sequence in Hole 47.2 had a total depth of 129.2 m and reached the upper Maastrichtian. The site contains a relatively thick lower–middle Eocene to uppermost Maastrichtian section (Fischer, Heezen, et al., 1971). This section was an integral part of the data set used by Douglas and Savin (1971) to derive one of the first late Maastrichtian to Cenozoic paleotemperature curves. A major unconformity was found between the upper Miocene and the upper–lower Eocene. Other, more minor unconformities may exist in the section, but they are difficult to detect because of the major drilling disturbance present in the section. Biostratigraphic results from Hole 47.2 (e.g., Douglas, 1971) suggest a reasonably continuous sequence across intervals such as the K/T boundary.

Site 1212 is in the middle of the Shatsky Rise depth transect. The shallowest site, 1209 at 2387 m, is ~300 m shallower than Site 1212; the deepest site, 1208 at 3346 m, is ~670 m deeper. The goal at Site 1212 was to recover with double APC coring a complete and undisturbed record of the Site 47 sequence. As part of this depth transect, drilling at Site 1212 addresses a number of leg-related objectives. The sediments recovered at this site will be used to

1. Reconstruct changes in the properties of surface and deepwaters and vertical gradients through the Cretaceous and Paleogene using biotic and stable isotope studies;
2. Determine long-term climate changes during the onset and demise of the Cretaceous "greenhouse" and the onset of Antarctic glaciation in the Eocene;
3. Shed light on the nature of chemical (i.e., calcite compensation depth [CCD], nutrients, and oxygenation) and physical oceanographic changes (temperature gradients) during transient climatic events such as the E/O boundary, the PETM, late Paleocene and early Eocene hyperthermals, and the MME;
4. Determine fluctuations in the CCD through time and interpret them in a paleoceanographic framework;
5. Improve understanding of the origin of orbital cycles in the sedimentary record using geochemical and biotic data; and
6. Improve Cretaceous and Paleogene timescales by including correlations between the geomagnetic polarity timescale and low-latitude biostratigraphies.

OPERATIONS

Transit from Site 1211 to Site 1212

The short transit (28 nmi) to Site 1212 was completed in 3.2 hr at an average speed of 8.8 kt. At 0955 hr on 29 September 2001, the ship was switched over to dynamic positioning mode, initiating operations at Site 1212.

Site 1212

Hole 1212A

An APC/extended core barrel (XCB) bottom-hole assembly (BHA) was run to 2689.0 meters below rig floor (mbrf), and Hole 1212A was spudded with the APC at 1540 hr on 29 September. The mudline core recovered 4.96 m of sediment, indicating a seafloor depth of 2693.6 mbrf, or 2682.5 meters below sea level (mbsl). APC coring advanced the hole to 101.6 mbsf with 115.1% recovery (Table T1). Cores 4H through 13H were oriented. After an incomplete stroke on Core 13H, we terminated coring in Hole 1212A. The drill string was recovered to the seafloor at 0255 hr on 30 September, ending operations at Hole 1212A.

T1. Coring summary, p. 63.

Hole 1212B

The ship was offset 15 m to the north and the bit was positioned at a depth of 2689.0 mbrf. The same bit position was used in an attempt to keep critical intervals from falling at core breaks. Hole 1212B was spudded at 0345 hr on 30 September, recovering 6.74 m and establishing a seafloor depth of 2691.8 mbrf, or 2680.6 mbsl. Continuous APC coring progressed to 101.2 mbsf. Cores 4H through 12H were oriented. After an incomplete stroke on Core 12H, we adopted a strategy of deploying the XCB center bit to drill through chert layers, followed by redeployment of the APC. Ten deployments of the XCB center bit were required, including three to penetrate a layer at ~136 mbsf, drilling through 14.8 m to obtain 13 additional APC cores. Total APC recovery for Hole

1212B was 93.6%. Because of the increasing frequency of chert layers and diminishing core recovery on the last three APC cores, we terminated coring at Hole 1212B at 207.6 mbsf. The drill string was retrieved, clearing the rig floor at 2330 hr on 1 October, which concluded operations at Site 1212.

LITHOSTRATIGRAPHY

Description of Lithologic Units

Site 1212 is located in the approximate vicinity of DSDP Site 47.2 and within 1.5 km of DSDP Site 577. The site was drilled in a water depth of 2681 m. The 207.6 m of sediment recovered from Holes 1212A and 1212B is primarily Upper Cretaceous and Cenozoic nannofossil ooze and clayey nannofossil ooze that are entirely pelagic in character. Nannofossils are the major constituent, with variable amounts of clay and foraminifers. In general, there are subtle downhole trends of an increase in the carbonate content and oxidation of sediment. Despite the relatively uniform character of the sediment, the sequence is subdivided into three major lithologic units on the basis of variations in physical properties and sediment composition (Fig. F4). Unit I is light gray (N7) nannofossil ooze with clay that is interbedded with light olive-gray (5Y 6/1) to olive-gray (5Y 4/1) clayey nannofossil ooze. The unit extends from the sediment-water interface to a major Paleogene–Neogene unconformity at 61.3 mbsf in Hole 1212A. Unit II consists of pale yellowish brown (10YR 6/2) nannofossil ooze with clay to grayish orange (10YR 7/4) and very pale orange (10YR 8/2) nannofossil ooze that extends from 61.3 mbsf to the K/T boundary at 101.4 mbsf in Hole 1212A. Unit III encompasses uniform white (N9) to very pale orange (10YR 8/2) nannofossil ooze from 101.4 mbsf to the base of the drilled section at 207.6 mbsf in Hole 1212B. Units I and II are further subdivided on the basis of minor variations in sediment composition and color. The Site 1212 unit and subunit boundaries are nearly identical to those selected for DSDP Site 577 (Heath, Burckle, et al., 1985).

F4. Core recovery, lithology, lithologic units, age with corresponding biostratigraphic zonations, color reflectance, and percent carbonate, Hole 1212B, p. 33.

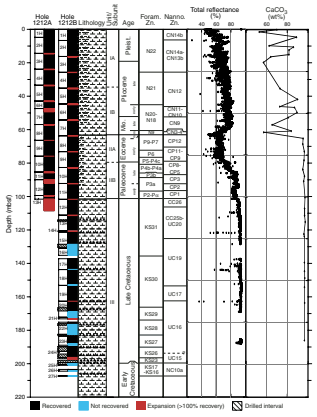

Lithologic Unit I

Intervals: 198-1212A-1H-1, 0 cm, through 8H-3, 150 cm, and 198-1212B-1H, 0 cm, through 7H-7, 6 cm
Depths: 0.0 to 61.3 mbsf in Hole 1212A and 0.0 to 63.26 mbsf in Hole 1212B
Age: Holocene to middle Miocene

Subunit IA

Unit I is subdivided into two subunits (Fig. F4). Subunit IA (0 to 29.78 mbsf [Hole 1212A] and 0 to 35.2 mbsf [Hole 1212B]; Sections 198-1212A-1H-1 to 4H-3, 133 cm, and Sections 198-1212B-1H-1 to 5H-1, 0 cm; Holocene to upper Pliocene) is light gray (N7) nannofossil ooze with clay that is interbedded with a light olive-gray (5Y 6/1) and olive-gray (5Y 4/1) clayey nannofossil ooze with foraminifers. In addition to nannofossils (50%–80%), the sediment contains subordinate amounts of clay (5%–35%) and foraminifers (0%–32%) (see **"Site 1212 Smear Slides,"** p. 70). The percentage of nannofossils in this subunit generally increases downhole, whereas the percentage of foraminifers decreases. Minor biogenic components include diatoms (0%–5%), radiolarians

(0%–5%), silicoflagellates (0%–2%), and sponge spicules (0%–2%) (Fig. F5). Nonbiogenic components include Fe oxides, quartz, volcanic glass, feldspar, and mica. Carbonate content averages 72 wt% and varies from 53 to 89 wt% (Fig. F4). Cycles are expressed as decimeter-scale light/dark alternations with high-amplitude and high-frequency variation in color reflectance that correspond with similar frequency rhythms in magnetic susceptibility and bulk density (see "Physical Properties," p. 23). In general, total color reflectance (L*) increases downhole as carbonate content increases (Fig. F4). The red/blue ratio, however, is low (~1.3) and relatively constant with depth (Fig. F6). Lithologic contacts are mostly gradational and highly bioturbated. Bioturbation within beds is rare to moderate. Pyritized burrow fills and blebs are rare to common throughout the subunit as are green diagenetic bands/laminae. Volcanic ash layers are restricted to Subunit IA. There are few distinct ash beds in this unit, and Section 198-1212A-4H-7 contains a single large (~1.5 cm) pumice fragment.

Subunit IB

Subunit IB (29.78 to 61.3 mbsf [Hole 1212A] and 35.2 to 63.26 mbsf [Hole 1212B]; Sections 198-1212A-4H-3, 133 cm, through 8H-3, 150 cm, and 198-1212B-5H-1, 0 cm, through 7H-7, 6 cm; upper Pliocene to middle Miocene) consists of alternating very light gray (N8) nannofossil ooze with clay and light olive-gray (5Y 6/1) clayey nannofossil ooze. This subunit is distinguished from Subunit IA by higher average carbonate content and less pronounced cycles. In addition to nannofossils (69%–85%), sediment constituents include clay (8%–25%), foraminifers (1%–10%), radiolarians (0%–5%), diatoms (0%–2%), and sponge spicules (0%–1%). Other minor components include Fe oxides, quartz, volcanic glass, feldspar, mica, and opaque minerals. The average carbonate content is 82 wt%, with variations from to 73 to 89 wt%. The light/dark alternations (decimeter scale) are more subtle than in Subunit IA (Fig. F7). Total color reflectance averages 75%. The red/blue color reflectance ratio is relatively constant at 1.3 until the lower part of the subunit (~55 mbsf), where it rapidly increases to 2.5. This increase in the red/blue ratio is analogous to the Subunit IA/IB boundary at Sites 1207, 1208, 1210, and 1211. The amplitude of the high-frequency cycles in total reflectance is lower than it is in Subunit IA. Bioturbation is rare to moderate. Rare pyritized burrow fills and green diagenetic bands are restricted to the upper portion of Subunit IB. Some burrows are filled with foraminifer-rich sediment.

Lithologic Unit II

Intervals: 198-1212A-8H-3, 150 cm, through 12H-CC, 6 cm, and 198-1212B-7H-6, 0 cm, through 11H-7, 24 cm
Depths: 61.3 to 101.4 mbsf in Hole 1212A and 63.26 to 101.44 mbsf in Hole 1212B
Age: early middle Eocene to K/T boundary

The boundary between Units I and II was placed at the base of a middle Eocene/middle Miocene unconformity in Section 198-1212B-7H-6. This unconformity coincides with an abrupt shift in both bulk density and magnetic susceptibility values (Figs. F26, F33). Unit II is further distinguished from Unit I by a higher average carbonate content. Unit II has been subdivided into two subunits.

F5. Estimates of biosiliceous material, Hole 1212A, p. 34.

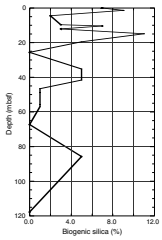

F6. Color reflectance ratio, Holes 1212A and 1212B, p. 35.

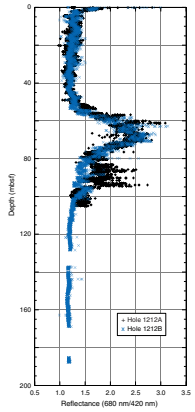

F7. Color reflectance, Cores 198-1212B-3H and 5H, p. 36.

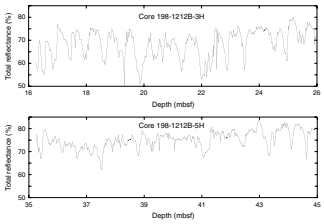

Subunit IIA

Subunit IIA (61.3 to 76.54 mbsf [Hole 1212A] and 62.3 to 81.43 mbsf [Hole 1212B]; Sections 198-1212A-8H-3, 150 cm, through 10H-1, 64 cm, and 198-1212B-7H-7, 6 cm, through 9H-5, 73 cm; lower middle Eocene to P/E boundary) consists predominantly of pale yellowish brown (10YR 6/2) nannofossil ooze with clay alternating with pale orange to grayish orange (10YR 7/4) nannofossil ooze. There are a few 1-cm-thick layers of moderate yellowish brown (10YR 5/4) clayey nannofossil ooze. The average carbonate content in Subunit IIA is 82 wt%. Minor components include clay (~3%–10%), foraminifers (0%–7%), and radiolarians (0%–1%). Other minor components (0%–4%) include feldspar, volcanic glass, and opaque minerals. A prominent clay-rich layer (~35%) is present in Section 198-1212A-8H-3, 120–150 cm. This clay layer contains minor amounts of Fe oxides (4%), phillipsite (3%), and barite (2%). The subunit exhibits decimeter-scale, light/dark alternations, and contacts between lithologies that are heavily bioturbated. Abundant well-preserved burrows including *Zoophycos* and large (2–3 cm) unidentified burrows with white halos are present in Sections 198-1212B-8H-2 through 8H-3. A relatively high abundance of pyrite blebs are present in lower Eocene Sections 198-1212A-9H-4 through 9H-CC and Sections 198-1212B-8H-6 through 9H-3 (Fig. **F8**). Total color reflectance averages 67.5%. Red/blue color reflectance ratios, which average 2.1, are markedly higher in comparison with Unit I. At the base of the subunit there is a sharp contact between a moderate yellowish brown (10YR 5/4) clayey nannofossil ooze in Subunit IIA and a very pale orange (10YR 8/2) nannofossil ooze of Subunit IIB (Fig. **F8**). The P/E boundary occurs at the contact (see **"Biostratigraphy,"** p. 12). Sediments just below and within the clay-rich layer contain up to 5% microscopic inorganic calcite needles. In Hole 1212B, this clayey nannofossil ooze unit contains an unusual feature—a 1.5-cm burrow filled with opaline fragments, interpreted initially as remains of a sponge.

F8. Clay-rich layer at the P/E boundary, Section 198-1212A-10H-1, p. 37.

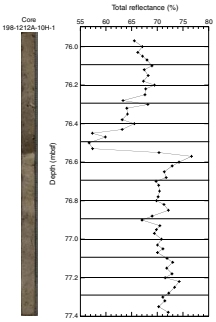

Subunit IIB

Subunit IIB (76.54 to 101.4 mbsf [Hole 1212A] and 81.43 to 101.44 mbsf [Hole 1212B]; Sections 198-1212A-10H-1, 64 cm, to 12H-CC, 6 cm, and 198-1212B-9H-5, 73 cm, to 11H-7, 24 cm; P/E boundary to K/T boundary) consists of predominantly very pale yellowish brown nannofossil ooze with clay interbedded with very pale orange (10YR 8/2) nannofossil ooze. The carbonate content is slightly higher (96.3 wt%) and is less variable (94.9%–96.4%) than in the overlying subunits. In addition to nannofossils, major constituents include clay (0%–25%) and foraminifers (0%–15%). Minor nonbiogenic components (0%–1%) include Fe oxides, volcanic glass, feldspar, quartz, and pyrite. Inorganic/organic calcite makes up 1%–3% of the sediment. Bedding is on a decimeter scale, and contacts are heavily to moderately bioturbated. Total color reflectance increases in Subunit IIB to 74.1%. The red/blue color reflectance ratio averages 1.5. The base of this unit lies at the K/T boundary and is marked by a sharp contact at which a pinkish gray (5YR 8/1) clayey unit overlies white nannofossil ooze.

Lithologic Unit III

Intervals: 198-1212A-12H-CC, 6 cm, through 13H-CC and 198-1212B-11H-7, 24 cm, through 27H-CC
Depths: 101.4 to 108.12 in Hole 1212A and 101.44 to 207.6 mbsf in Hole 1212B

Age: K/T boundary to late Albian

Unit III is predominantly homogeneous, soft, white (N9) nannofossil ooze and nannofossil ooze with foraminifers interbedded with chert. In addition to nannofossils (83%–99%), constituents include foraminifers (0%–10%), clay (1%–5%), and a trace of pyrite. Inorganic calcite, mostly rhombs and blades, makes up to 7% of the sediment in some intervals. The upper few centimeters of most cores in Unit III commonly contains very pale orange (10YR 8/2) chert fragments. Overall, the sediment is compositionally homogeneous and featureless. Carbonate content in the unit averages 96.7 wt% and varies within a narrow range (96.1–97.4 wt%). As a result, total color reflectance is high, averaging 92.3%, and the red/blue ratio is low, averaging 1.2%. Cores 198-1212B-17H and 24H are highly disturbed by coring. There are fragments of *Inoceramus* in Section 198-1212B-23H-2, 129 cm. At the base of Section 198-1212B-24H-7, two large unconformities from the Campanian to lower Santonian–Coniacian and from the Coniacian to the Albian are present. Recovery through the upper Campanian and lower Maastrichtian exceeded 90% in some intervals. The lower Santonian–Coniacian is represented by a pink, clayey layer in interval 198-1212B-24H-7, 13–24 cm, that contains glauconite.

Interpretation

Unit I

In general, the Unit I lithology is similar to Unit I at all of the Leg 198 sites on the southern Shatsky Rise, except Sites 1213 and 1214. The pervasive light–dark bedding cycles indicate the strong influence of glacial–interglacial climate cycles on local sedimentation. The dominant periodicity corresponds to eccentricity (100 k.y.) from 0 to 0.6 Ma, and obliquity (41 k.y.) from 0.6 to 2.5 Ma. These depositional cycles possibly reflect regional shoaling and deepening of the lysocline/CCD and/or climatically controlled variations in clay fluxes and carbonate production. Site 1212, however, differs in that the sediment accumulation rate through the Pliocene–Pleistocene was two to three times lower than at Sites 1209 and 1210, and slightly higher than at Site 1211 (Fig. F15). Although Site 1212 is roughly 300 m deeper than Site 1209, it is just 108 m deeper than Site 1210, suggesting that differential preservation was not responsible for the relative offsets in long-term accumulation rates. This is reflected in the nearly identical average Neogene carbonate contents between sites. Thus, current activity may be continuously or episodically sweeping sediment away from Site 1212, as well as Site 577, which has a similar unconformity. The location of Site 1212 on the western flank of the rise near an apparent canyon would support this supposition. Current-mediated erosion would also account for the extent of the middle Miocene–middle Eocene unconformity at the base of the unit.

In terms of overall general lithologic characteristics, Site 1212 is very similar to DSDP Site 577 with one notable exception: the color hues are darker on average throughout Unit I of Site 1212. Rather than the light gray (N7) and light olive-gray (5Y 6/1) hues observed at Site 1212, the Site 577 sediments were described as white (N9) to light gray (N7) (Heath, Burckle, et al., 1985). Although this difference is relatively subtle, it may be significant as there was little to no pyrite identified at Site 577.

Unit II

As observed at the other Leg 198 sites, Unit II sediment has a distinctly higher ratio of red to blue hues than sediment in Unit I. This change in color is partially indicative of a shift to more oxidized sediment pore water conditions, which at the other Southern High sites (1209 and 1210) has been attributed to the low Paleogene sedimentation rates and the low clay contents. One exception, however, is a 10-m interval at the base of Subunit IIA characterized by numerous pyrite blebs and burrows. Pyrite was not observed in such high concentrations at the other Leg 198 sites for the time-equivalent interval. Given the low sedimentation rate (2 m/m.y.) at this site, it is clear that some other factor was controlling pyrite formation. One possibility is that the pyrite is the result of locally high C_{org} or reactive Fe-mineral contents. However, nothing in the sediment composition as determined by smear slide examination currently supports this. For example, magnetic susceptibility levels are low, similar to other sites (see **"Physical Properties,"** p. 23).

The clay layer at the P/E boundary is very likely associated with the PETM event. During the PETM, the lysocline and CCD are thought to have risen rapidly as a result of massive dissociation of methane hydrate and its subsequent oxidation to CO_2 in bottom waters (Dickens et al., 1997). The added CO_2 lowers the pH and carbonate ion content of the seawater, thereby increasing dissolution of carbonate. Hence, the event is usually represented by a condensed interval. Highly fragmented foraminifers and high concentrations of fish debris in this layer at Site 1212 support the dissolution hypothesis.

In Subunit IIB in Hole 1212B, the red/blue color reflectance ratio abruptly increases upcore at 85.1 mbsf, whereas for the same time interval in Hole 1212A, the ratio increases at 94.7 mbsf. The contrasting colors between the two holes is difficult to account for because the magnetic susceptibility, bulk density, and carbonate content are identical. One possibility is that the color difference is an artifact of redox changes associated with the exposure of the sediment to the atmosphere. During coring at Site 1212, a delay in core processing necessitated storage of some cores on the catwalk for an extended period of time, whereas other cores were stored inside. A consequence of this, unfortunately, is that some reactions may have occurred in some cores and not in others.

The K/T boundary marks the base of Unit II. Here, a thin basal foraminiferal clay overlies white (N9) nannofossil ooze as observed at Sites 1209 and 1210. Previous drilling in the vicinity of Site 1212 at Sites 577 (Heath, Burckle, et al., 1985) and 47.2 (Fischer, Heezen, et al., 1971) also recovered K/T boundary intervals. The completeness of the boundary at DSDP Site 47.2, however, was difficult to ascertain because of severe coring disturbance. The boundary sequence at Site 577, on the other hand, was recovered intact and has provided essentially all that is known about the regional paleoenvironmental changes associated with that event. The carbonate record from Site 577 exhibits a subtle reduction (~2–3 wt%) in carbonate content across the boundary. This and a reduction in vertical carbon isotope gradients have been interpreted to represent a collapse in primary carbonate production as a result of the plankton extinction (Zachos et al., 1985). Carbonate content eventually recovers further upsection, indicating a recovery in production. Although carbonate content has not yet been measured in similar detail at Site 1212, the abrupt shift to lower reflectance across the boundary

and subsequent recovery several meters above suggest a similar change in carbonate deposition.

Diagenesis

The Unit I and II nannofossil oozes show little to no signs of carbonate recrystallization. The exception is the occurrence of micrometer-scale inorganic calcite needles in the interval within and below the clay-rich layer at the P/E boundary (Sections 198-1212A-10H-1, 64 cm, and 198-1212B-9H-5, 73 cm). These needles appear to be a common feature of the P/E boundary clay-layers at all sites on Shatsky Rise (see Fig. **F12,** p. 48, in the "Site 1209" chapter). Their origin remains uncertain, however. They may be related to the initial dissolution pulse associated with CO_2 injection, or they may have formed in response to the rapid rise in oceanic carbonate and Ca^{2+} ion content in the immediate aftermath of the dissolution pulse (Dickens, 2000).

In Unit III, inorganic calcite crystals (i.e., needles) become a more common constituent (1%–10%), indicating onset of incipient calcite solution and recrystallization in these Upper Cretaceous oozes. Still, as observed elsewhere on the rise, the sediment texture exhibits no obvious signs of lithification.

BIOSTRATIGRAPHY

Sediments of Site 1212 range in age from late Pleistocene to late Albian. Calcareous nannofossils are generally abundant and moderately to well preserved throughout the sediments of Holes 1212A and 1212B. Planktonic foraminifers are more variable in abundance and preservation, with the poorest preservation (high levels of test fragmentation) in the upper Miocene–Pleistocene. Sedimentation was not continuous and four unconformities/condensed intervals have been recognized separating upper Miocene/middle Miocene, middle Miocene/middle Eocene, mid-Campanian/lower Santonian–Coniacian, and Santonian–Coniacian/basal Cenomanian–uppermost Albian (see **"Sedimentation and Accumulation Rates,"** p. 19). All core catcher samples were examined, and supplementary samples were used to refine datum positions and the biostratigraphy in and around critical intervals. Several critical intervals were identified from Holes 1212A and 1212B and include the PETM, the K/T boundary, and the MME.

Benthic foraminifers were examined in selected core catcher samples in Holes 1212A and 1212B. They are generally well preserved and rare to few in abundance in the Neogene through Cretaceous sections except for the upper Paleocene and middle Eocene sections, where relative benthic abundance is high because of planktonic foraminiferal dissolution. Paleodepth estimates are based on the work of Pflum et al. (1976), Tjalsma and Lohmann (1983), Woodruff (1985), and van Morkhoven et al. (1986) for the Neogene and Paleogene section. For the Cretaceous section, estimates are mainly based on the study of Nyong and Olsson (1984) and the backtracked paleodepth curve from the DSDP and Ocean Drilling Program (ODP) data of Kaiho (1999).

Calcareous Nannofossils

Neogene

The Neogene section ranges from the upper Pleistocene (Zone CN15) to middle Miocene (Zones CN3 and CN4). The Pleistocene to upper Miocene interval appears to be relatively complete and exhibits a high sedimentation rate that is typical of other Neogene sections recovered during Leg 198 (Table T2). In mid- to lower Pliocene samples from Cores 198-1212A-4H through 7H (e.g., Samples 198-1212A-4H-CC and 5H-1, 45 cm) numerous reworked taxa of earliest Pliocene and late Miocene age, including *Reticulofenestra pseudoumbilicus, Amaurolithus* spp., and *Discoaster quinqueramus*, have been recognized. Care must be taken with the LOs of these species within this interval.

T2. Calcareous nannofossil datums, ages, and depths, p. 65.

An unconformity that includes most of the upper and middle Miocene is constrained by the FO of *Discoaster berggrenii* and the LO of *Sphenolithus heteromorphus* (Samples 198-1212A-8H-3, 5 cm, to 110 cm, and 198-1212B-7H-6, 5 cm, to 120 cm). Another significant unconformity separating lower middle Miocene and middle Eocene sediments lies just below this interval and is constrained by the occurrence of *Sphenolithus heteromorphus* (Zones CN3 and CN4) above and the occurrence of *Discoaster sublodoensis* (Zones CP12–lower CP13) below.

Paleogene

Paleogene sediments range from middle Eocene (Zone CP12) to earliest Paleocene (Subzone CP1a) in age, based on the FO of *Discoaster sublodoensis* and the FO of *Biantholithus sparsus,* respectively. Sedimentation rates are lower than in the overlying Neogene (see **"Sedimentation and Accumulation Rates,"** p. 19).

The P/E boundary and PETM interval appear to be relatively complete based on the levels of several datums. These datums include the LO of *Fasciculithus* (Samples 198-1212A-10H-1, 1 cm, and 198-1212B-9H-5, 55 cm), which lies just above the clay horizon that marks the PETM in the upper part of Zone CP8, the FO of *Discoaster diastypus* (Sample 198-1212A-9H-7, 30 cm), and the FO of *Tribrachiatus orthostylus* at the base of Subzone CP9a (Sample 198-1212A-9H-1, 10 cm). Not all datums were determined in both cores, due to sampling of inadequate resolution.

The K/T boundary is present in Cores 198-1212A-12H and 198-1212B-11H and appears to be complete. This interval follows the typical succession observed at other Leg 198 sites and includes the LO of *Micula prinsii* at the top of Zone CC26 and the presence of bladelike calcite below the boundary and the presence of common calcispheres above the boundary (Samples 198-1212A-12H-7, 73 cm, and 198-1212B-11H-7, 20 cm). These sediments are immediately overlain by an interval devoid of nannofossils, except for a few "survivor" species, such as *Markalius inversus* and *Goniolithus fluckigeri,* and reworked Cretaceous taxa (Samples 198-1212A-12H-7, 60 cm, and 198-1212B-11H-7, 3 cm). This interval is capped by sediments of Subzone CP1a, including taxa such as *Biantholithus sparsus* and *Neobiscutum* spp. (Samples 198-1212A-12H-6, 80 cm, 198-1212B-11H-4, 70 cm, 198-1212A-12H-7, 1 cm, and 198-1212B-11H-6, 70 cm, respectively).

Cretaceous

Sediments of late Maastrichtian to late Albian age were recovered from Holes 1212A and 1212B. High sedimentation rates characterize the Maastrichtian and upper Campanian interval. The nannofossil assemblages from these sediments are typically well preserved and diverse. The Maastrichtian appears to be relatively complete. Sediments assigned to Zone CC22 (Campanian) overlie a short section of Coniacian-aged chalk in Section 198-1212B-24H-6, based on the presence of *Lithastrinus septenarius* and the absence of *Micula staurophora* (Sample 198-1212B-24H-6, 30 cm). This, in turn, overlies sediment assigned to lower Subzone NC10a (basal Cenomanian–upper Albian) based on the presence of *Eiffellithus turriseiffelii* and *Broinsonia stenostaurion* (interval 198-1212B-24H-6, 40–51 cm).

Planktonic Foraminifers

Neogene

The upper 60 m of section at Site 1212 records continuous deposition of uppermost Miocene–Pleistocene sediment based on the recognition of planktonic foraminiferal Zones N18–N22 (Table T3). Preservation of planktonic foraminifers varies from poor to moderate, with selective dissolution and fragmentation leading to the sporadic presence of some biostratigraphically useful taxa through this interval. Most of the core catcher samples examined from Holes 1212A and 1212B are dominated by dissolution-resistant taxa including *Globorotalia inflata* (upper Pliocene–Pleistocene), *Truncorotalia crassaformis, Sphaeroidinella dehiscens, Sphaeroidinellopsis seminulina* (uppermost Miocene–lower Pliocene), and *Sphaeroidinellopsis subdehiscens,* with persistent but lower numbers of *Globigerina bulloides, Neogloboquadrina pachyderma* (dextral), *Neogloboquadrina dutertrei, Globorotalia tumida, Globoconella conomiozea* (lower Pliocene), *Globigerinoides ruber, Globigerinoides sacculifer, G. obliquus,* and *Orbulina universa*. Occasional downhole contamination in the core catcher samples is suspected based on the presence of very rare *Truncorotalia truncatulinoides* below its predicted range mixed with specimens indicative of Zone N19 in Sample 198-1212A-4H-CC. In addition, reworking of older sediments or downhole mixing of assemblages is responsible for the co-occurrence of *Truncorotalia tosaensis* (upper Pliocene–Pleistocene) and *Globorotalia margaritae* (uppermost Miocene–lower Pliocene) in Sections 198-1212A-4H-CC and 5H-CC. Section 198-1212A-7H-CC contains early forms of *G. tumida* with *G. margaritae, Globorotalia plesiotumida,* and *Globigerinoides conglobatus,* without *Sphaersoidinella dehiscens*, suggesting a Zone N18 assignment.

An unconformity or condensed section in Sections 198-1212A-8H-3 and 198-1212B-7H-6 separates the uppermost Miocene (Zone N18 or N17) and lower middle Miocene (Zone N9). Sample 198-1212B-7H-6, 118–120 cm, was collected near the base of this dark-colored interval and contains *Orbulina universa, Praeorbulina glomerosa, Paragloborotalia mayeri, Globigerinoides mitra, Sphaeroidinellopsis seminulina, Sphaeroidinellopsis disjuncta*, and *Fohsella peripheroronda*.

Paleogene

The lower middle Miocene rests unconformably on lower middle Eocene sediments assigned to Zone P11 based on the presence of *Morozovella aragonensis, Igorina broedermanni, Acarinina pentacamerata, Trun-*

T3. Planktonic foraminifer datums, ages, and depths, p. 66.

corotaloides libyaensis, and *Globigerinatheka senni* in Sample 198-1212B-7H-6, 135–137 cm. A relatively thin Paleocene–lower middle Eocene section was cored at Site 1212, and many of the planktonic foraminiferal zones were not observed during the course of core catcher examination because of the low sedimentation rates (see **"Sedimentation and Accumulation Rates,"** p. 19). Planktonic foraminiferal preservation varies from moderate to good.

The LO of *Morozovella velascoensis,* which lies a short distance above the onset of the PETM, lies between Samples 198-1212B-9H-4, 114 cm, and 9H-5, 42 cm. The base of the PETM event, however, appears to correspond to an unconformity in Hole 1212B. Foraminifers in Sample 198-1212B-9H-5, 77–78 cm, include *Globanomalina pseudomenardii,* the LO of which defines the top of Zone P4 at 55.9 Ma, some 0.4 m.y. before the onset of the event.

A paleontologically complete K/T boundary section was recovered at Site 1212. The boundary is bioturbated, and burrows of the lowermost Danian sediment extend 10 cm into the uppermost Maastrichtian. These lowermost Danian sediments yield a tiny *Guembelitria* assemblage reminiscent of the P0 zonal fauna in the deepest burrows, followed above by the assemblage of Zone Pα, defined by the first occurrence of *Parvularugoglobigerina eugubina,* in Samples 198-1212A-12H-7, 23–24 cm, 12H-7, 72 cm, and 198-1212B-11H-7, 23–24 cm. The former sample contains rare ~100-µm-sized, amber to olive-green spherules, probably altered tektites. The spherules are concentrated in the first 2–3 cm above the K/T boundary within Zone Pα. At Site 1212, in the lowest 10–20 cm of the basal Paleocene, planktonic foraminifers are extremely abundant representing up to 34% of smear slides.

Cretaceous

A relatively thick and continuous section of mid-Campanian–Maastrichtian nannofossil ooze was recovered in Hole 1212B based on the complete succession of planktonic foraminiferal zones from the *Radotruncana calcarata* (Zone KS27) through the *Abathomphalus mayaroensis* (Zone KS31) Zones in intervals 198-1212A-12H-CC through 13H-CC and 198-1212B-11H-CC through 23H-CC (Table **T3**). The ooze immediately underlying the K/T boundary correlates to the uppermost Maastrichtian *Abathomphalus mayaroensis* Zone (Zone KS31) based on the presence of the nominal taxon, but the planktonic foraminiferal assemblages are affected significantly by dissolution. Below this level, however, assemblages are diverse and generally well preserved. Section 198-1212B-24H-6 contains a 20- to 25-cm-thick section of intact chalk containing planktonic foraminifers of Coniacian–early Santonian age, thereby suggesting an unconformity in the highly disturbed sediments of Core 198-1212B-24H.

Another stratigraphic break separating the Coniacian–lower Santonian and basal Cenomanian is present between Cores 198-1212B-24H and 25H. Sample 198-1212B-25H-1, 42–43 cm, contains planktonic foraminifers indicative of the lower Cenomanian–uppermost Albian *Rotalipora globotruncanoides* Zone (Zone KS17) based on the presence of the nominal taxon without *Planomalina buxtorfi*. Samples 198-1212B-25H-CC and 27H-CC are assigned to the upper Albian *Rotalipora appenninica* Zone (Zone KS16) based on the presence of *Hedbergella libyca* in the former sample and the co-occurrence of rare *R. appenninica* and *P. buxtorfi* in the latter sample.

Benthic Foraminifers

Neogene

Samples 198-1212A-1H-CC through 5H-CC (Pleistocene–lower Pliocene), benthic assemblages are characterized by *Cibicidoides wuellerstorfi, Oridorsalis tener, Pullenia bulloides, Pyrgo murrhina,* and uvigerinids (*Uvigerina hispida* and *Uvigerina hispidocostata*). Samples 198-1212A-6H-CC and 7H-CC (lower Pliocene–upper Miocene) are dominated by stilostomellids (*Stilostomella abyssorum, Stilostomella gracillima,* and *Stilostomella subspinosa*). Additional taxa include *O. tener, P. bulloides, P. murrhina,* and agglutinated taxa (*Karreriella bradyi* and *Martinottiella* sp.) (Table T4).

These characteristic benthic assemblages indicate upper abyssal depths (2000–3000 m), even though taxa such as *Pullenia bulloides* show a wide bathymetric range from lower neritic–abyssal depth (Pflum et al., 1976).

T4. Cenozoic and Cretaceous benthic foraminifers, Hole 1212A, p. 67.

Paleogene

In Samples 198-1212A-8H-CC (middle Eocene) and 9H-CC (uppermost Paleocene), benthic foraminifers are very rare in abundance and moderately preserved. Their test sizes are small, and most of the specimens are found in the 125- to 250-µm size fraction, except for nodosariids (*Dentalina* spp. and *Nodosaria* spp.). Benthic assemblages in Sample 198-1212A-8H-CC are characterized by small-sized buliminids (*Buliminella grata, Bulimina impendens,* and *Bulimina jarvisi*), *Clinapertina complanata, Dentalina* spp., and *Nuttallides truempyi*. In Sample 198-1212A-9H-CC, *N. truempyi, Oridorsalis umbonatus*, and *Quadrimorphina profunda* characterize the assemblage. No agglutinated forms are present in these two samples.

In Samples 198-1212A-10H-CC through 12H-CC and 198-1212B-10H-CC, benthic assemblages are generally represented by abundant *Oridorsalis umbonatus, Gyroidinoides globosus, Nuttallides truempyi, Dentalina* spp., *Lenticulina* spp., abundant *Tritaxia* (*Tritaxia globulifera, Tritaxia* spp., and *Tritaxia rugolosa*), and *Spiroplectammina jarvisi*. Though rare in abundance, *Aragonia ouezzanensis, Aragonia velascoensis,* and buliminids (*Bulimina trinitatensis, Bulimina velascoensis, Buliminella grata,* and *Quadratobuliminella pyramidalis*) are also characteristic forms in these sections (Table T4). These Paleogene benthic assemblages are indicative of upper abyssal depths (2000–3000 m), according to Tjalsma and Lohmann (1983) and van Morkhoven et al. (1986).

Cretaceous

The Upper Cretaceous Samples 198-1212A-13H-CC and 198-1212B-12H-CC through 23H-CC contain abundant *O. umbonatus, G. globosus, N. truempyi, Nuttallinella florealis, Aragonia ouezzanensis, A. velascoensis, Dentalina* spp., *Lenticulina* spp., and abundant agglutinated taxa (*Marssonella trochoides, Gaudryina pyramidata, Spiroplectammina* sp., *S. jarvisi, Tritaxia* spp., *T. globulifera,* and *T. rugolosa*). Section 198-1212B-24H-CC is represented by highly disturbed sediment that contains an assemblage with Albian–Cenomanian benthic foraminifers, including *Conorotalites aptiensis* and *Hanzawaia compressa,* mixed with younger Cretaceous taxa.

Samples 198-1212B-25H-CC and 27H-CC are characterized by Lower Cretaceous benthic foraminifers including abundant trochospiral cal-

careous species (*Conorotalites aptiensis, Gyroidinoides globosus, Gyroidinoides infracretaceus, Hanzawaia compressa, Protosangularia albiana,* and *Protosangularia cenomaniana*), diverse nodosariids (*Astacolus* spp., *Dentalina* spp., *Lenticulina* spp., *Marginulina inaequalis, Nodosaria* spp., and *Saracenaria triangularis*), and abundant agglutinated taxa (*Dorothia gradata, Marssonella oxycona, Pseudoclavulina* sp., *Rhizammina* spp., *Spiroplectammina* sp., *Spiroplectinella excolata, Tritaxia* spp., and *T. globulifera*). *Pleurostomella* spp. is also abundant in these samples (Table T5).

T5. Cenozoic and Cretaceous benthic foraminifers, Hole 1212B, p. 69.

PALEOMAGNETISM

Archive halves of core sections from Holes 1212A and 1212B were measured on the shipboard pass-through magnetometer unless they displayed obvious and pervasive coring disturbance. Measurements were made on Cores 198-1212A-1H through 12H and on one section of Core 13H. From Hole 1212B, Cores 198-1212B-1H to 13H, 15H, 18H to 20H, and 23H were measured. Cores 198-1212B-14H, 16H, 17H, 21H, 22H, 25H, and 27H were not measured because of low recovery and/or pervasive disturbance. The results from Site 1212 are similar to other sites on southern Shatsky Rise. Cores of Pliocene and younger age yield an easily interpretable magnetic polarity stratigraphy, whereas most data from older cores are uninterpretable. This is largely attributed to deformation of the soft sediments during drilling, core recovery, or core splitting.

As for other Leg 198 sites, the natural remanent magnetization (NRM) of core sections was measured at 5-cm intervals, followed by measurement after two or three alternating-field (AF) demagnetization steps (10- and 20-mT peak fields, with a 15-mT step added when time permitted). NRM intensity values typically stayed within a narrow range, from ~2×10^{-3} to 10^{-1} A/m for Cenozoic sediments, but showed a drop of an order of magnitude for the Upper Cretaceous section at depths greater than 100 meters composite depth (mcd). After AF demagnetization at 20 mT (to remove the drill string overprint), the downward trend was similar with a shift to values 5 to 10 times weaker than NRM values (Fig. F9). A decline of magnetization intensity of about one order of magnitude was observed with depth from the surface to 70 mcd. Below that, the magnetization intensity increases slightly from 80 to 105 mcd in cores around the K/T boundary and drops to levels near the sensitivity limit of the cryogenic magnetometer in Maastrichtian and Campanian ooze (Fig. F9).

F9. Archive-half magnetization intensities after AF demagnetization at peak fields of 20 mT, p. 38.

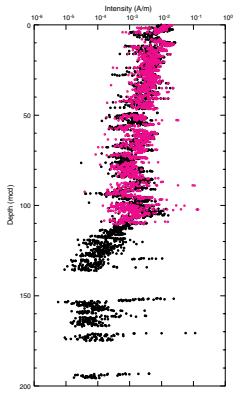

Paleomagnetic data acquired from the shipboard pass-through magnetometer from Site 1212 produced an interpretable magnetic polarity stratigraphy in the upper ~50 mcd. In this Pliocene and Pleistocene section, it was possible to recognize polarity zones corresponding to the Brunhes Chron (C1n) to the base of the Gauss Chron (C2A) in both holes (Fig. F10).

Measurements on cores deeper than ~50 mcd showed erratic inclination values and poor correlation between Holes 1212A and 1212B (Fig. F10), making it impossible to make a reliable polarity interpretation for the upper Miocene to Cretaceous section. As at previous sites, the problem is attributed to pervasive coring deformation of the soft sediments of those ages. It may be possible to construct a polarity stratigraphy from carefully chosen discrete samples that are not severely affected by drilling disturbance.

F10. Inclination after AF demagnetization at peak fields of 20 mT, p. 39.

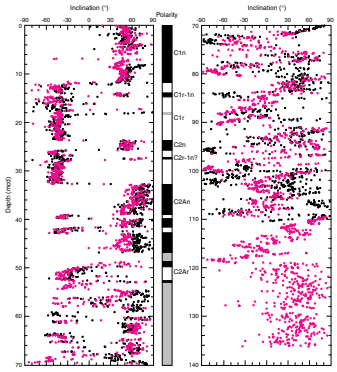

Polarity chrons recognized in the upper 45 mcd of the section yield an age-depth curve for the Pliocene–Pleistocene sediments (Fig. F11). For this interval, the polarity stratigraphy suggests a near uniform sedimentation rate of ~13 m/m.y.

COMPOSITE DEPTHS

Multisensor track (MST) and spectral reflectance (L*) data collected from Holes 1212A and 1212B were used to determine depth offsets in the composite section. Magnetic susceptibility, gamma ray attenuation (GRA) bulk density, and spectral reflectance measurements were the primary parameters used for core-to-core correlation. GRA bulk density and magnetic susceptibility data were collected at 3-cm intervals and spectral reflectance data were collected at 2.5-cm intervals on all cores (see "MST Measurements," p. 23, in "Physical Properties" and "Lithostratigraphy," p. 4, in the "Explanatory Notes" chapter for details about MST and spectral reflectance data).

The data used to construct the composite section and determine core overlaps are presented in a composite depth scale in Figure F12. The depth offsets that comprise the composite section for Holes 1212A and 1212B are given in Table T6. Units for the composite depth scale are meters composite depth.

The composite data show that the APC cores from Site 1212 provide a more or less continuous overlap to at least 115 mcd (K/T boundary; ~109 mcd in Core 198-1212A-12H). Core 198-1212B-2H was tentatively appended to Core 1H (Fig. F13; Table T7), as there was no overlapping interval recovered in Hole 1212A. As a result, minor offsets between holes have been found within the underlying ~40 mbsf. This led to inadequate overlapping of accompanying cores (Fig. F13; e.g., the base of Core 198-1212B-3H was tied to the top of Core 198-1212B-4H, the base of Core 198-1212B-4H was tied to top of Core 198-1212B-5H, the base of Core 198-1212A-2H was tied to the top of Core 198-1212B-3H, the base of Core 198-1212A-3H was tied to the top of Core 198-1212A-4H, and the base of Core 198-1212A-5H was tied to the top of Core 198-1212A-6H; see Table T7). There may also be a gap between Cores 198-1212B-11H and 12H (Core 198-1212B-12H was appended to Core 198-1212B-11H; see Table T7), as no overlapping interval was recovered in Hole 1212A.

Below the uppermost Maastrichtian, most of the cores from Holes 1212A and 1212B could not be correlated and placed into a composite depth framework because of low signal amplitude. Expansion of sedimentary features in one hole relative to coeval cores in the other hole indicate distortion of the cored sequence. Because some distortion occurred within individual cores on depth scales of <9 m, it was not possible to accurately align every feature in the MST and color reflectance records by simply adding a constant to the mbsf core depth.

Following construction of the composite depth section for Site 1212, a single spliced record was assembled for the aligned cores over the upper 115 mcd using cores from both holes. Intervals having significant disturbance or distortion were avoided. The PETM interval in the composite was taken from Core 198-1212B-9H.

F11. Age-depth curve derived from magnetic stratigraphy, p. 40.

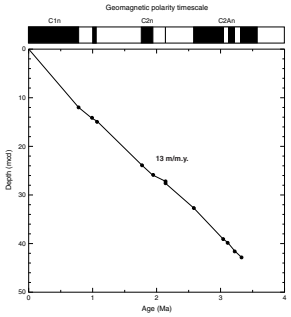

F12. Magnetic susceptibility and GRA density, p. 41.

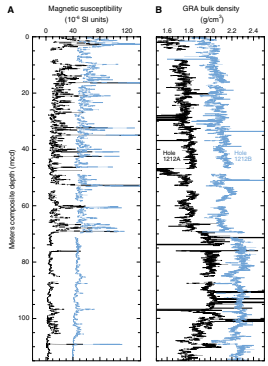

T6. Composite depth section, p. 71.

F13. Magnetic susceptibility data for 0 to 50 mcd, p. 42.

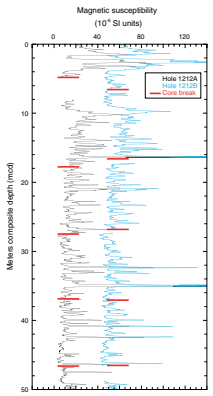

T7. Splice tie points, p. 72.

SEDIMENTATION AND ACCUMULATION RATES

Unconformities and changes in sedimentation rate at Site 1212 are illustrated in a plot of calcareous microfossil datum ages (first and last occurrences) vs. depth (Fig. F14). These rates rely on major calcareous nannofossil and planktonic foraminiferal datums presented in Tables T2 and T3 (see "Biostratigraphy," p. 12). The Pleistocene–upper Albian section cored at Site 1212 is punctuated by at least four unconformities: lower middle Miocene/lower middle Eocene, mid-Campanian/lower Santonian–Coniacian, and Coniacian/basal Cenomanian. In addition, a fourth unconformity or condensed interval separates the uppermost Miocene and lower middle Miocene.

An expanded view of the Neogene (Fig. F15) shows that the uppermost Miocene–Pleistocene section accumulated at rates of ~8.7 m/m.y., although discrete intervals accumulated at rates that varied from 4.1 to 16.3 m/m.y. Dark-colored, clay-rich sediments in Sections 198-1212A-8H-1 and 8H-2 and Sections 198-1212B-7H-3 and 7H-4 may contain an unconformity or condensed interval(s) between uppermost Miocene and lower middle Miocene sediments. The gradational color change between Sections 198-1212A-8H-3 and 8H-4 and 198-1212B-7H-6 and 7H-7 marks the bioturbated unconformity separating the lower middle Miocene and the lower middle Eocene (Figs. F15, F16).

Sedimentation rates in the Eocene range between 1.5 and 2.0 m/m.y. (Fig. F16). The upper Paleocene shows sedimentation rates of ~2.5 m/m.y. decreasing to 1.8 m/m.y. through the mid- and lower Paleocene (Fig. F17). A diastem was detected in the uppermost Paleocene, at the base of the PETM, in Hole 1212B (see "Biostratigraphy," p. 12). Shipboard biostratigraphy indicates that the K/T boundary interval is paleontologically complete.

Sedimentation rates for the Campanian–Maastrichtian interval were significantly higher than the Paleogene with rates of ~8.5–9.2 m/m.y. (Fig. F17). A 20- to 25-cm-thick interval of intact chalk in Section 198-1212B-24H-6 in an otherwise highly disturbed core indicates an age of early Santonian–Coniacian. Two major unconformities occur in the interval between Sections 198-1212B-23H-CC and 25H-1. Lowermost Cenomanian–uppermost Albian sediments accumulated at an average rate of 8.8 m/m.y. (Fig. F18).

Mass accumulation rates for the bulk sediment, carbonate, and noncarbonate fractions were calculated using dry bulk density and carbonate content (see "Organic Geochemistry," p. 20) data through eight linear sedimentation rate segments in the Cretaceous–Neogene section recovered at Site 1212 (Table T8). These segments were chosen to reflect the major changes in sedimentation rate as shown in Figure F14. Mass accumulation rate data are not available for sections of core immediately adjacent to intervals of stratigraphic importance, such as the PETM and the K/T boundary.

As observed at Sites 1209–1211 on the Southern High of Shatsky Rise, sedimentation during Campanian and Maastrichtian was carbonate dominated and marked by high mass accumulation rates, averaging 1.0 g/cm²/k.y. (Fig. F19). Beginning in the earliest Paleocene, the rate of bulk sediment accumulation dropped dramatically to an average of 0.2 g/cm²/k.y. The same low rate of accumulation prevailed through early middle Eocene time (Fig. F19). Bulk sediment accumulation rates remained low during middle Miocene and late Miocene to early Pliocene time, averaging 0.2 and 0.4 g/cm²/k.y., respectively. As at Sites 1207–

F14. Age-depth plot of calcareous nannofossil and planktonic foraminiferal datums, p. 43.

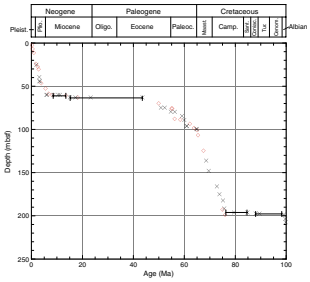

F15. Age-depth plot of Neogene calcareous nannofossil and planktonic foraminiferal datums, p. 44.

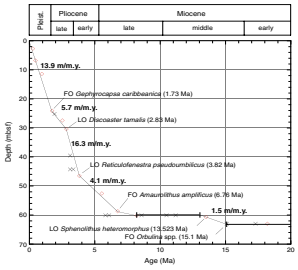

F16. Age-depth plot of early Oligocene–late Paleocene calcareous nannofossil and planktonic foraminiferal datums, p. 45.

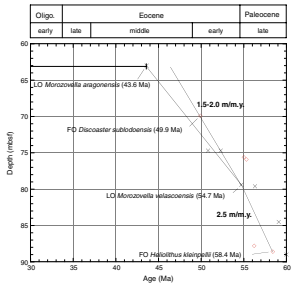

F17. Age-depth plot of early Eocene–Campanian calcareous nannofossil and planktonic foraminiferal datums, p. 46.

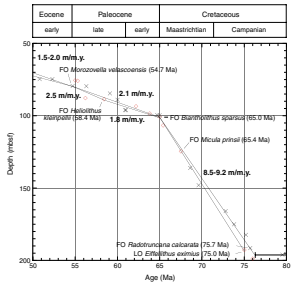

1211, there was a shift to higher rates of bulk sediment accumulation accompanied by an increased proportion of noncarbonate sediment in the late Pliocene (Fig. F19). These conditions have prevailed through to the present time.

ORGANIC GEOCHEMISTRY

Volatile Hydrocarbons

Headspace gas analysis was conducted as part of the standard protocol required for shipboard safety and pollution prevention monitoring. A total of nine cores from Hole 1212A were evaluated (Table T9). The concentrations of CH_4 were at background levels (range = 1.8–2.1 µL/L [ppmv]); no hydrocarbon gases higher than C_1 were detected.

Carbonate

Carbonate determinations by coulometry were made for a total of 26 samples from Hole 1212A and 11 samples from Hole 1212B (Table T10). Samples were selected to provide a measure of the carbonate content within different units and to assess the influence of carbonate content on color reflectance. The values for carbonate content range from 53 to 90 wt% in Pleistocene to middle Miocene nannofossil ooze of Unit I (Table T10; Fig. F20); lower values correspond to intervals enriched in clay or silica. Nannofossil ooze of Unit II (Paleogene) contains uniformly high carbonate values (mean = 95.9 wt%; standard deviation = 0.81) that are marginally less than those of Unit III (Cretaceous) (mean = 96.7 wt%; standard deviation = 0.31).

INORGANIC GEOCHEMISTRY

Interstitial Water Chemistry

Thirteen interstitial water samples were collected at Site 1212. In Hole 1212A, nine samples were taken between 0 and 90 mbsf (one sample/core). Hole 1212B was sampled only when depths exceeded those reached in Hole 1212A. The sampling resolution was decreased (one sample per three cores) in Hole 1212B such that four samples were collected between 100 and 200 mbsf. Details of analytical methods can be found in "Inorganic Geochemistry," p. 21, in the "Explanatory Notes" chapter. Filtered (0.45 µm) samples were analyzed for pH, salinity, chlorinity, alkalinity, sulfate (SO_4^{2-}), phosphate (HPO_4^{2-}), ammonium (NH_4^+), silica ($Si(OH)_4$), boron (H_3BO_3), iron (Fe^{2+}), manganese (Mn^{2+}), and major cations (Na^+, K^+, Mg^{2+}, Ca^{2+}, Li^+, Sr^{2+}, and Ba^{2+}). A compilation of data is provided in Table T11. Cited values for average seawater composition are from Millero and Sohn (1992) and Broecker and Peng (1982).

pH, Salinity, Chloride, and Sodium

The pH of pore waters at Site 1212 ranges between 7.37 and 7.63, with an average value of 7.45 ± 0.07 (Table T11). All values are lower than the average seawater value of 8.1. As at Sites 1209–1211, variability in the pH profile occurs within the upper lithologic unit, which is char-

F18. Age-depth plot of Maastrichtian–Albian calcareous nannofossil and planktonic foraminiferal datums, p. 47.

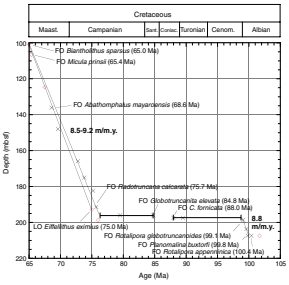

T8. Linear sedimentation rate segments and average accumulation rates, p. 73.

F19. Mass accumulation rates vs. depth and age for the Maastrichtian–Pleistocene, p. 48.

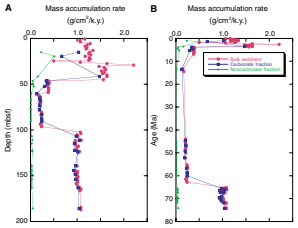

T9. Headspace CH^4 concentrations, p. 74.

T10. Carbonate content, p. 75.

F20. Carbonate profile, p. 49.

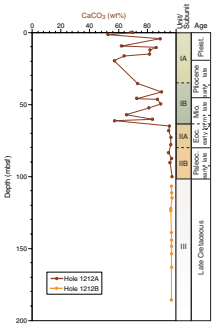

T11. Geochemical data, p. 76.

acterized by a lesser proportion of carbonate sediment (72 wt% carbonate through Subunit IA) relative to underlying sediments (82 wt% carbonate in Subunit IB) (see "Carbonate," p. 20, in "Organic Geochemistry"). Below ~40 mbsf, the pH becomes relatively uniform as the carbonate content of the sediments increases, reflecting the buffering capacity of carbonate-dominated sediments. Salinity ranges from 34.0 to 35.5 g/kg.

The chloride (Cl^-) pore water profile fluctuates around a mean of 559 ± 2 mM, with an increase in pore water Cl^- anion content between ~30 and 90 mbsf (Fig. F21). Sodium (Na^+) concentrations, calculated using the methods described in Broecker and Peng (1982), average 474 ± 3 mM (Fig. F22). Such broad downcore variations in pore water Na^+ and Cl^- profiles of pelagic sediments have been linked to variations in mean ocean salinity associated with changes in ice volume (McDuff, 1985; Schrag et al., 1995).

F21. Sodium and chloride profiles, p. 50.

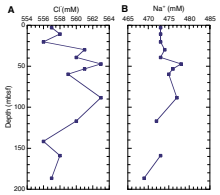

Alkalinity, Sulfate, Ammonium, Phosphate, Iron, and Manganese

The concentrations of SO_4^{2-}, alkalinity, NH_4^+, and HPO_4^{2-} in the interstitial waters at Site 1212 (Fig. F22) are relatively low and invariant. Downcore, SO_4^{2-} concentrations decrease steadily from 28 mM (average seawater concentration) in the uppermost sample to 22 mM at 88.35 mbsf. Below this depth, SO_4^{2-} remains uniform at 22 mM down to the bottom of the profile (186.60 mbsf). Alkalinity decreases from 2.8 mM in the surface pore waters (10.85 mbsf) to 2.2 mM at 159.10 mbsf. Here, the trend reverses, and the alkalinity increases to 2.8 mM at 186.60 mbsf.

F22. Sulfate, alkalinity, ammonium, and phosphate profiles, p. 51.

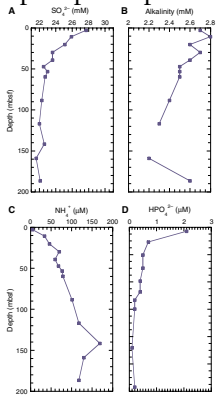

Similar to Sites 1209–1211, the NH_4^+ concentrations are low (between 5 and 130 µM), implying that the organic matter content of the sediment at Site 1212 is low (see "Carbonate," p. 20, in "Organic Geochemistry"). This interpretation is supported by the limited downcore decrease in SO_4^{2-} and the low pore water HPO_4^{2-} concentrations, the highest values of which are <2 µM (1.5–1.8 µM) (Fig. F22). However, Site 1212 has the greatest degree of sulfate reduction on the Southern High. A corresponding increase in pyrite was observed through lithologic Unit I in cores from Site 1212 relative to other Southern High sites (see "Lithologic Unit I," p. 7, in "Lithostratigraphy").

The Mn^{2+} profile exhibits a downcore decrease from 16 µM at 2.95 mbsf to 1 µM at 39.35 mbsf. Below this depth, there is little variation in the Mn^{2+} profile and concentrations remain low (1–4 µM). As at Sites 1209 and 1210, elevated concentrations of Mn^{2+} in the upper part of the sediment section are likely related to the occurrence of a condensed interval containing Mn-rich phases. Consequently, the minor excursion at ~60 mbsf is interpreted to reflect the dissolution of Mn minerals and diffusion of Mn^{2+} away from Mn-rich sediments.

After an increase to 4 µM in the uppermost sediments, the downcore Fe^{2+} concentrations decrease significantly through the upper ~50 mbsf of the section. Concentrations decrease from 42 µM at 2.95 mbsf to 4 µM at 53.35 mbsf; the lower part of the profile is uniform with average concentrations of 3 ± 1 µM (Fig. F23). The inflection at ~50 mbsf coincides with the middle Miocene to lower middle Eocene unconformity in Core 198-1212A-7H (see "Lithostratigraphy," p. 7). The elevated concentrations of Fe^{2+} through the sediment section corresponding to

F23. Manganese and iron profiles, p. 52.

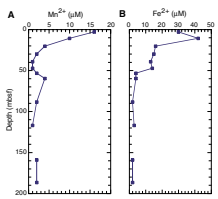

lithologic Unit I (0.00–53.60 mbsf) are likely related to the close proximity of volcanic ash (Subunit IA) and other Fe^{2+} sources to sites of pyrite formation.

Potassium, Calcium, Magnesium, Strontium, and Lithium

The concentrations of K^+, Ca^{2+}, and Mg^{2+} in the upper pore waters at Site 1212 differ little from concentrations in average seawater (12, 11, and 51 mM, respectively) (Fig. F24). In lithologic Unit II (≥~60 mbsf) of the section, downcore trends are consistent with those resulting from exchange with basaltic basement at depth (Gieskes, 1981), wherein K^+ and Mg^{2+} concentrations decrease downcore and Ca^{2+} increases. However, in lithologic Unit I, it is likely that processes other than exchange with basement are affecting the distribution of Mg^{2+} cations. In the pore waters contained within Unit I (see "Lithologic Unit I," p. 7, in "Lithostratigraphy"), Mg^{2+} concentrations decrease at a rate that is inconsistent with what might be expected for a diffusional gradient associated with basement exchange. Consequently, it is likely that a Mg-rich phase is precipitating within lithologic Unit I. Below ~50 mbsf, where the lithology is dominated by carbonate-rich phases, Mg^{2+} concentrations become uniform (46.7 ± 0.3 mM). Assuming that volcanic weathering reactions with basement are removing Mg^{2+} from interstitial waters at depth, the trend observed below ~50 mbsf implies that Mg^{2+} cations are being mobilized into the pore waters. Although there is a 5-mM increase in Ca^{2+} through this interval, the Sr profile and Sr/Ca ratios imply that carbonate dissolution is not responsible for the increase in Mg^{2+}.

The Sr^{2+} and Sr/Ca pore water profiles both increase steadily from the shallowest sample at 2.95 mbsf down to 29.85 mbsf, suggesting that carbonate dissolution or recrystallization is occurring within this interval (Fig. F24) (e.g., Baker et al., 1982). Pore waters collected within lithologic Subunit IB and lithologic Unit II show little change in either the Sr^{2+} or Sr/Ca profiles, implying that there is little additional Sr^{2+} input from carbonate alteration.

The Li^+ concentrations decrease sharply from 30 µM in the shallowest sample (2.95 mbsf) to a minimum of 16 µM at 10.85 mbsf (Fig. F24). Below this depth, concentrations gradually increase to 22 µM at the base of the profile (186.60 mbsf). The decrease to Li^+ concentrations below that of average seawater (25 µM) may reflect uptake by clay minerals forming through the weathering of volcanic material (Gieskes, 1981).

F24. Potassium, calcium, magnesium, strontium, and lithium profiles, p. 53.

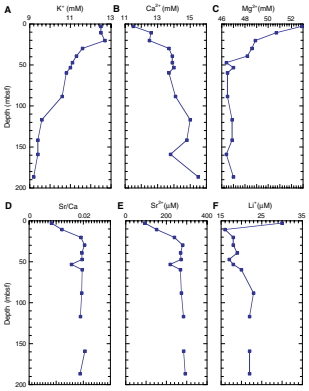

Silica

The shape of the dissolved silica profile at Site 1212 is generally similar to those observed at Sites 1207–1211 (Fig. F25). Pore water silica concentrations are highest in lithologic Unit I, ranging between 550 and 660 µM. Through the underlying sediment section, pore water $Si(OH)_4$ concentrations decrease gradually to 144 µM at the base of the profile (159.10 mbsf). Elevated concentrations in the upper part of the profile are interpreted to reflect the leaching and weathering of volcanic ash and biogenic silica in the Pliocene–Pleistocene sediments. Lower concentrations coincide with the appearance of carbonate-dominated sediments and chert in lithologic Units II and III. The removal of

F25. Silica profile, p. 54.

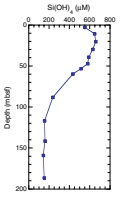

$Si(OH)_4$ from pore waters may be the result of the recrystallization of opal-A to opal-CT or quartz (Baker, 1986; Gieskes, 1981).

Boron and Barium

Given that variations in the Ba^{2+} and H_3BO_3 concentrations in pore waters of pelagic sediments are poorly understood, profiles for these parameters at Site 1212 are described largely for purposes of documentation (Table T11). The average boron concentration (378 ± 21 µM) is higher than that of average seawater (416 µM). The Ba^{2+} concentration averages 0.3 ± 0.1 µM, and the profiles show little variability with depth. Concentrations are extremely low, but on average, are higher than those of average seawater, implying that Ba^{2+} is being added to the system. Possible sources of Ba^{2+} include calcareous skeletal debris and minor volcanic ash in the Neogene section, which may be undergoing leaching and/or dissolution.

PHYSICAL PROPERTIES

Physical properties at Site 1212 were measured on both whole-round sections and discrete samples from split-core sections. Continuous whole-round measurements were made of magnetic susceptibility, GRA bulk density, and compressional *P*-wave velocity, using the MST, for all Site 1212 cores. Natural gamma radiation measurements were made with the MST on Core 198-1212A-12H only. Discrete measurements of compressional *P*-wave velocity were made at a routine frequency of at least one measurement per split-core section in Holes 1212A and 1212B. Index properties were measured on discrete samples from split-core sections at an average frequency of one measurement per section in Hole 1212A.

MST Measurements

All core sections from Holes 1212A and 1212B were routinely measured on the MST for magnetic susceptibility and GRA bulk density at 3-cm intervals (Figs. F26, F27). MST *P*-wave velocity was routinely measured at 10-cm intervals on all cores from Holes 1212A and 1212B (Fig. F28). Natural gamma radiation (NGR) was measured at 30-cm intervals in Core 198-1212A-12H only. All collected MST data are archived in the ODP Janus database.

Magnetic susceptibility values (Fig. F26) are generally highest in the uppermost ~63 m of the Site 1212 sedimentary column; this interval equates to Pleistocene–lower Miocene lithologic Unit I (see "Lithologic Unit I," p. 7, in "Lithostratigraphy"). Peaks in magnetic susceptibility within lithologic Subunit IA may correlate with distinctive ash layers. In lithologic Unit I, an excellent correlation is also observed between magnetic susceptibility data and color reflectance measurements, primarily the total reflectance value (L*) and the 550-nm wavelength (see "Lithologic Unit I," p. 7, in "Lithostratigraphy"). Both magnetic susceptibility and color reflectance data in this interval reveal a pronounced cyclicity, which may be useful in identifying astronomically controlled depositional processes. As already observed at Sites 1209, 1210, and 1211, a small peak (at ~58–63 mbsf) followed by a sharp decrease in magnetic susceptibility characterizes the lower middle Eocene–lower Miocene unconformity (see "Biostratigraphy," p. 12).

F26. Whole-core MST magnetic susceptibility, p. 55.

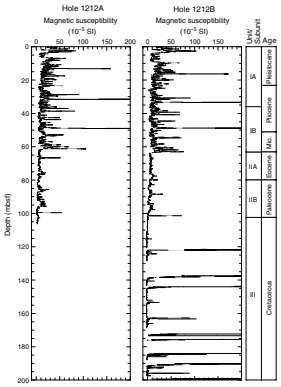

F27. Whole-core MST GRA and discrete bulk density vs. depth, p. 56.

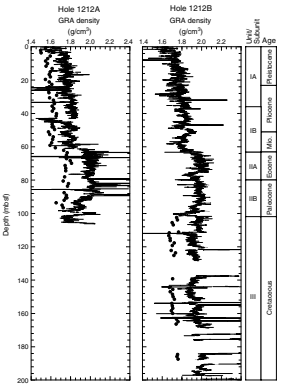

F28. Whole-core MST and discrete *P*-wave velocity vs. depth, p. 57.

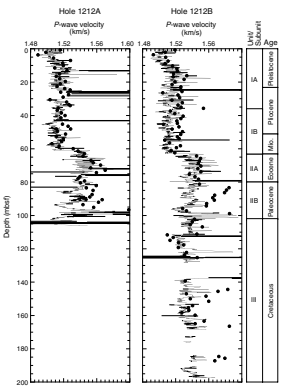

Magnetic susceptibility values are higher in the Eocene and Paleocene segments of lithologic Unit II, between ~62 and ~102 mbsf, than those recorded in Unit III (Cretaceous). Higher magnetic susceptibility values were also recorded within the Paleocene interval of lithologic Subunit IIB than those recorded in Subunit IIA. As observed at Sites 1209, 1210, and 1211, large peaks in magnetic susceptibility values delineate the K/T boundary, which occurs at ~102 mbsf in Holes 1212A and 1212B (see "Biostratigraphy," p. 12). These magnetic susceptibility increases are associated with an increase in clay content and a decrease in carbonate content in this stratigraphic interval (see "Organic Geochemistry," p. 20). In Cretaceous lithologic Unit III, magnetic susceptibility values are generally close to background values, with the exception of some excursions that are related to chert horizons, and do not exhibit any consistent downhole variation.

Site 1212 MST GRA bulk density data (Fig. F27) do not exhibit a constant downhole increase, as would be expected if increased sediment compaction and dewatering with greater overburden pressure were the only factors controlling this physical property. However, GRA bulk density data do show some distinct variations that relate to lithologic changes at distinct horizons. For example, there are significant increases in measured GRA bulk density values at the lower middle Eocene–lower Miocene unconformity (~63 mbsf) and the K/T boundary (~102 mbsf). MST GRA bulk density values exhibit a general increase between the seafloor and ~45 mbsf, within Pleistocene–Pliocene lithologic Subunit IA, before decreasing to lower values through the Pliocene–Miocene components of lithologic Subunits IA and IB, between ~45 and ~63 mbsf. Hole 1212A MST GRA bulk density values show a significant minimum at ~43 mbsf, followed by a rapid increase between ~43 and 50 mbsf. Discrete bulk density measurements in Holes 1212A and 1212B and MST GRA bulk density values in Hole 1212B do not reflect this trend. MST GRA bulk density values exhibit a sharp increase at ~63 mbsf occurring at the lower middle Eocene–lower Miocene lithologic boundary. Cyclic variations in GRA bulk density values, similar to that evident in magnetic susceptibility and color data (see "Lithologic Unit I," p. 7, in "Lithostratigraphy"), are found within Pleistocene–Miocene lithologic Unit I. A distinct minimum in MST GRA bulk density values occurs in the lowermost Eocene. Within the lower part of lithologic Unit II (Paleocene) MST GRA bulk density values decrease with increased burial depth, with a distinct minimum at ~100 mbsf occurring at the K/T boundary (i.e., between lithologic Units II and III). Within Cretaceous lithologic Unit III, below a stepped decrease at ~111 mbsf, MST GRA bulk density values gradually increase with burial depth to the bottom of Hole 1212B.

Hole 1212A GRA bulk density values are consistently higher than the discrete wet bulk density measurements (see Fig. F27; Table T12). These overestimated GRA bulk density values can be explained by the relatively high carbonate content, porosity, and moisture content of sediments; the calibration procedure for the MST GRA sensor is optimized for mixed-lithology sediments. Consequently, the GRA method overestimates the density in carbonate-rich sediments of all lithologic units. This phenomenon is most pronounced in lithologic Unit III because these sediments have the highest carbonate contents (see "Organic Geochemistry," p. 20).

MST *P*-wave velocities are plotted in Figure F28. Despite some obviously "out of range" values, reliable *P*-wave velocities vary between ~1500 and ~1580 m/s, with the highest velocities generally recorded at

T12. Discrete index properties measurements, p. 77.

greater depths in the sediment column. A linear relationship between increased burial depth and higher MST *P*-wave velocities is not observed at Site 1212. This suggests that sediment compaction and dewatering processes are not the only factors influencing *P*-wave velocity values. MST *P*-wave velocities do, however, follow the same downhole trends as the MST GRA bulk density data (see Fig. **F27**). MST *P*-wave values increase between the seafloor and ~15 mbsf, within the Pleistocene part of lithologic Subunit IA, then generally decrease between ~15 and ~63 mbsf (through the Pliocene–Miocene parts of lithologic Subunits IA and IB). One exception to this trend occurs from ~25 to 30 mbsf in Hole 1212A, where a marked increase in MST *P*-wave values is recorded. At ~63 mbsf, an abrupt increase in *P*-wave values from ~1510 to 1550 m/s correlates with the lower middle Eocene–lower Miocene unconformity. From ~65 to ~97 mbsf, *P*-wave velocities decrease with increasing burial depth (within the Eocene–Paleocene portions of lithologic Unit II). From ~97 to 102 mbsf, an abrupt decrease, followed by a significant increase, in *P*-wave values mark the lowermost Paleocene and the Cretaceous/Paleocene boundary. In the upper part of Cretaceous lithologic Unit III, from ~102 to ~110 mbsf, MST *P*-wave velocities show a gradual decrease to ~1540 m/s, then a significant decrease to ~1530 m/s, before gradually increasing with burial depth in the basal portion of Hole 1212B.

The downhole trends recorded by the reliable MST *P*-wave logger (PWL) values also compare well with the trends of the discrete measurements of *P*-wave velocity (Fig. **F28;** see also Table **T13;** Fig. **F29**). However, MST PWL values are generally lower than discrete values; this difference may be due to an assumption in the calibration of the MST PWL that the core liner is full of sediment and that there is no water between the liner and the sediment.

NGR data were collected at 30-cm intervals in Core 198-1212A-12H (Fig. **F30**) in the interval immediately above the K/T boundary. All measured values fall within the base of Subunit IIB (Paleocene). A relative peak in NGR values occurs at ~94.7 mbsf.

P-Wave Velocity

Discrete measurements of compressional *P*-wave velocity were made on Site 1212 split-core sections using the modified Hamilton Frame (PWS3) velocimeter. Data were collected at a routine sampling frequency of one measurement per section (Table **T13;** Fig. **F29**). Velocities vary between ~1500 m/s in the soft surface sediments and ~1580 m/s in the more consolidated sediments at Site 1212. Discrete *P*-wave measurements show a general increase in velocity, from ~1500 to ~1520 m/s, between the seafloor and ~20 mbsf, within Pleistocene–Pliocene lithologic Subunit IA. Below 20 mbsf, velocities remain relatively constant with depth to ~63 mbsf (Eocene/Miocene unconformity). *P*-wave velocities increase to ~1550 m/s between ~58 and ~63 mbsf in Hole 1212A and more abruptly in Hole 1212B at ~63 mbsf (lower middle Eocene–lower Miocene unconformity). Velocities then exhibit a general downhole increase through the Eocene segments of lithologic Unit II, to ~1590 (Hole 1212A) or ~1580 (Hole 1212B) m/s. In Hole 1212A, discrete *P*-wave values decrease through the lower Eocene and Paleocene parts of lithologic Unit II. In Hole 1212B, a peak in discrete *P*-wave values occurs at ~82 mbsf and delineates the P/E boundary. At the base of Hole 1212B, *P*-wave velocities between ~180 and ~190 mbsf are higher than those recorded in the upper part of lithologic Unit III.

T13. Discrete measurements of *P*-wave velocity, p. 79.

F29. Discrete *P*-wave velocities, p. 58.

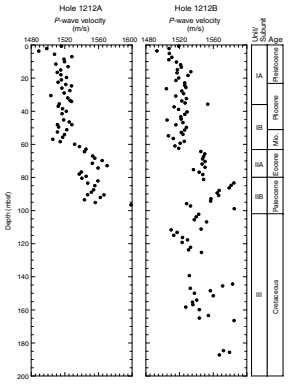

F30. MST natural gamma radiation vs. depth, p. 59.

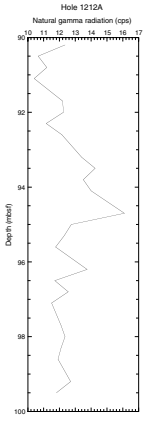

A positive correlation between *P*-wave velocity and discrete bulk density in Hole 1212A (Fig. F31) indicates that these two properties are closely related at Site 1212. The lack of evidence for early diagenetic cementation near the seafloor, as shown by high-percentage porosity in the interval 0–60 mbsf (Fig. F32; Table T12), suggests that increasing *P*-wave velocity and bulk density with depth in the upper ~25 m of Site 1212 is primarily the result of compaction and pore fluid expulsion. The lack of any constant increase in either of these two physical properties with greater burial depth further suggests that compaction and pore fluid expulsion are not the only factors influencing the more deeply buried sediments at this locality. It is highly probable that primary sediment composition was an additional important factor that influenced postdepositional changes following sediment burial on the Southern High of Shatsky Rise, as also indicated at Sites 1209, 1210, and 1211 (see "Physical Properties," p. 29, in the "Site 1209" chapter, "Physical Properties," p. 26, in the "Site 1210" chapter, and "Physical Properties," p. 25, in the "Site 1211" chapter).

Index Properties

Index properties determined for discrete samples from Hole 1212A are listed in Table T12 and shown in Figures F32 and F33. Index properties reflect progressive sediment compaction and fluid expulsion with depth in the sediment column, and also indicate changes in sediment composition as defined by lithologic units and subunits (see "Lithostratigraphy," p. 7). Bulk and dry density values increase between the seafloor and ~40 mbsf, through Pleistocene–Miocene lithologic Unit I. A slight decrease in bulk and dry density values occurs between ~40 and 63 mbsf. A large stepped increase in both bulk and dry density is evident at ~63 mbsf, delineating the unconformable boundary between lithologic Units I and II. Below ~63 mbsf, bulk and dry density exhibit a general trend to lower values through the Eocene–Paleocene segments of lithologic Unit II and Cretaceous lithologic Unit III. Slightly increased values in bulk and dry densities occur between ~160 and 180 mbsf. By comparison, grain density does not exhibit any clear downhole variation, which might explain the relatively good correlation between GRA bulk density and *P*-wave velocity (Fig. F31). Water content, porosity, and void ratio all exhibit a general downhole decrease between the seafloor and ~40 mbsf, through Pleistocene–Pliocene lithologic Unit I, the corollary to increasing bulk and dry density (see Fig. F33). A very slight increase in these values occurs between ~40 and 63 mbsf. At ~63 mbsf, water content, porosity, and void ratio exhibit a significant decrease that corresponds to the Eocene/Miocene unconformity. Between ~63 to 160 mbsf, within the Eocene and Paleocene portions of lithologic Unit II and Cretaceous lithologic Unit III, water content, porosity, and void ratio show general trends to higher values with increasing burial depth. These trends suggest that overburden on these sediments was not sufficient to cause significant downhole water loss and consequent decrease in porosity in the ~63 and 160 mbsf depth range. Below ~160 mbsf, there is a slight decrease in porosity, water content, and void ratio.

Summary

As observed at Sites 1209, 1210, and 1211, physical properties data at Site 1212 show variation with depth below seafloor that may be con-

F31. *P*-wave velocity vs. wet bulk density, p. 60.

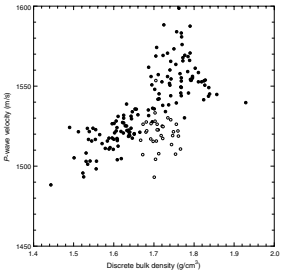

F32. Water content, porosity, and void ratio vs. depth, p. 61.

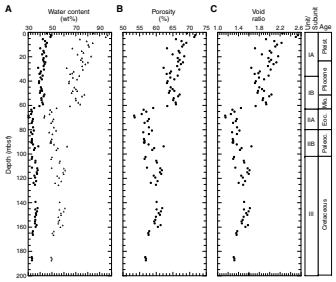

F33. Wet bulk, dry, and grain density vs. depth, Holes 1212A and 1212B, p. 62.

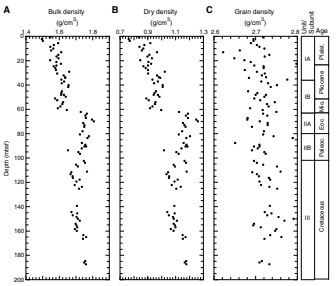

trolled by progressive compaction and fluid expulsion only in the uppermost part of the sedimentary column (i.e., between 0 and 40 mbsf). In addition, as at Sites 1209, 1210, and 1211, a simple relationship between lithology and physical properties is less obvious at Site 1212 than at Sites 1207 and 1208. As observed for Sites 1209, 1210, and 1211, the unusual downhole trends in physical properties data cannot be explained by the sediment burial history alone. The physical properties data suggest that there has been less compaction and diagenesis in the sediments below ~63 mbsf relative to those sediments in the overlying stratigraphic interval. This variability may be a reflection of varying microfossil composition within the Site 1212 sediments and the so-called "diagenetic potential" of different sediments (see **"Physical Properties,"** p. 29, in the "Site 1209" chapter).

REFERENCES

Baker, P.A., 1986. Pore-water chemistry of carbonate-rich sediments, Lord Howe Rise, Southwest Pacific Ocean. *In* Kennett, J.P., von der Borch, C.C., et al., *Init. Repts. DSDP,* 90 (Pt. 2): Washington (U.S. Govt. Printing Office), 1249–1256.

Baker, P.A., Gieskes, J.M., and Elderfield, H., 1982. Diagenesis of carbonates in deep-sea sediments—evidence from Sr^{2+}/Ca^{2+} ratios and interstitial dissolved Sr^{2+} data. *J. Sediment. Petrol.,* 52:71–82.

Broecker, W.S., and Peng, T.H., 1982. *Tracers in the Sea:* Palisades, New York (Lamont-Doherty Geol. Observ.).

Cande, S.C., and Kent, D.V., 1995. Revised calibration of the geomagnetic polarity timescale for the late Cretaceous and Cenozoic. *J. Geophys. Res.,* 100:6093–6095.

Dickens, G.R., 2000. Methane oxidation during the Late Palaeocene Thermal Maximum. *Bull. Soc. Geol. Fr.,* 171:37–49.

Dickens, G.R., Castillo, M.M., and Walker, J.G.C., 1997. A blast of gas in the latest Paleocene: simulating first-order effects of massive dissociation of oceanic methane hydrate. *Geology,* 25:259–262.

Douglas, R.G., 1971. Cretaceous foraminifera from the northwestern Pacific Ocean: Leg 6, Deep Sea Drilling Project. *In* Fischer, A.G., Heezen, B.C., et al., *Init. Repts. DSDP,* 6: Washington (U.S. Govt. Printing Office), 1027–1053.

Douglas, R.G., and Savin, S.M., 1971. Isotopic analyses of planktonic foraminifers from the Cenozoic of the northwest Pacific, Leg 6. *In* Fischer, A.G., Heezen, B.C., et al., *Init. Repts. DSDP,* 6: Washington (U.S. Govt. Printing Office), 1123–1127.

————, S.M., 1975. Oxygen and carbon isotope analyses of Tertiary and Cretaceous microfossils from Shatsky Rise and other sites in the North Pacific Ocean. *In* Larson, R.L., Moberly, R., et al., *Init. Repts. DSDP,* 32: Washington (U.S. Govt. Printing Office), 509–520.

Fischer, A.G., Heezen, B.C., et al., 1971. *Init. Repts. DSDP,* 6: Washington (U.S. Govt. Printing Office).

Gerstel, J., Thunell, R.C., Zachos, J.C., and Arthur, M.A., 1986. The Cretaceous/Tertiary boundary event in the North Pacific: planktonic foraminiferal results from Deep Sea Drilling Project Site 577, Shatsky Rise. *Paleoceanography,* 1:97–117.

Gieskes, J.M., 1981. Deep-sea drilling interstitial water studies: implications for chemical alteration of the oceanic crust, Layers I and II. *In* Warme, J.E., Douglas, R.G., and Winterer, E.L. (Eds), *The Deep Sea Drilling Project: A Decade of Progress.* Spec. Publ.—SEPM (Soc. Sediment. Geol.), 32:149–167.

Heath, G.R., Burkle, L.H., et al., 1985. *Init Repts., DSDP,* 86: Washington (U.S. Govt. Printing Office).

Kaiho, K., 1999. Evolution in the test size of deep-sea benthic foraminifera during the past 120 million years. *Mar. Micropaleontol.,* 37:53–65.

Kelly, D.C., Bralower, T.J., Zachos, J.C., Premoli Silva, I., and Thomas, E., 1996. Rapid diversification of planktonic foraminifera in the tropical Pacific (ODP Site 865) during the late Paleocene thermal maximum. *Geology,* 24:423–426.

Luterbacher, H.P., 1975. Early Cretaceous foraminifera from the northwestern Pacific, Leg 32, Deep Sea Drilling Project. *In* Larson, R.L., Moberly, R., et al., *Init. Repts. DSDP,* 32: Washington (U.S. Govt. Printing Office), 703–718.

McDuff, R.E., 1985. The chemistry of interstitial waters, Deep Sea Drilling Project Leg 86. *In* Heath, G.R., Burckle, L.H., et al., *Init. Repts. DSDP,* 86: Washington (U.S. Govt. Printing Office), 675–687.

Millero, F.J., and Sohn, M.L., 1992. *Chemical Oceanography:* Boca Raton (CRC Press).

Monechi, S., 1985. Campanian to Pleistocene calcareous nannofossil stratigraphy from the northwest Pacific Ocean, Deep Sea Drilling Project Leg 86. *In* Heath, G.R., Burckle, L.H., et al., *Init. Repts. DSDP,* 86: Washington (U.S. Govt. Printing Office), 301–336.

Nyong, E.E., and Olsson, R.K., 1984. A paleoslope model of Campanian to lower Maestrichtian foraminifera in the North American Basin and adjacent continental margin. *Mar. Micropaleontol.,* 8:437–477.

Pflum, C.E., Frerichs, W.E., and Sliter, W.V., 1976. *Gulf of Mexico Deep-water Foraminifers*. Spec. Publ.—Cushman Found. Foraminiferal Res., 14.

Schrag, D.P., Hampt, G., and Murray, D.W., 1996. Pore fluid constraints on the temperature and oxygen isotonic composition of the glacial ocean. *Science,* 272:1930–1932.

Sliter, W.V., 1992. Cretaceous planktonic foraminiferal biostratigraphy and paleoceanographic events in the Pacific Ocean with emphasis on indurated sediment. *In* Ishizaki, K., and Saito, T. (Eds.), *Centenary of Japanese Micropaleontology:* Tokyo (Terra Sci.), 281–299.

Sliter, W.V., and Brown, G.R., 1993. Shatsky Rise: seismic stratigraphy and sedimentary record of Pacific paleoceanography since the Early Cretaceous. *In* Natland, J.H., Storms, M.A., et al., *Proc. ODP, Sci. Results,* 132: College Station, TX (Ocean Drilling Program), 3–13.

Stott, L.D., 1992. Higher temperatures and lower pCO_2: A climate enigma at the end of the Paleocene Epoch. *Paleoceanography,* 7:395–404.

Tjalsma, R.C., and Lohmann, G.P., 1983. *Paleocene–Eocene Bathyal and Abyssal Benthic Foraminifera from the Atlantic Ocean.* Spec. Publ.—Micropaleontol., 4.

van Morkhoven, F.P.C.M., Berggren, W.A., and Edwards, A.S., 1986. Cenozoic cosmopolitan deep-water benthic foraminifera. *Bull. Cent. Rech. Explor.—Prod. Elf-Aquitaine,* 11.

Woodruff, F., 1985. Changes in Miocene deep-sea benthic foraminiferal distribution in the Pacific Ocean: relationship to paleoceanography. *In* Kennett, J.P. (Ed.), *The Miocene Ocean: Paleoceanography and Biogeography.* Mem.—Geol. Soc. Am., 163:131–175.

Wright, A.A., Bleil, U., Monechi, S., Michel, H.V., Shackleton, N.J., Simoneit, B.R.T., and Zachos, J.C., 1985. Summary of Cretaceous/Tertiary boundary studies, Deep Sea Drilling Project Site 577, Shatsky Rise. *In* Heath, G.R., Burckle, L.H., et al., *Init. Repts. DSDP,* 86: Washington (U.S. Govt. Printing Office), 799–804.

Zachos, J.C., Arthur, M.A., Thunnell, R.C., Williams, D.F., Tappa, E.J., 1985. Stable isotope and trace element geochemistry of carbonate sediments across the Cretaceous/Tertiary boundary at Deep Sea Drilling Project Hole 577, Leg 86. *In* Heath, G.R., Burckle, L.H., et al., *Init. Repts. DSDP,* 86: Washington (U.S. Govt. Printing Office), 513–532.

Figure F1. Summary diagram of coring results at Site 1212 plotted on the meters composite depth (mcd) scale. The maximum penetration measured with the drill pipe was 207.6 mbsf. Multisensor track (MST) magnetic susceptibility (brown points) and GRA wet bulk density (dark blue points) were measured every 3.0 cm. The accurate correction factor for magnetic susceptibility raw instrument values is 0.68×10^{-5}. For details about figure symbols and descriptions see Figure F12, p. 101, in the "Leg Summary" chapter.

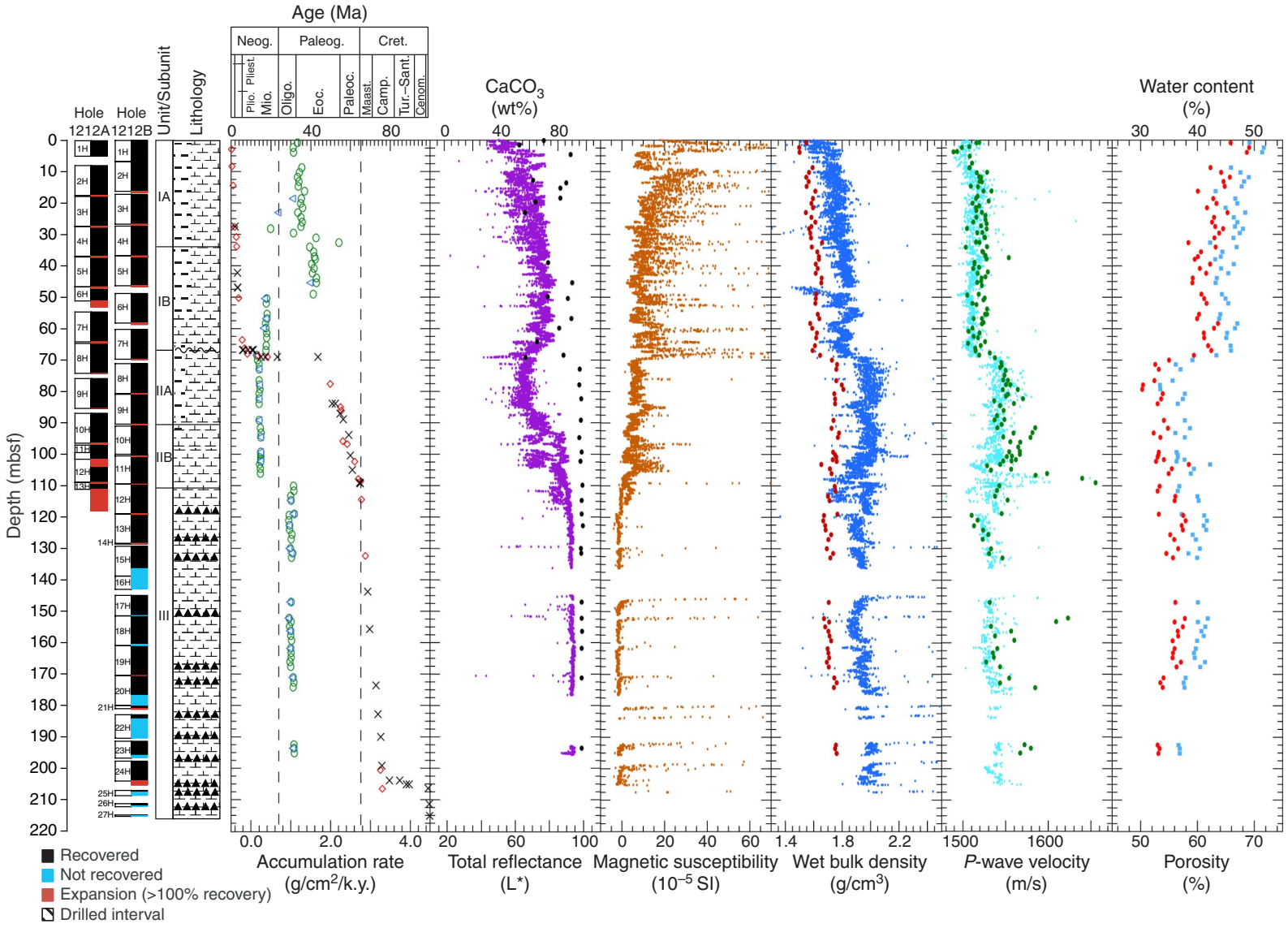

Figure F2. Age-depth curves for Sites 1209, 1210, 1211, and 1212 based on shipboard biostratigraphy. Circles = planktonic foraminiferal datums, squares = nannofossil datums, P. = Pleistocene, Pl. = Pliocene.

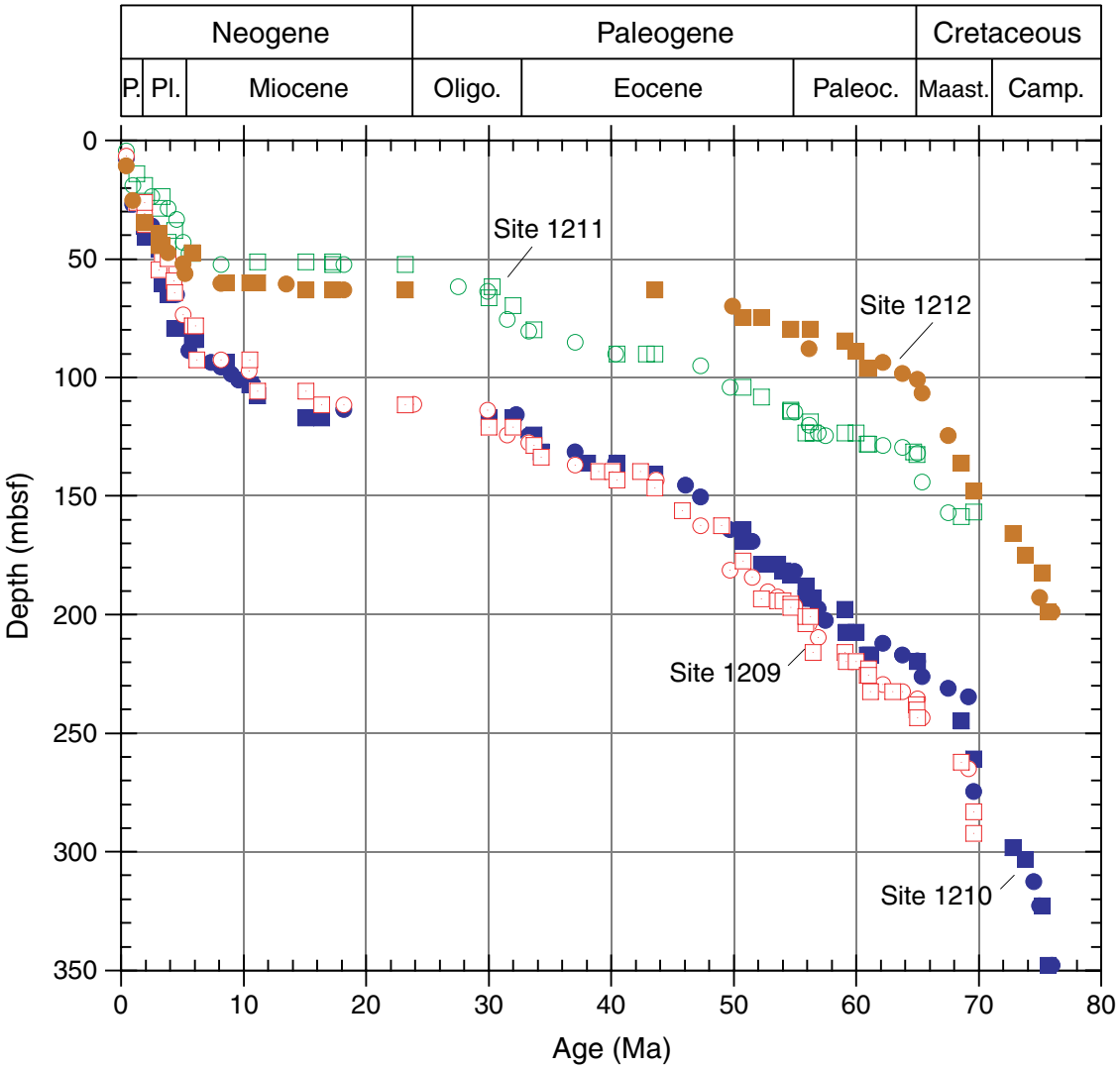

Figure F3. Summary of lithostratigraphy for Sites 1207–1214. TD = total depth.

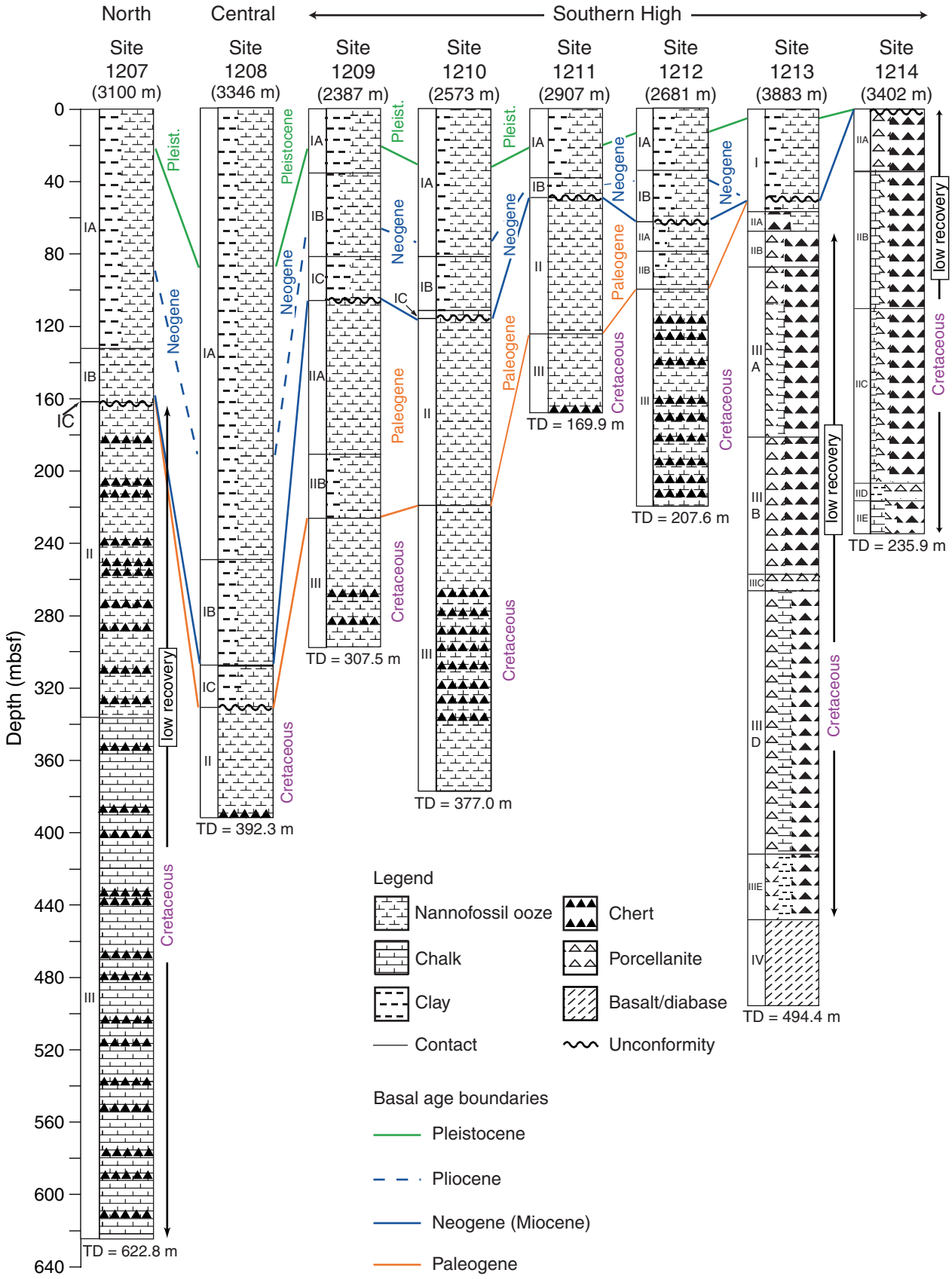

Figure F4. Core recovery, lithology, lithologic units, age with corresponding biostratigraphic zonations, color reflectance (L*), and percent carbonate for Hole 1212B. Foram. zn. = foraminiferal zone, nanno zn. = nannofossil zone.

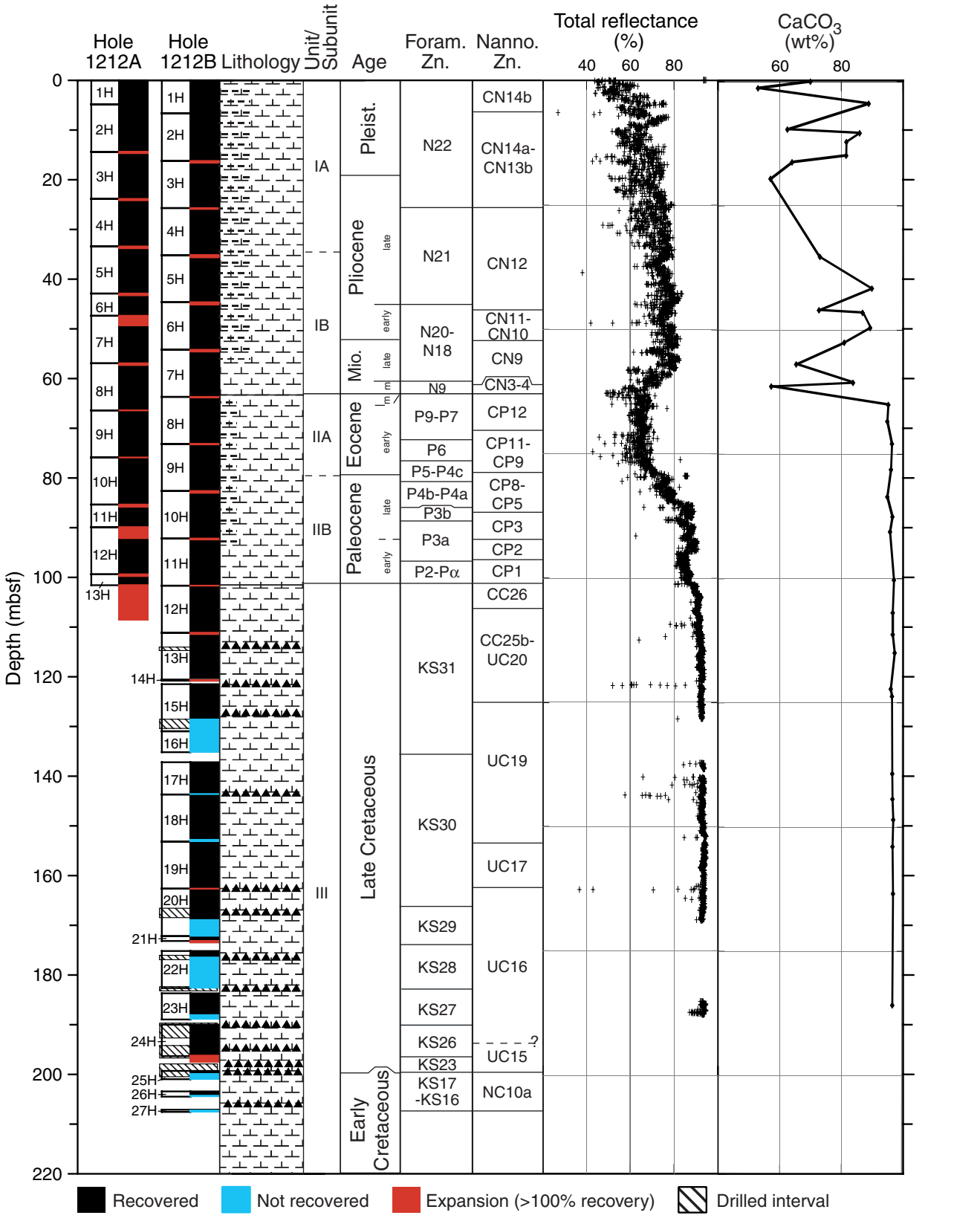

Figure F5. Estimates of biosiliceous material from Hole 1212A smear slides.

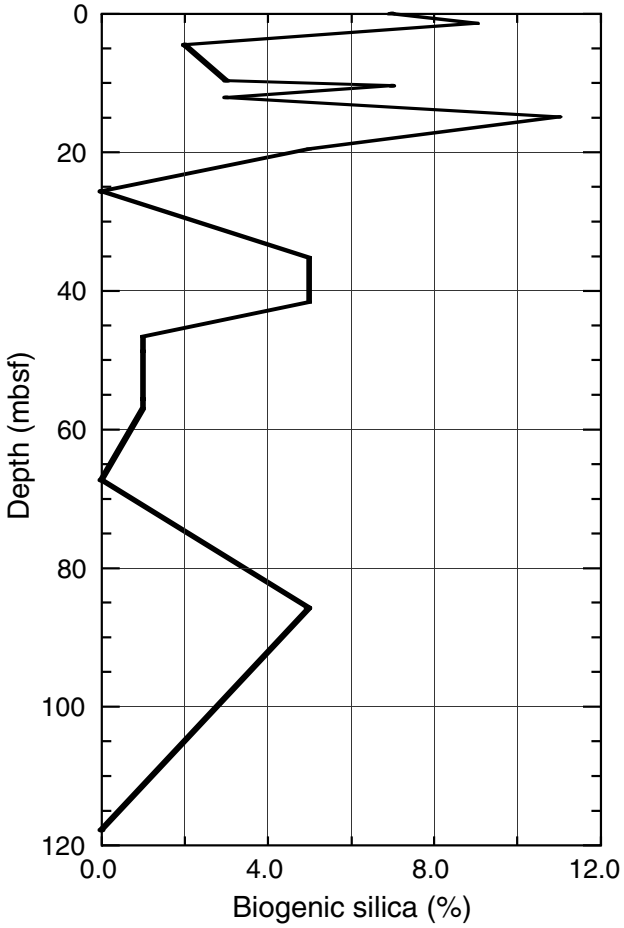

Figure F6. Color reflectance red/blue (680 nm/420 nm) ratio for Holes 1212A and 1212B. The increase in red/blue ratios at 63 mbsf indicates a shift toward more oxic redox conditions associated with lower sedimentation rates and more oxygen-rich bottom waters.

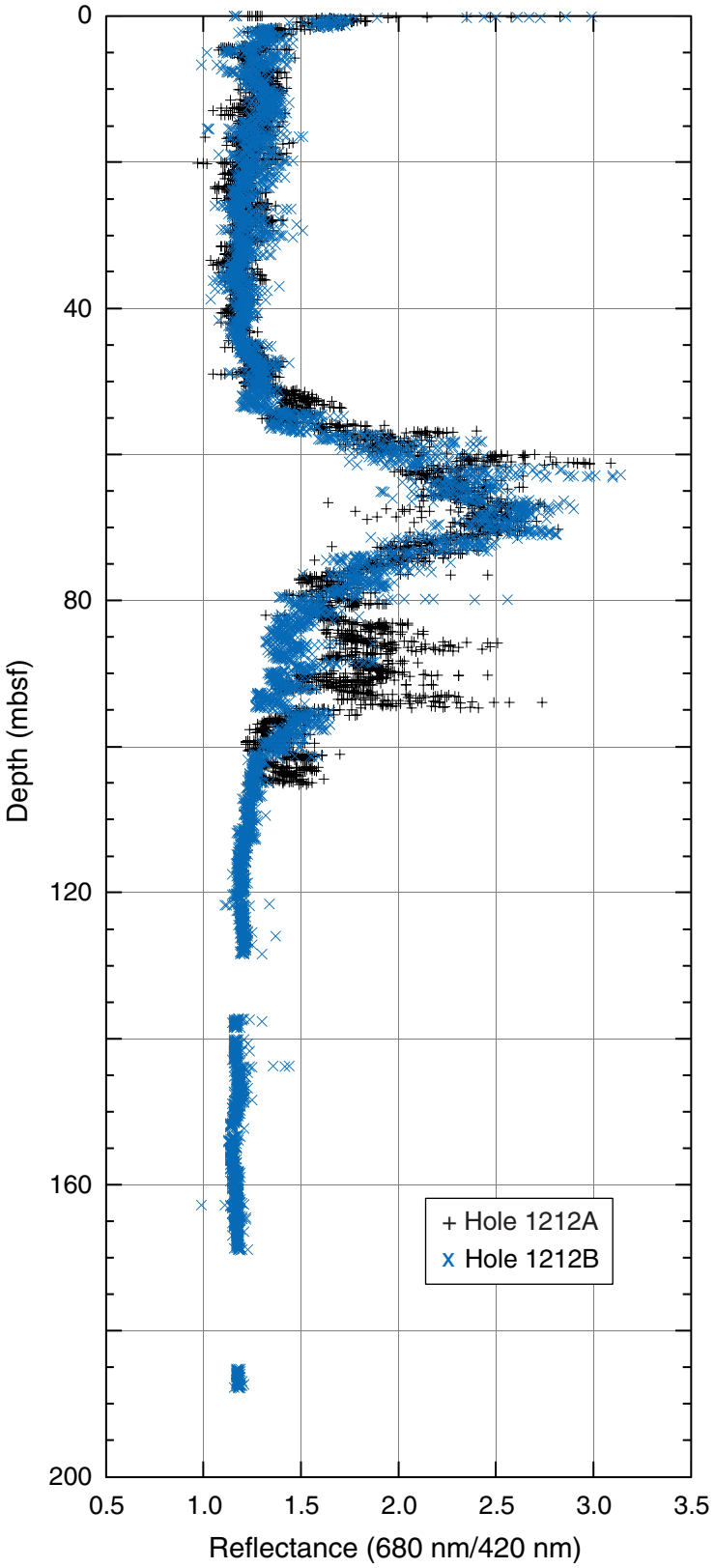

Figure F7. Color reflectance (L*) for Cores 198-1212B-3H and 5H. There is a distinct change in the amplitude of the color cycles between cores.

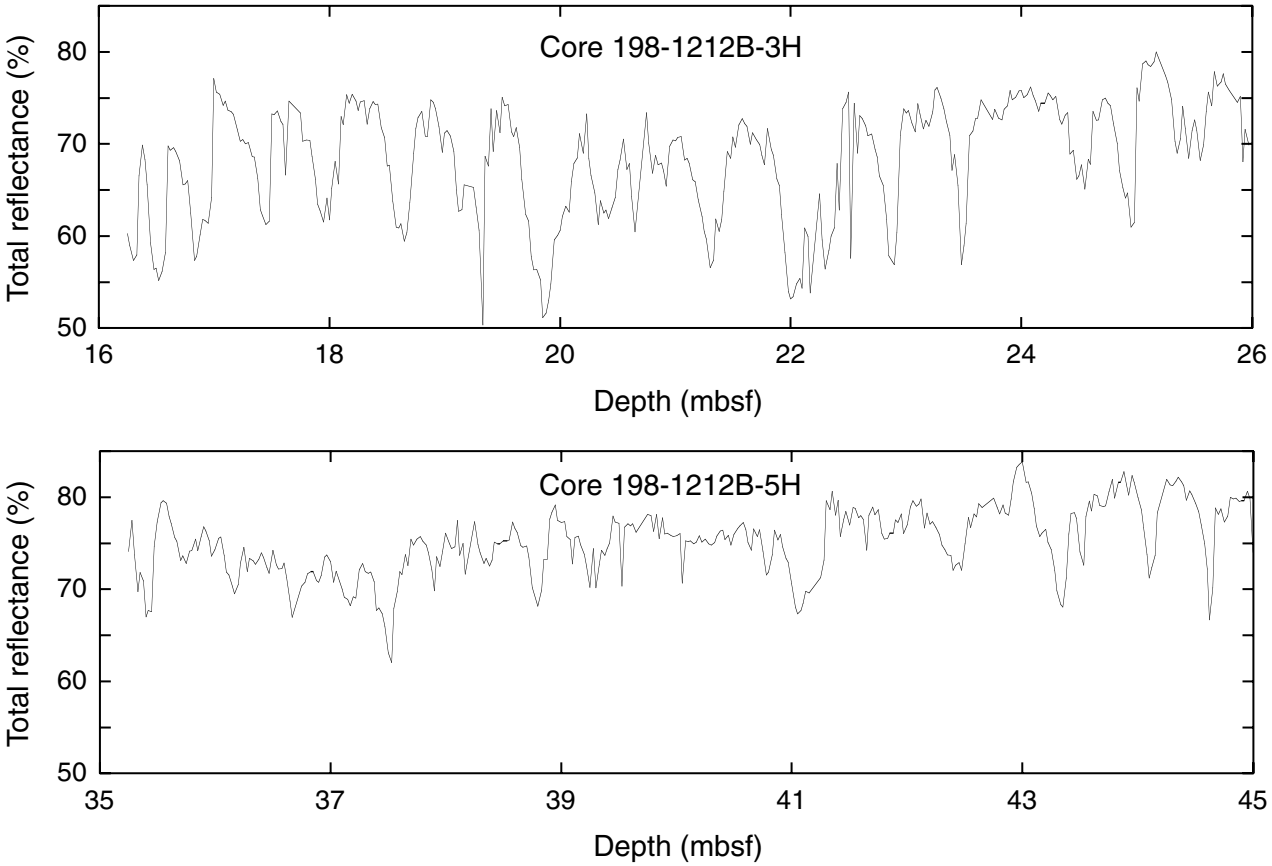

Figure F8. Composite digital photograph and total reflectance for a clay-rich layer at the P/E boundary in Section 198-1212A-10H-1.

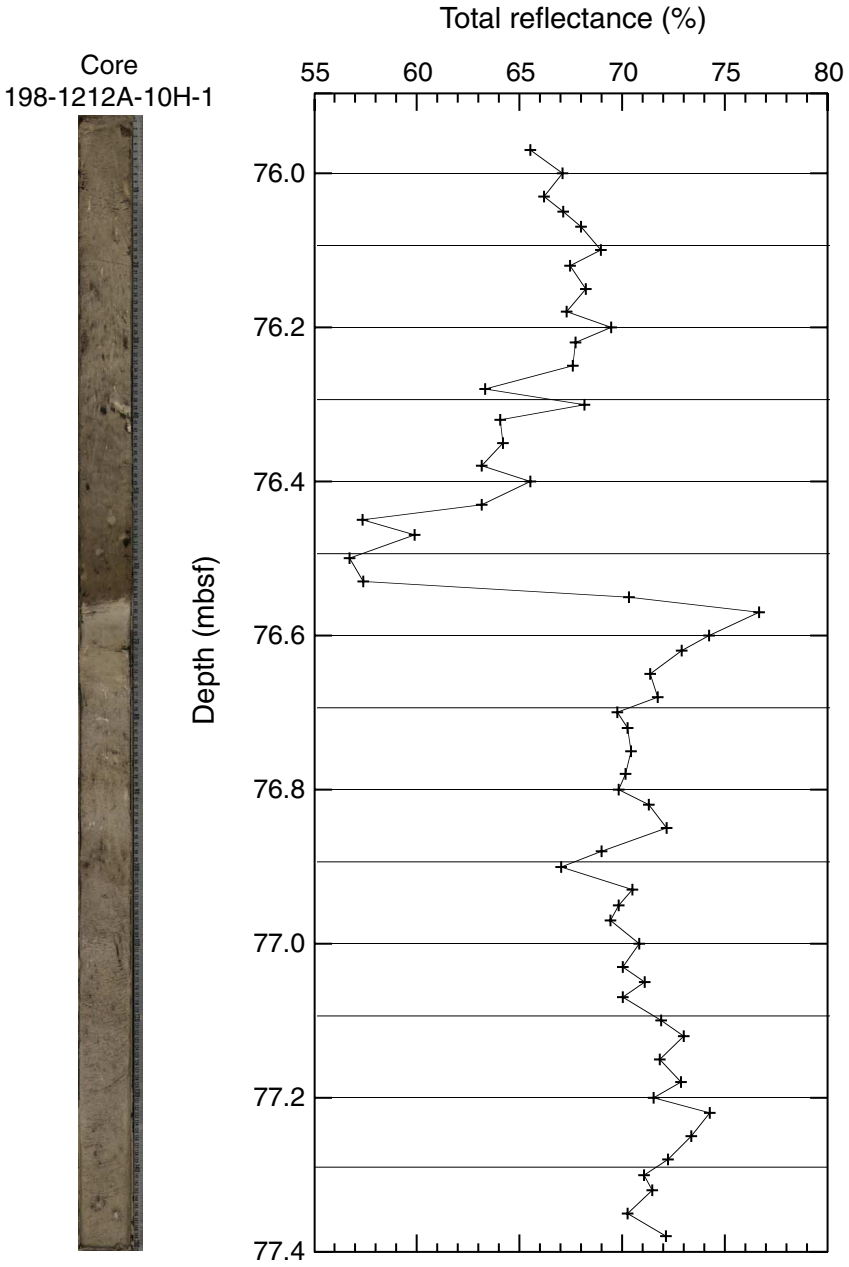

Figure F9. Site 1212 archive-half magnetization intensities after AF demagnetization at peak fields of 20 mT as measured with the shipboard pass-through magnetometer. Solid black circles = measurements from Hole 1212B, open purple circles = measurements from Hole 1212A.

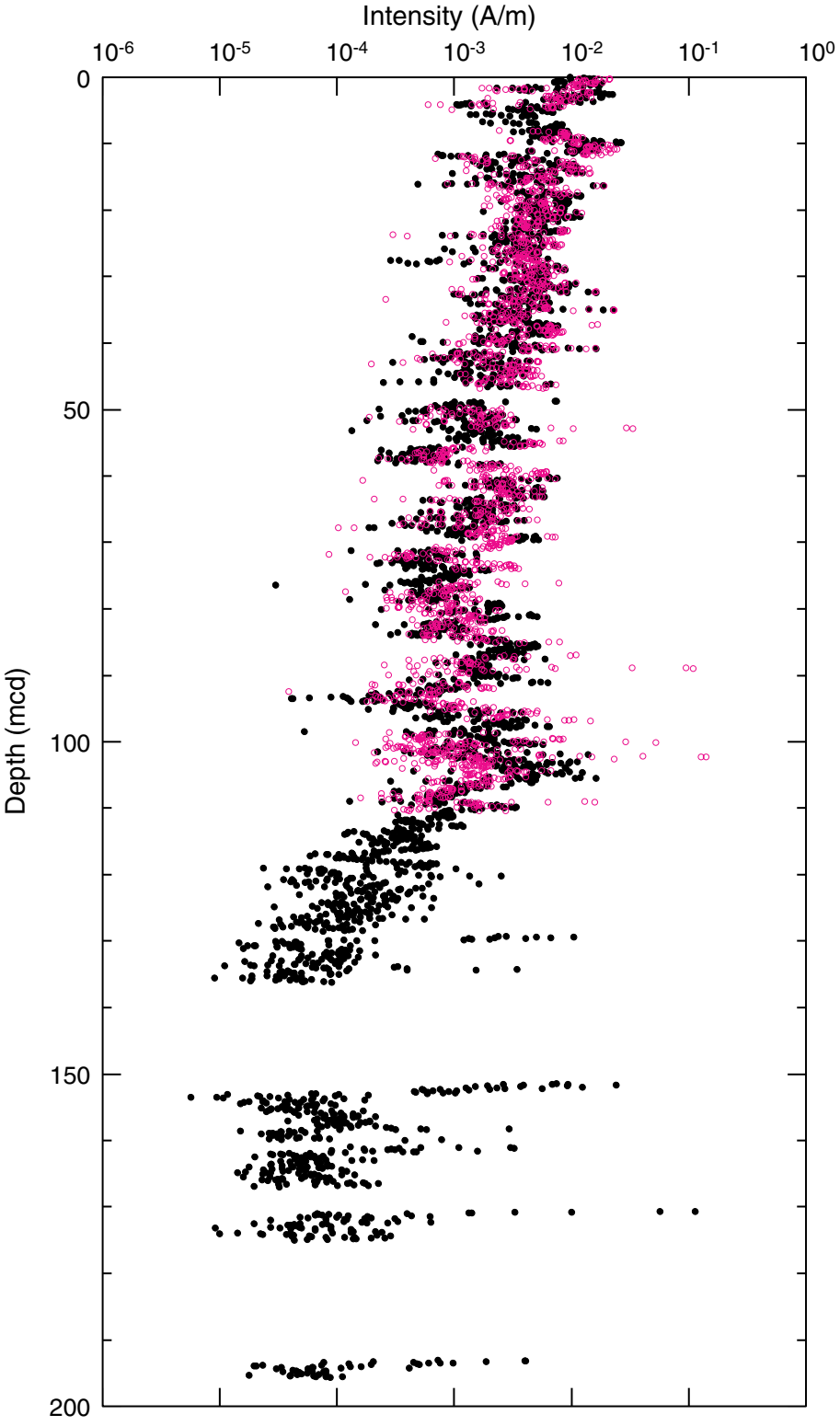

Figure F10. Inclination after AF demagnetization at peak fields of 20 mT as measured with the shipboard pass-through magnetometer for the upper 140 mcd from Holes 1212A (solid black circles) and 1211B (open purple circles). The center column shows interpreted zones of normal (black) and reversed (white) polarity for the 0–50 mcd interval.

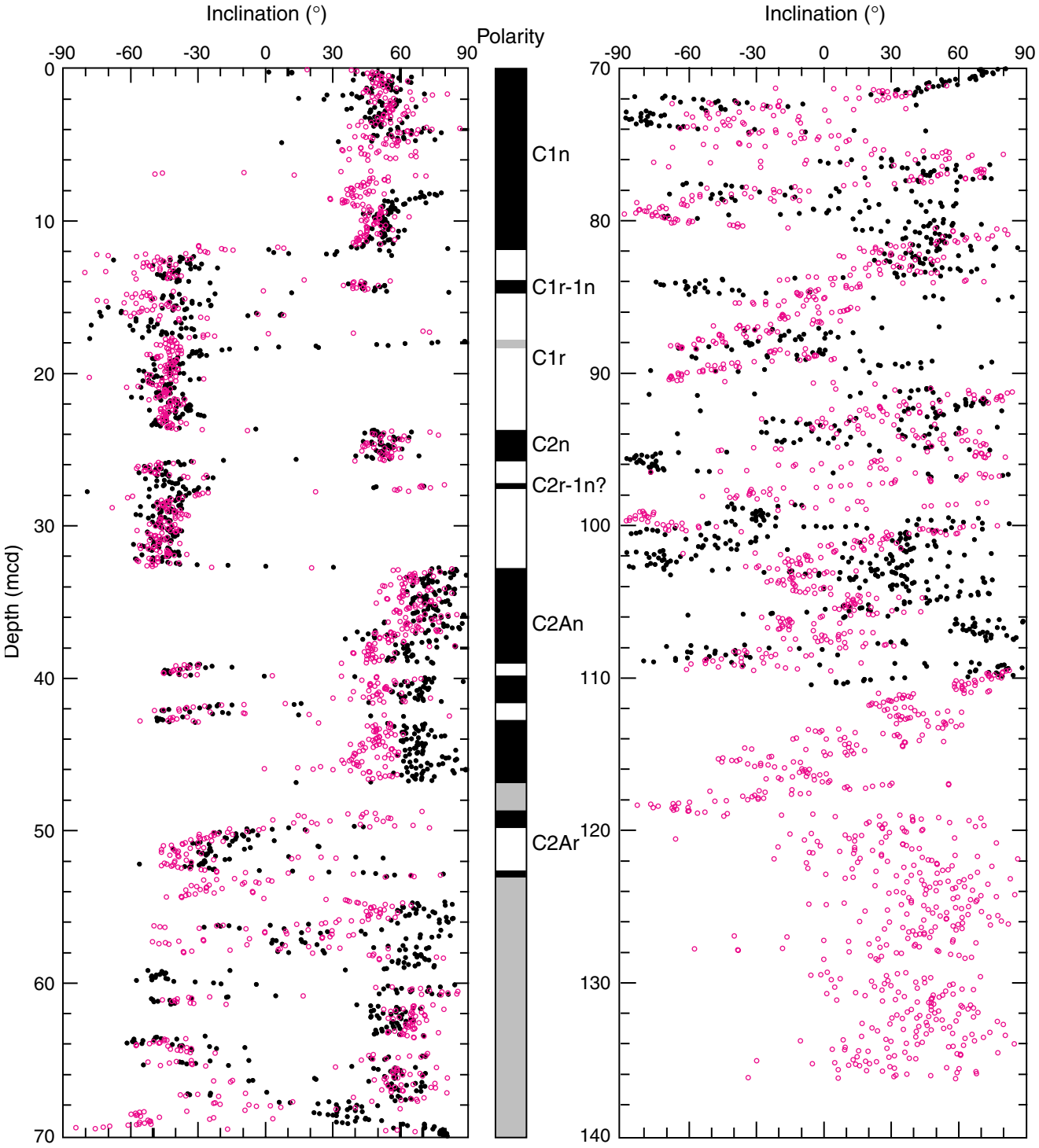

Figure F11. Age-depth curve (in mcd) for Site 1212 derived from the magnetic stratigraphy shown in Figure F10, p. 39, using the geomagnetic polarity timescale of Cande and Kent (1995). Average sedimentation rates in meters per million years are also plotted.

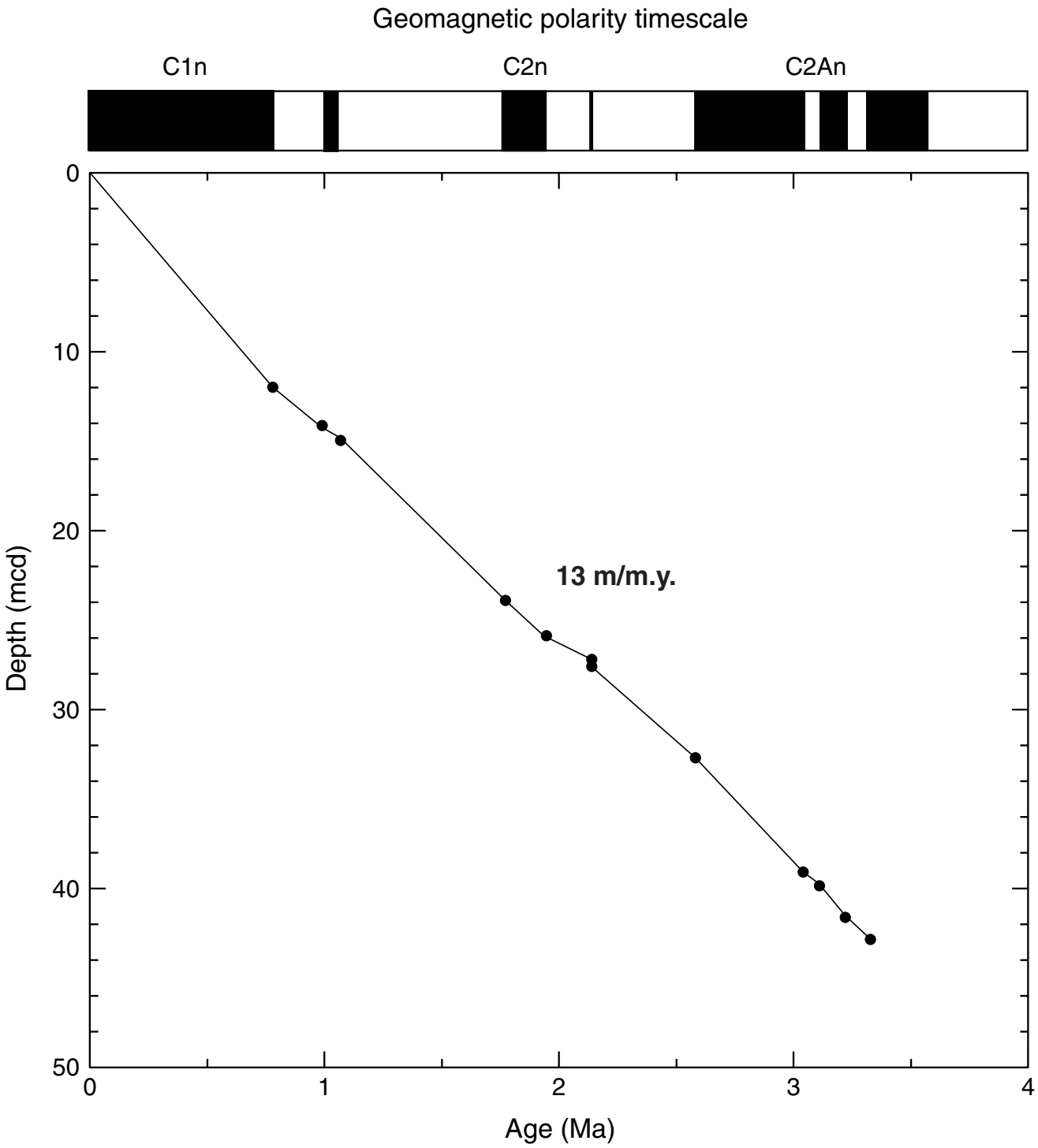

Figure F12. A. Magnetic susceptibility data for 0 to 115 mcd for Site 1212. The accurate correction factor for the raw instrument values is 0.68×10^{-6}. Hole 1212B is offset from Hole 1212A by a constant (40×10^{-6}). **B.** GRA bulk density data for 0 to 115 mcd for Site 1212. Hole 1212B is offset from Hole 1212A by a constant (0.3 g/cm^3).

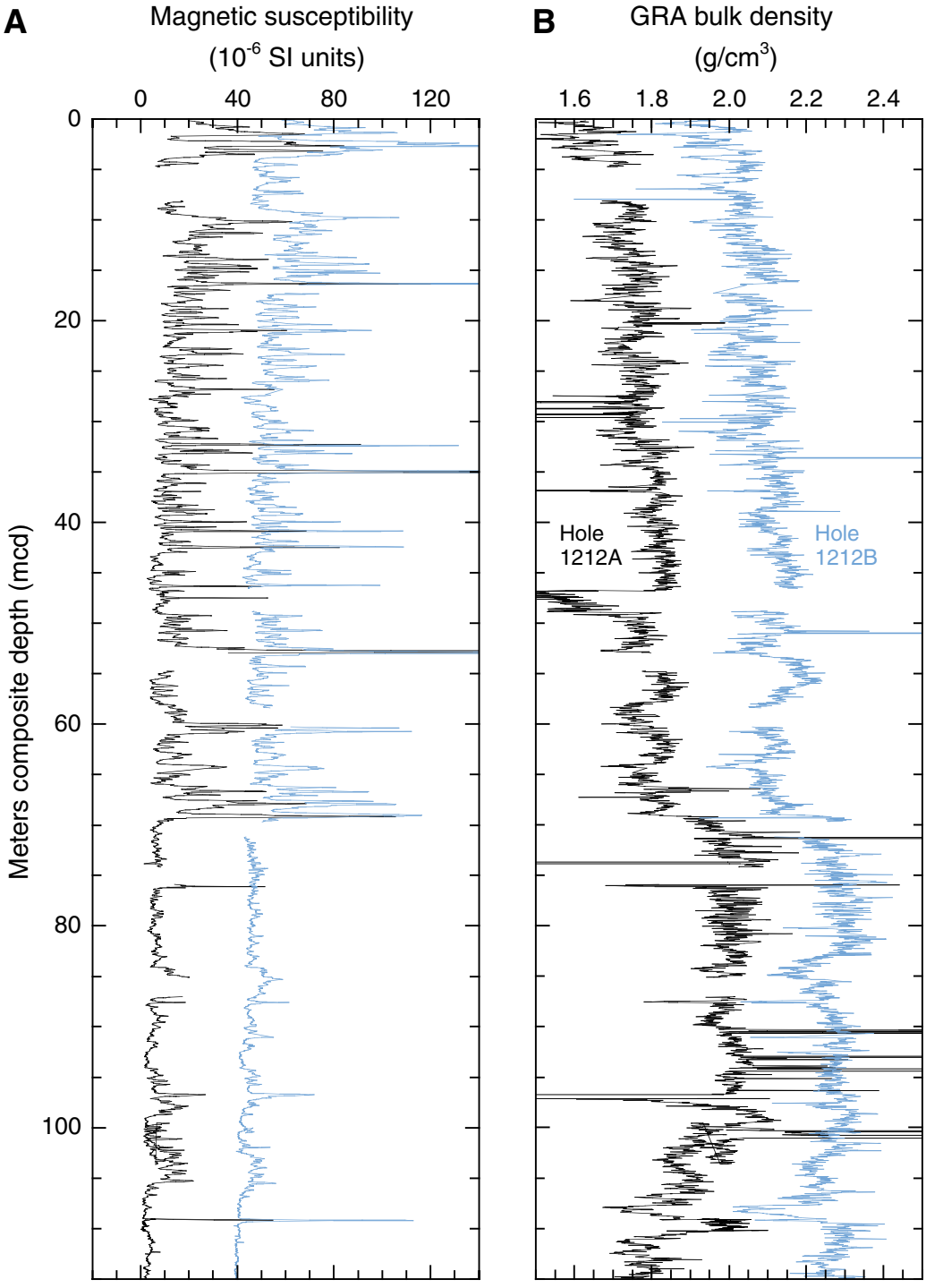

Figure F13. Magnetic susceptibility data for 0 to 50 mcd at Site 1212. Core 198-1212B-2H was tentatively appended to Core 198-1212B-1H, as there was no overlapping interval recovered in Hole 1212A. As a result minor offsets between holes have been found within the underlying ~40 mbsf leading to inadequate overlapping of accompanying cores. The accurate correction factor for the raw instrument values is 0.68×10^{-6}.

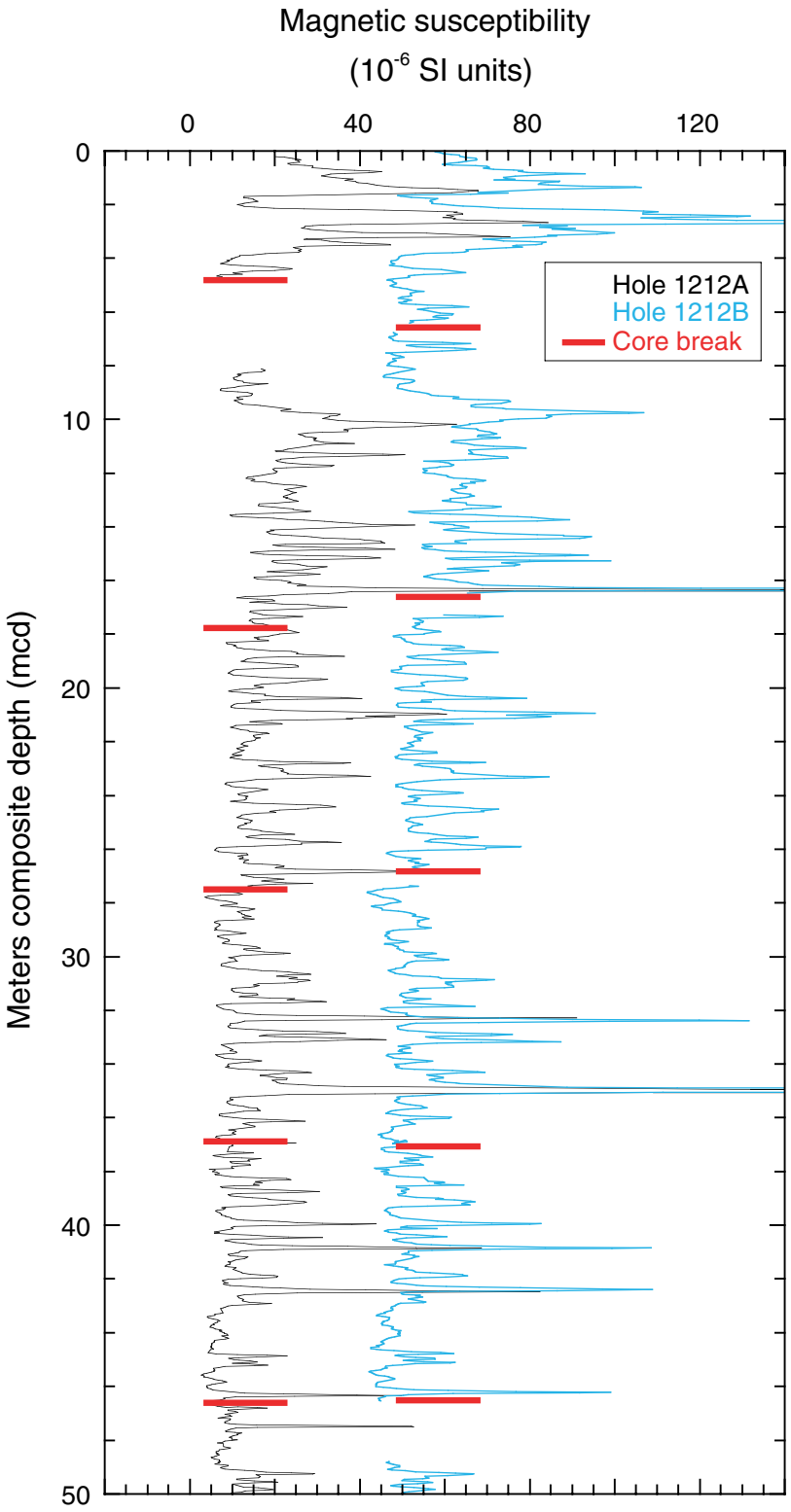

Figure F14. Age-depth plot of calcareous nannofossil (diamonds) and planktonic foraminiferal (crosses) datums at Site 1212. Horizontal lines represent unconformities in the section. Datum ages and depths are presented in Tables T2, p. 65, and T3, p. 66.

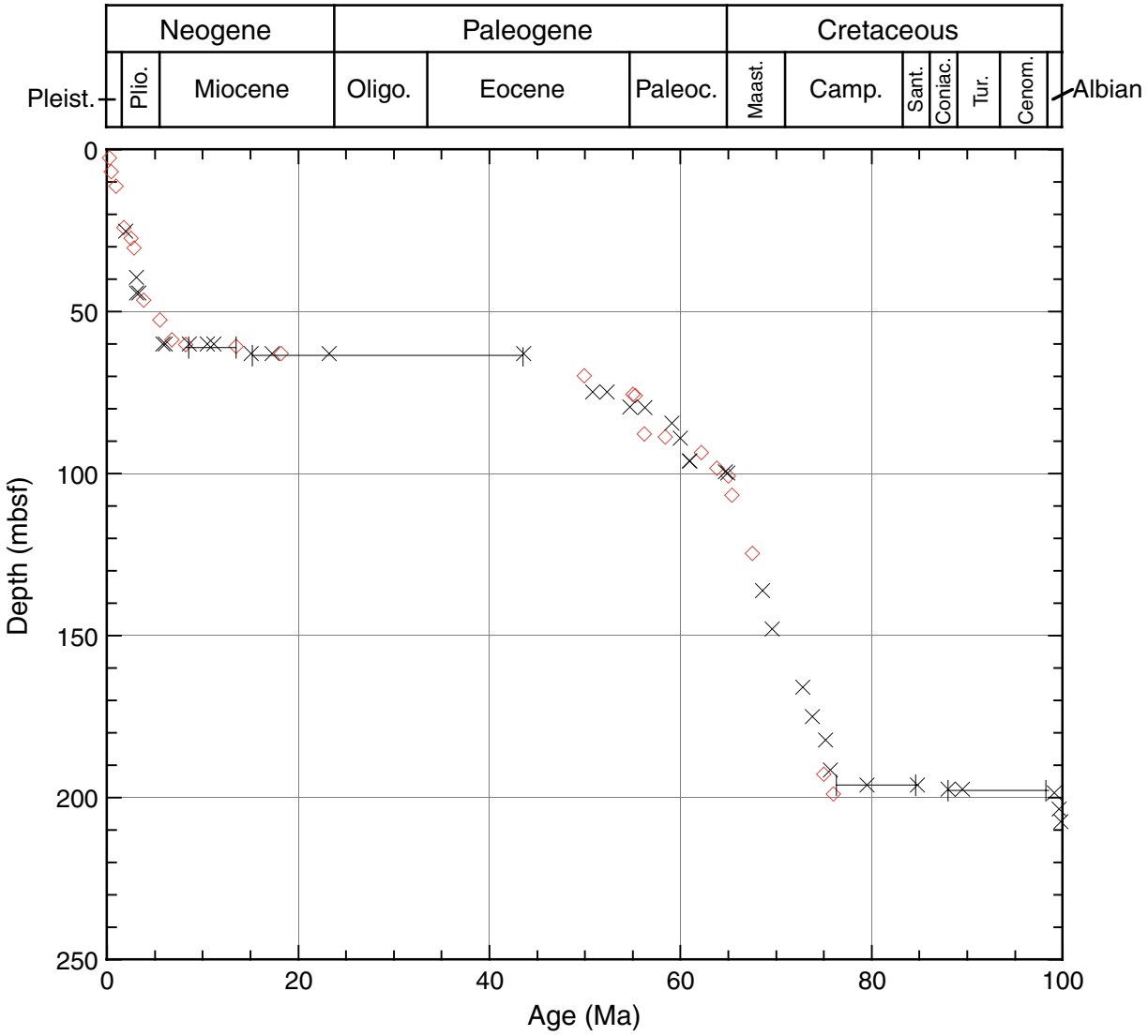

Figure F15. Age-depth plot of Neogene calcareous nannofossil (diamonds) and planktonic foraminiferal (crosses) datums at Site 1212. Horizontal lines represent unconformities in the section (see discussion in "Sedimentation and Accumulation Rates," p. 19). Datum ages and depths are presented in Tables T2, p. 65, and T3, p. 66. FO = first occurrence, LO = last occurrence.

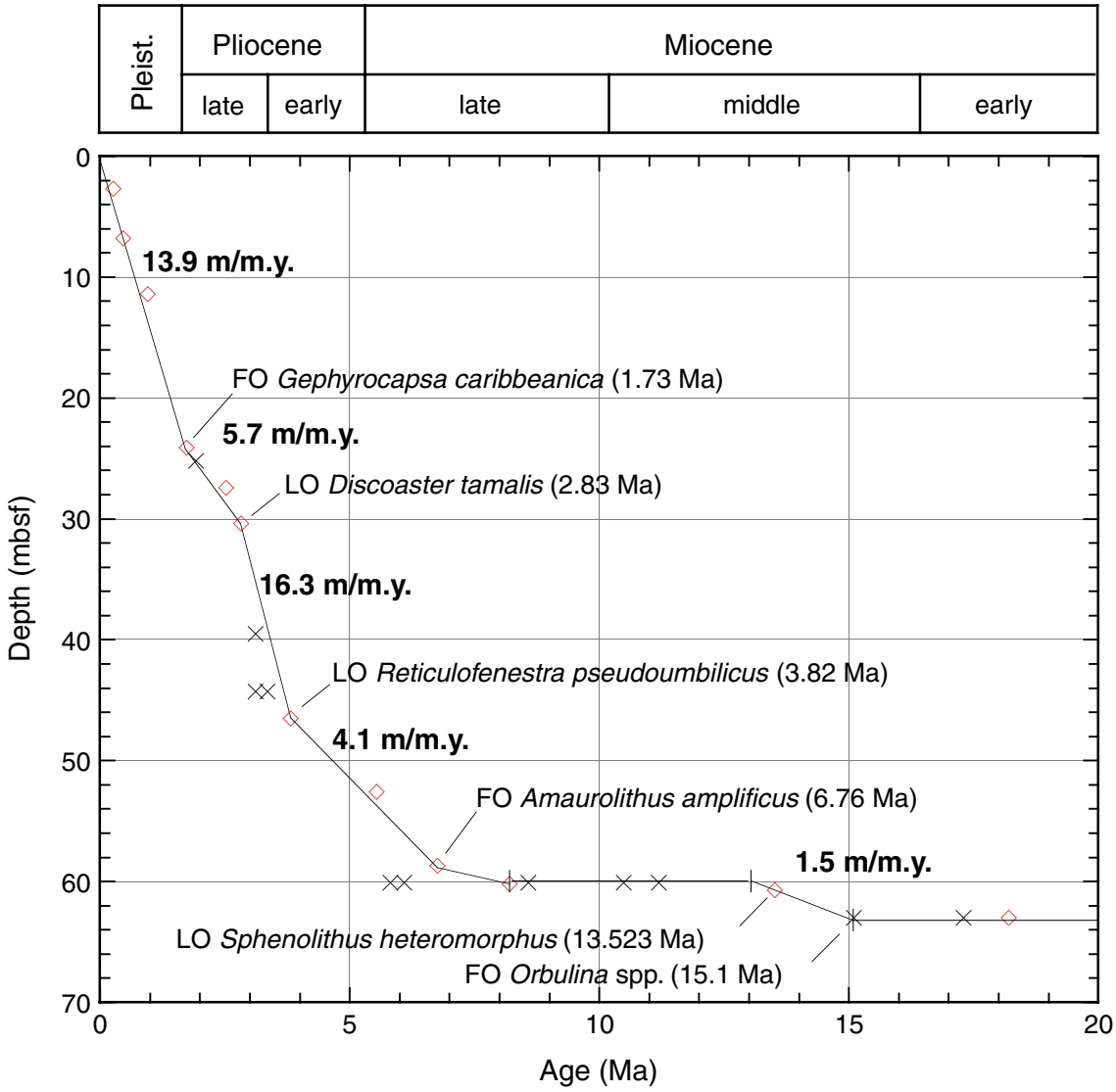

Figure F16. Age-depth plot of early Oligocene–late Paleocene calcareous nannofossil (diamonds) and planktonic foraminiferal (crosses) datums at Site 1212. Horizontal line represents an unconformity in the section (see discussion in **"Sedimentation and Accumulation Rates,"** p. 19). Two lines represent alternative interpretations of sedimentation rate history for the mid- to lower Eocene. Datum ages and depths are presented in Tables **T2,** p. 65, and **T3,** p. 66. FO = first occurrence, LO = last occurrence.

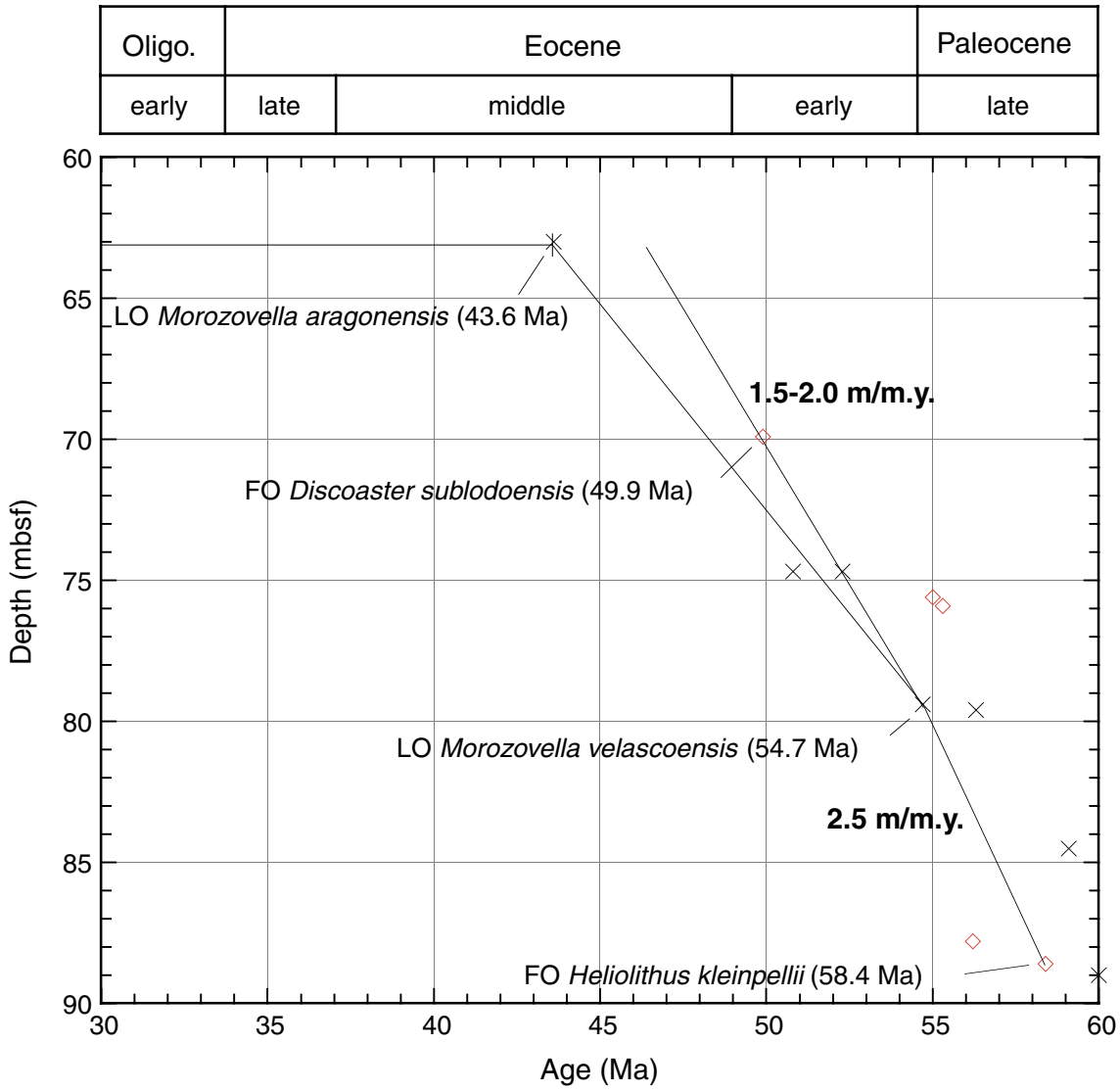

Figure F17. Age-depth plot of early Eocene–Campanian calcareous nannofossil (diamonds) and planktonic foraminiferal (crosses) datums at Site 1212. Horizontal line represents an unconformity in the section (see discussion in **"Sedimentation and Accumulation Rates,"** p. 19). Alternative sedimentation rate interpretations are shown by the multiple lines and by the range of possible rates for specific line segments. Datum ages and depths are presented in Tables **T2,** p. 65, and **T3,** p. 66. FO = first occurrence, LO = last occurrence.

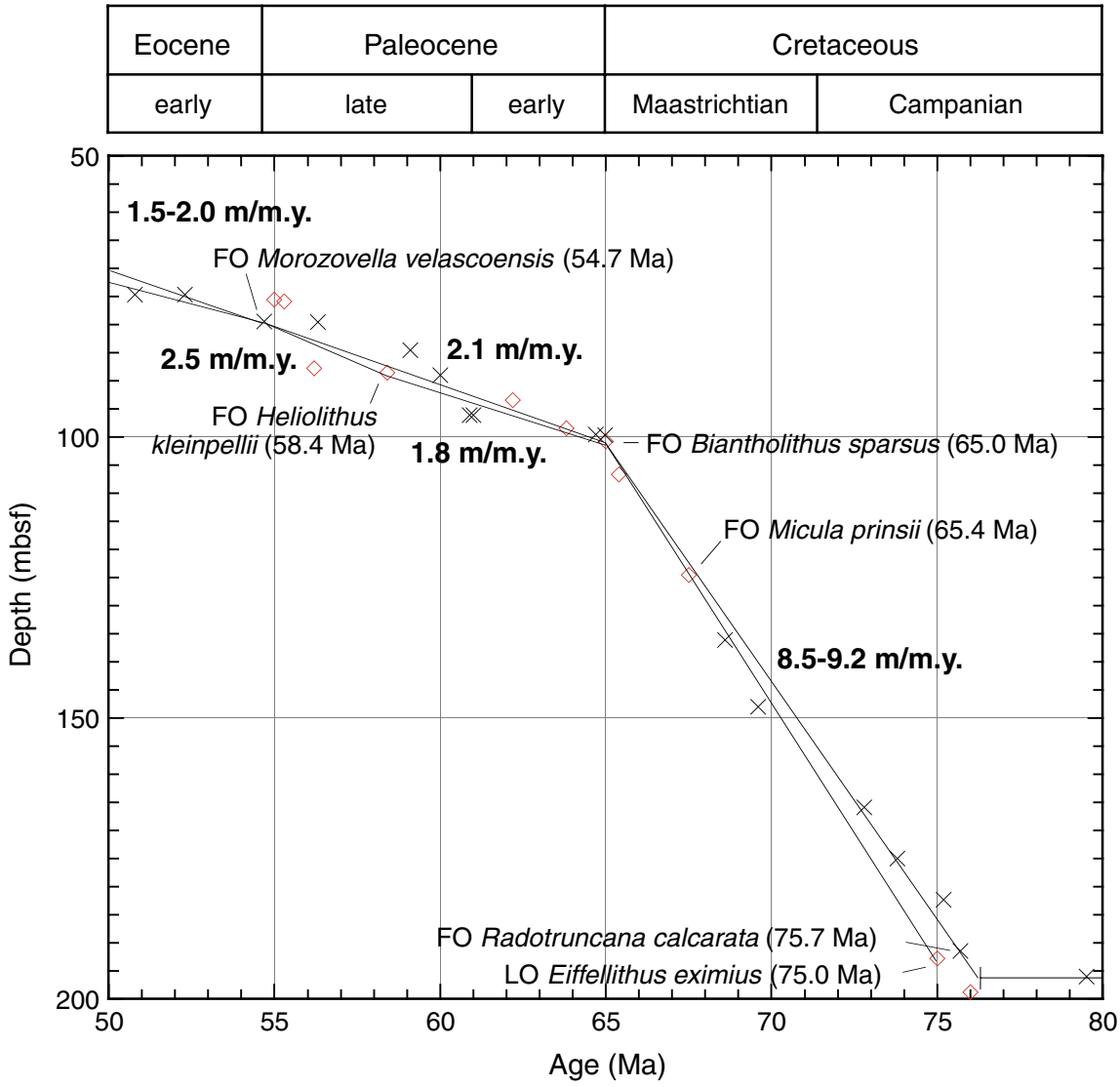

Figure F18. Age-depth plot of Maastrichtian–Albian calcareous nannofossil (diamonds) and planktonic foraminiferal (crosses) datums at Site 1212. Horizontal lines represent unconformities in the section (see discussion in **"Sedimentation and Accumulation Rates,"** p. 19). Datum ages and depths are presented in Tables **T2,** p. 65, and **T3,** p. 66. FO = first occurrence, LO = last occurrence.

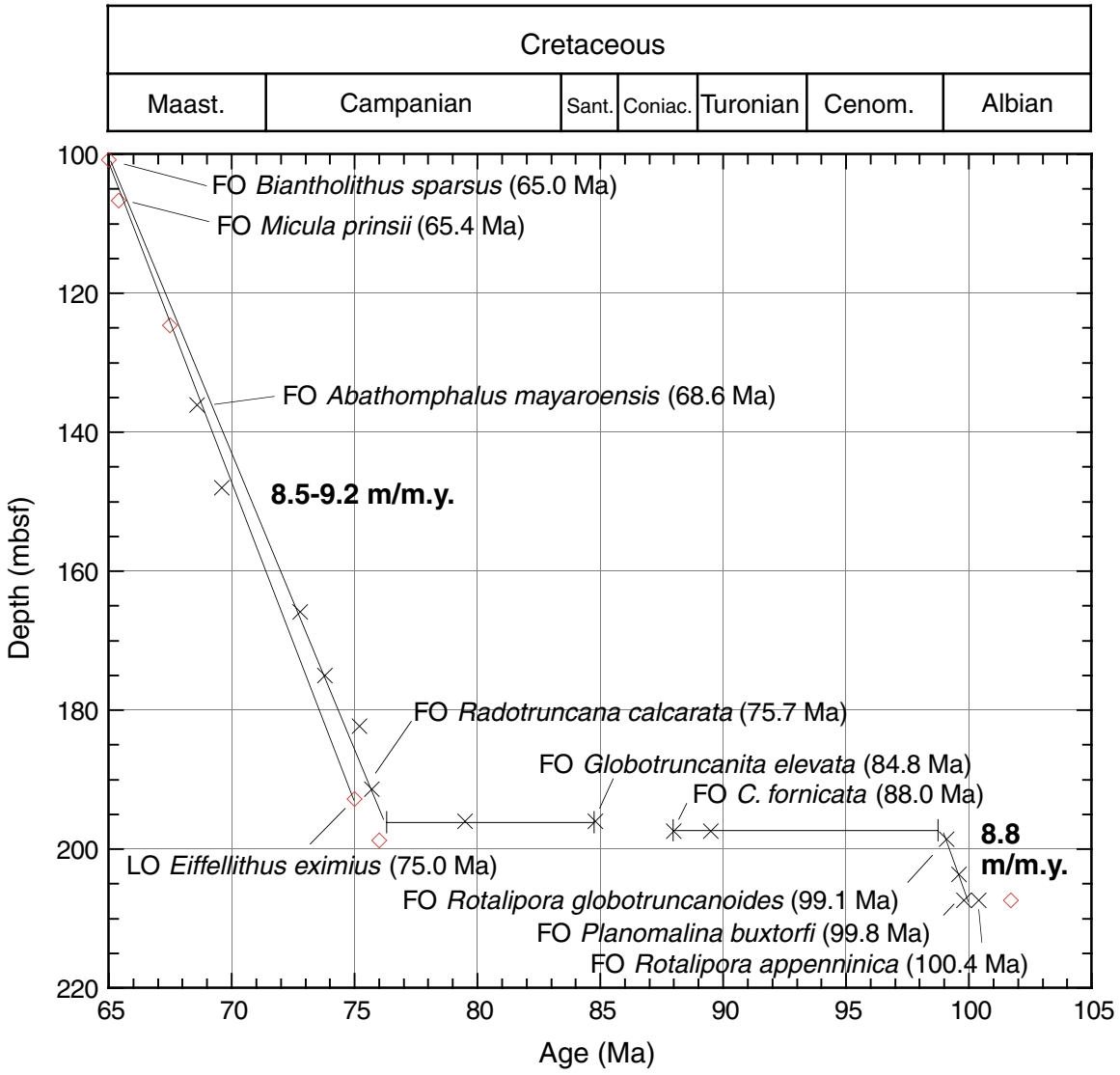

Figure F19. Mass accumulation rates for bulk sediment, carbonate fraction, and noncarbonate fraction vs. (A) depth and (B) age for the Maastrichtian–Pleistocene, Site 1212.

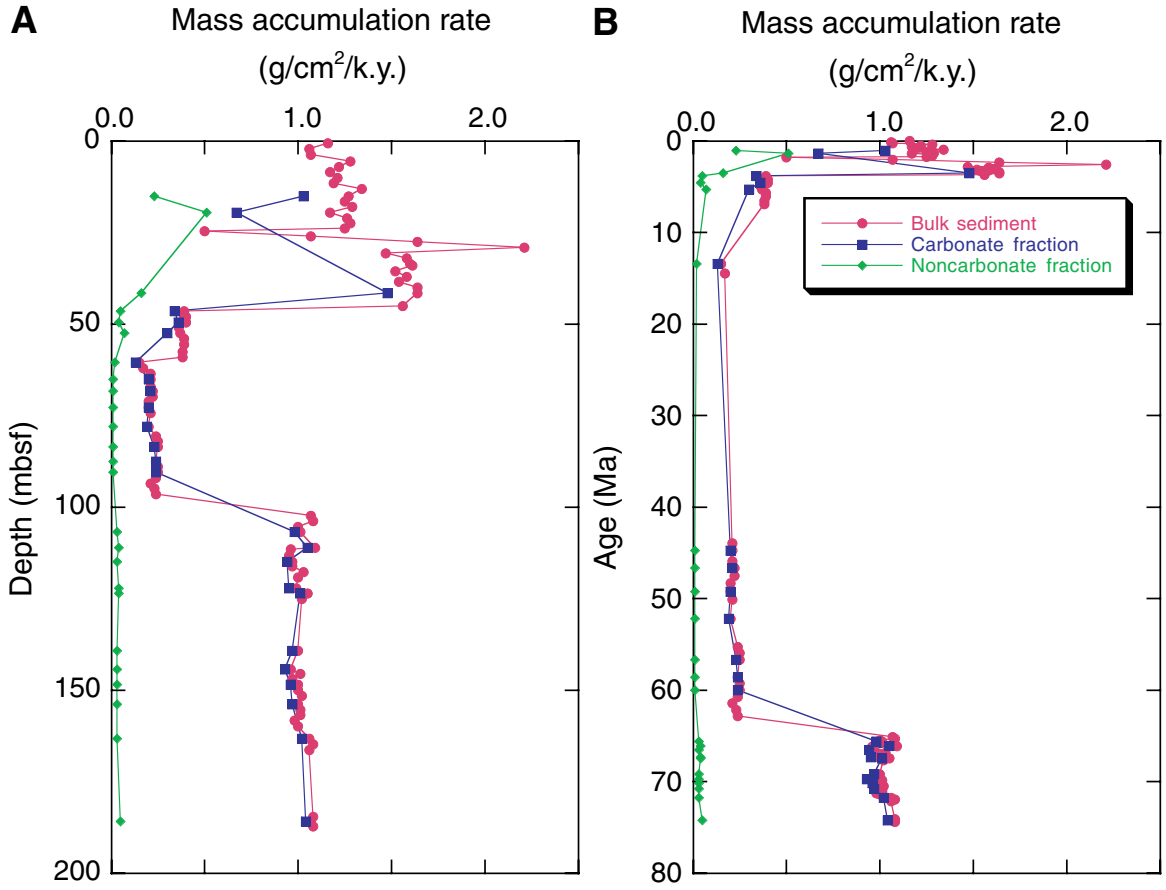

Figure F20. Downhole profiles of carbonate content for Site 1212.

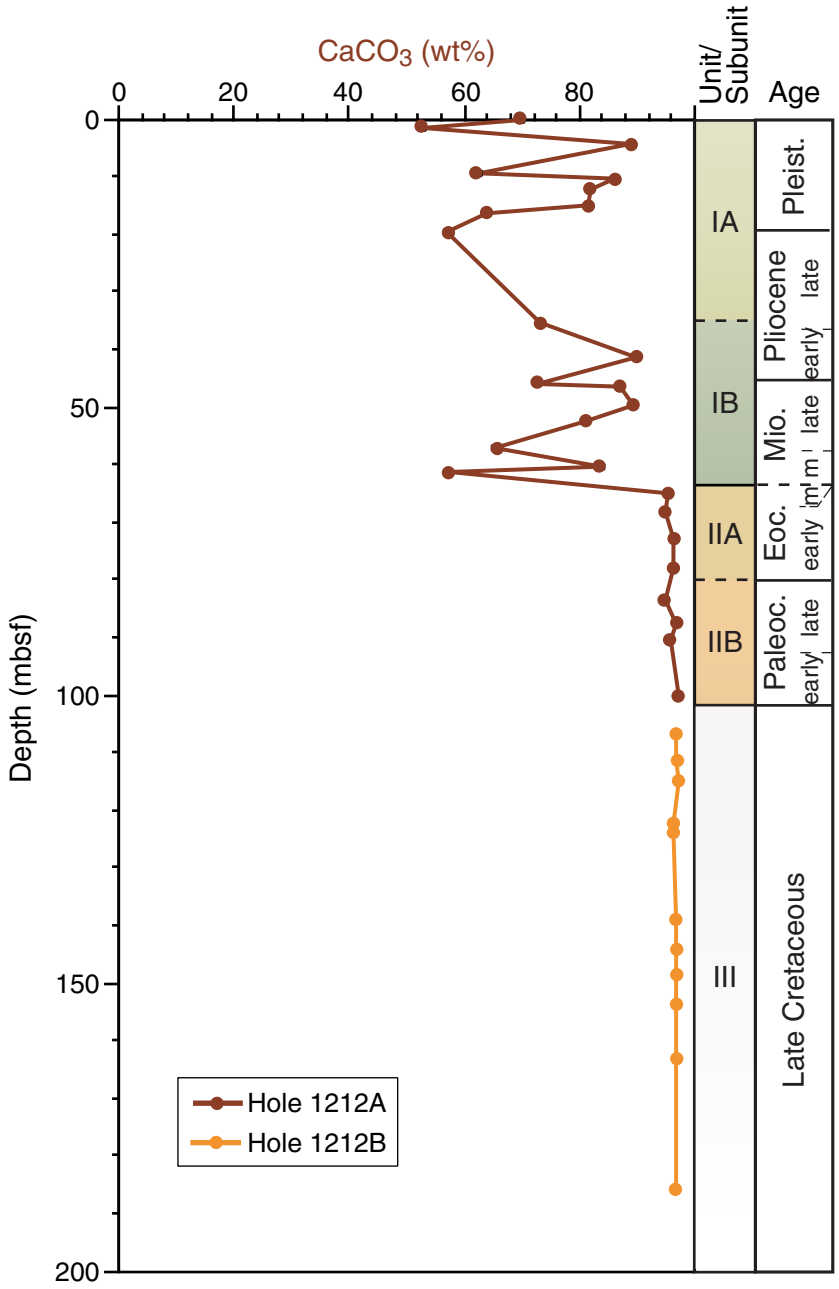

Figure F21. Downcore profiles for (**A**) chloride and (**B**) sodium, Site 1212. Sodium is calculated by charge balance. Low sample volume at 141.65 mbsf prevented measurement of the complete suite of pore water species; hence, sodium could not be calculated for this sample.

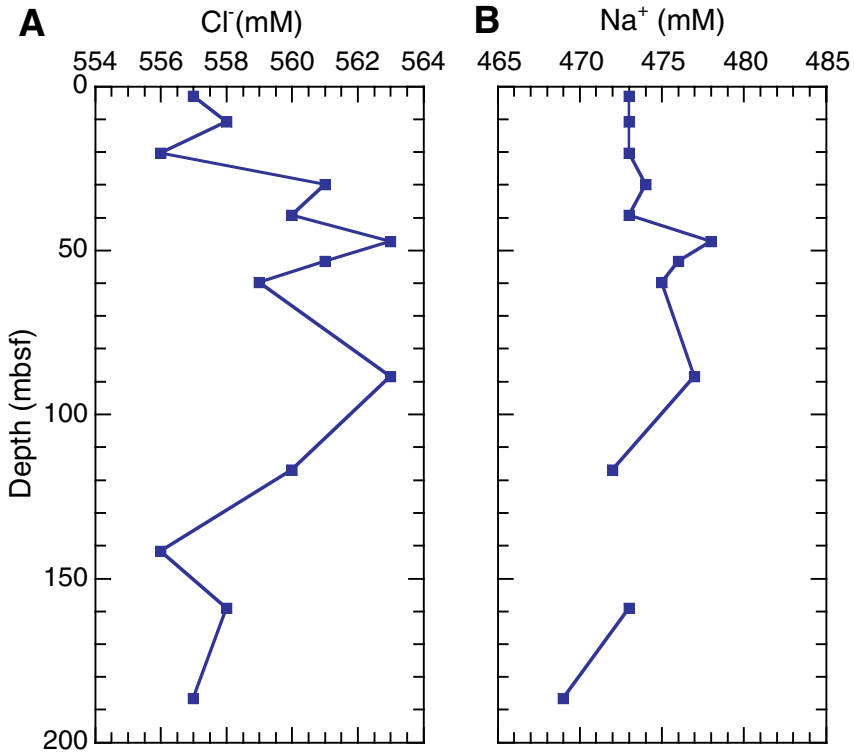

Figure F22. Site 1212 pore water profiles. **A.** Sulfate. **B.** Alkalinity. **C.** Ammonium. **D.** Phosphate. Compared with Sites 1209–1211, there is more sulfate reduction occurring at Site 1212. Low sample volume at 141.6 mbsf precluded a complete suite of analyses.

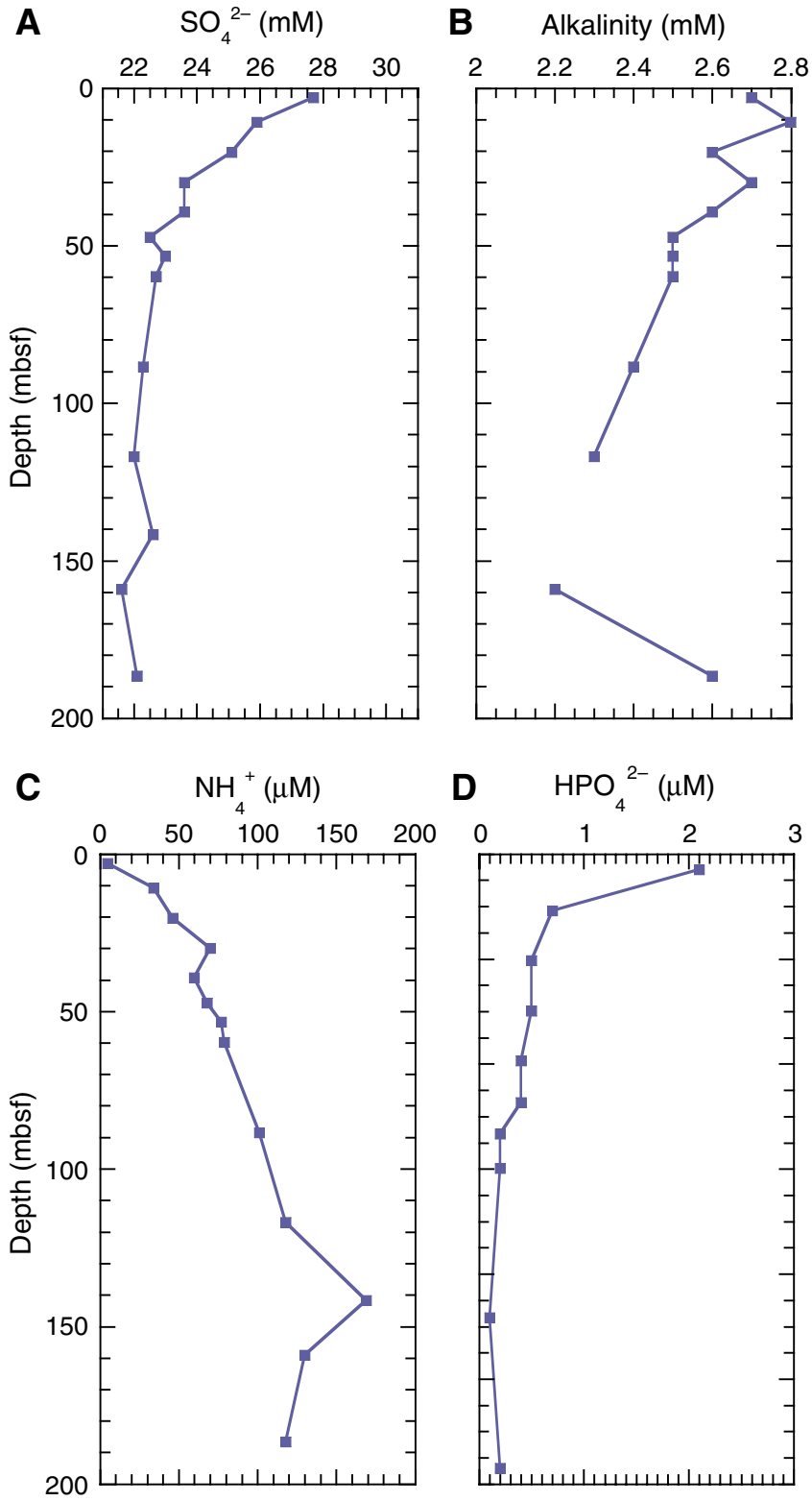

Figure F23. (A) Manganese and (B) iron concentrations at Site 1212 decrease significantly through lithologic Unit I (0.00–53.60 mbsf) and remain relatively uniform through the underlying sediment column. As at previous sites, there is an excursion in the manganese profile at the unconformity in Core 198-1212A-7H, implying the presence of Mn-rich minerals. Low sample volume at 141.6 mbsf precluded a complete suite of analyses.

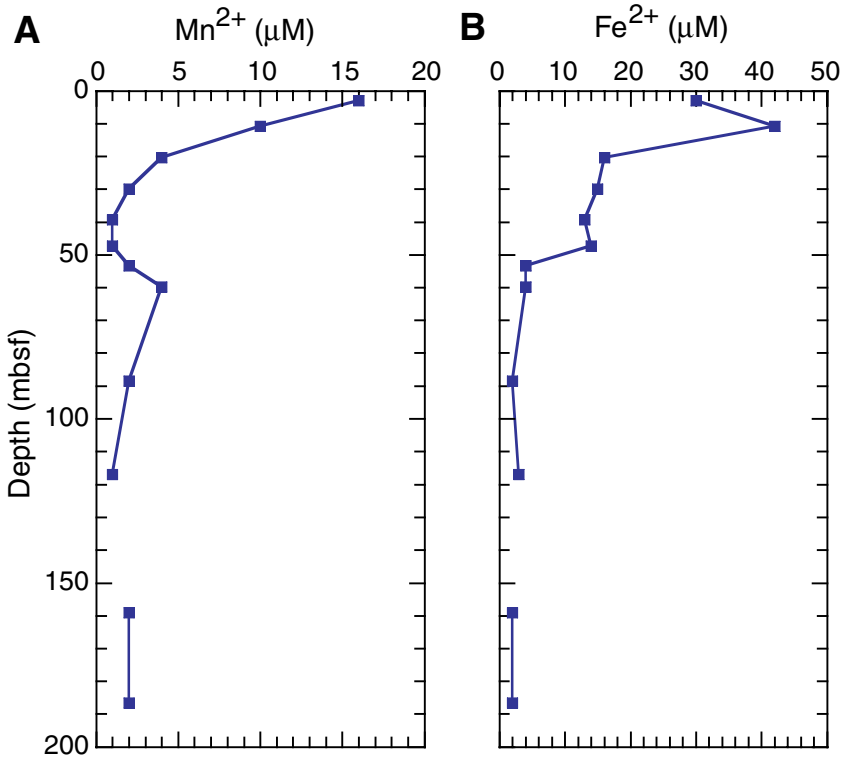

Figure F24. Interstitial water profiles for Site 1212. **A.** Potassium. **B.** Calcium. **C.** Magnesium. **D.** Sr/Ca ratios. **E.** Strontium. **F.** Lithium. It is likely that the potassium, magnesium, and calcium concentrations are being influenced by basement reactions, although other processes appear to be controlling downcore magnesium concentrations as well (see **"Potassium, Calcium, Magnesium, Strontium, and Lithium,"** p. 22, in "Inorganic Geochemistry"). Little carbonate dissolution or recrystallization appears to be occurring below ~50 mbsf. Low sample volume at 141.6 mbsf precluded a complete suite of analyses.

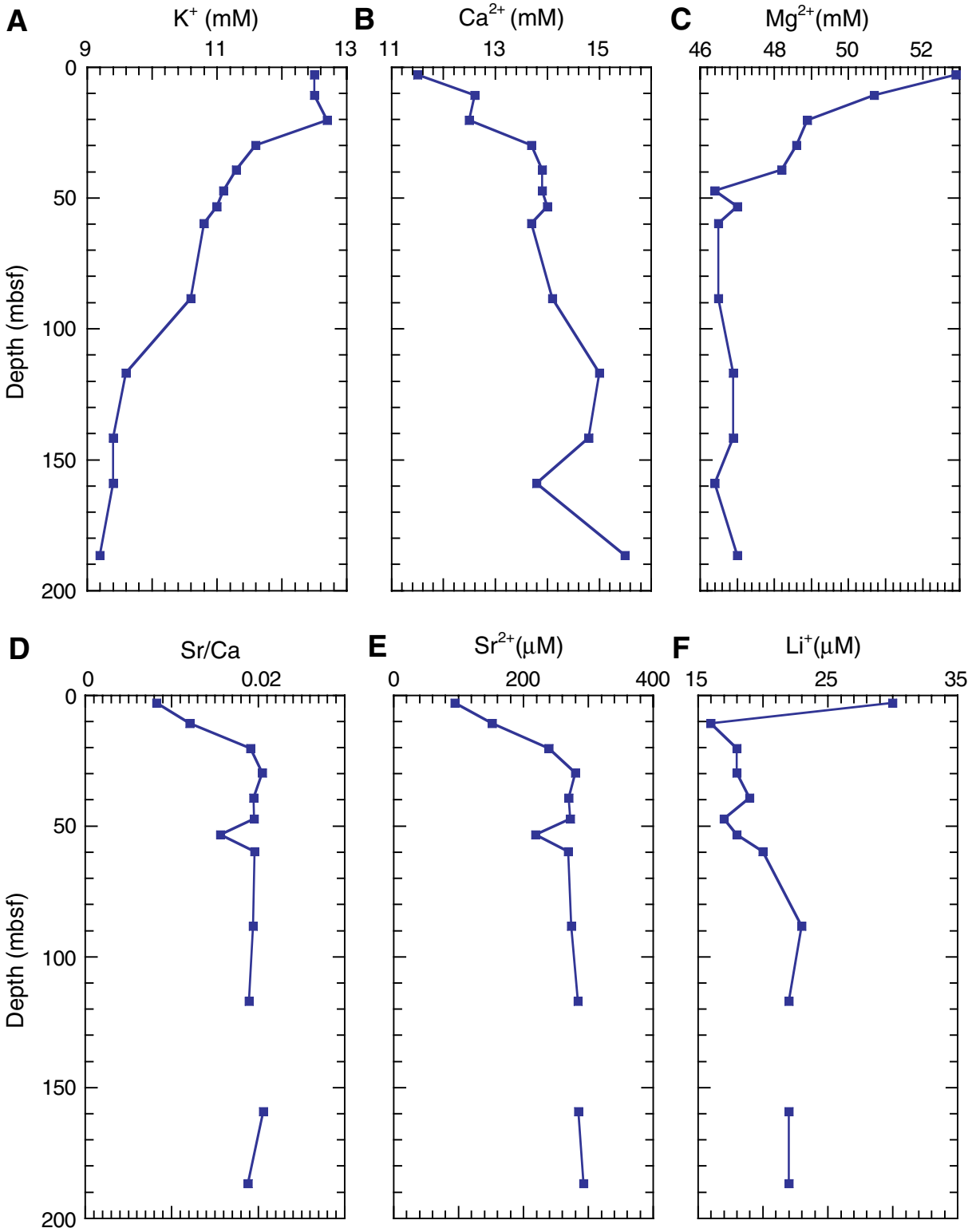

Figure F25. Downcore silica concentrations at Site 1212.

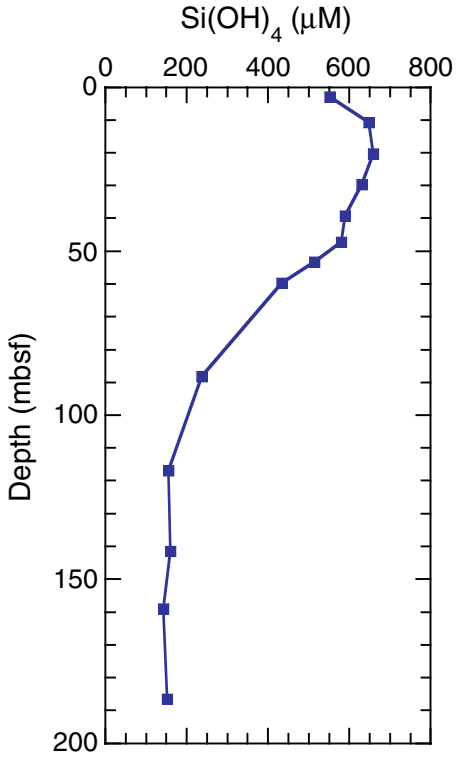

Figure F26. MST magnetic susceptibility measured in whole cores from Holes 1212A and 1212B plotted vs. depth. The accurate correction factor for the raw instrument values is 0.68×10^{-5}.

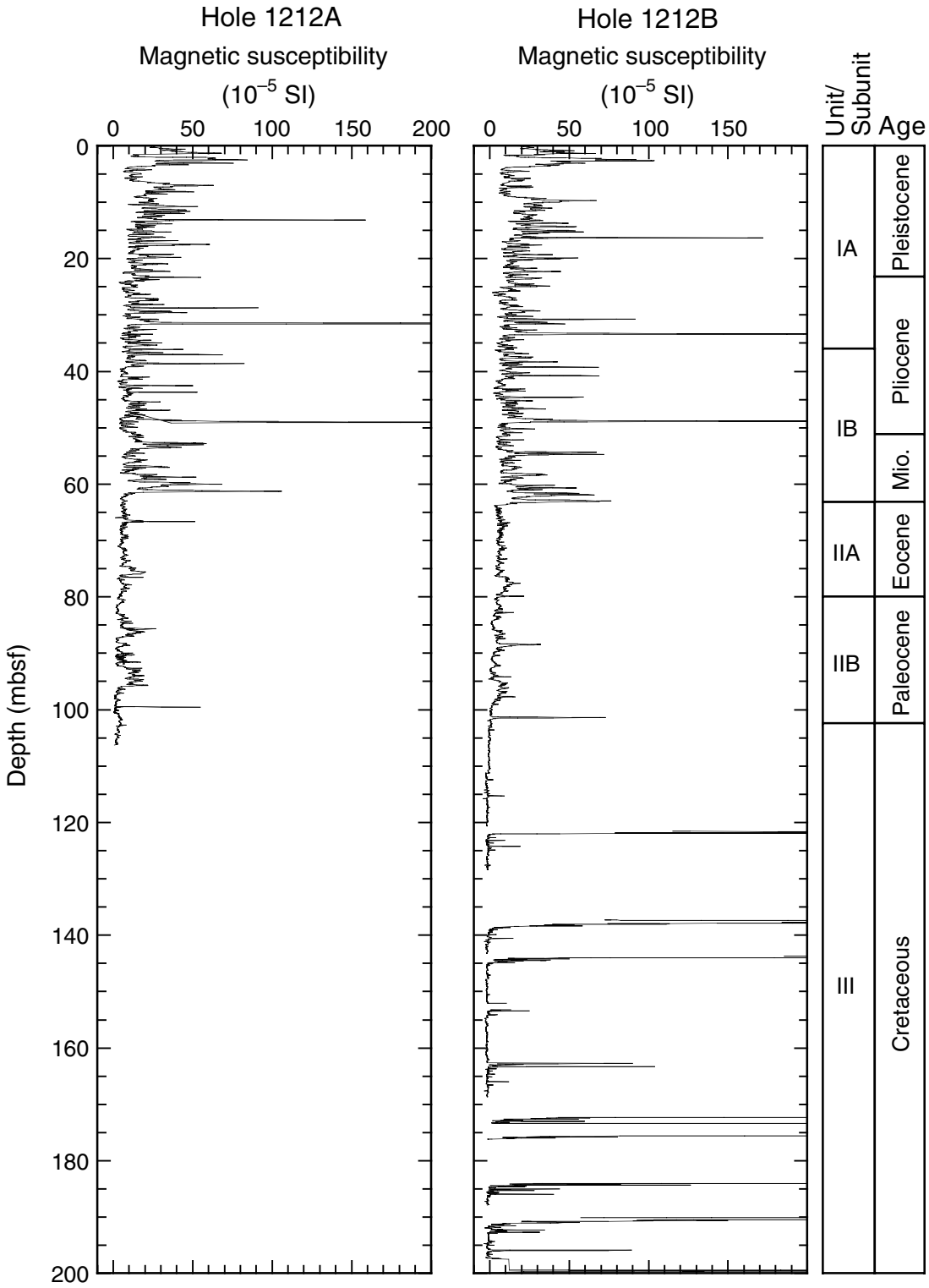

Figure F27. MST gamma ray attenuation (GRA) bulk density (lines) measured in whole cores from Holes 1212A and 1212B plotted vs. depth. Discrete measurements of wet bulk density (see Table **T12,** p. 77) (solid circles) are plotted for comparison.

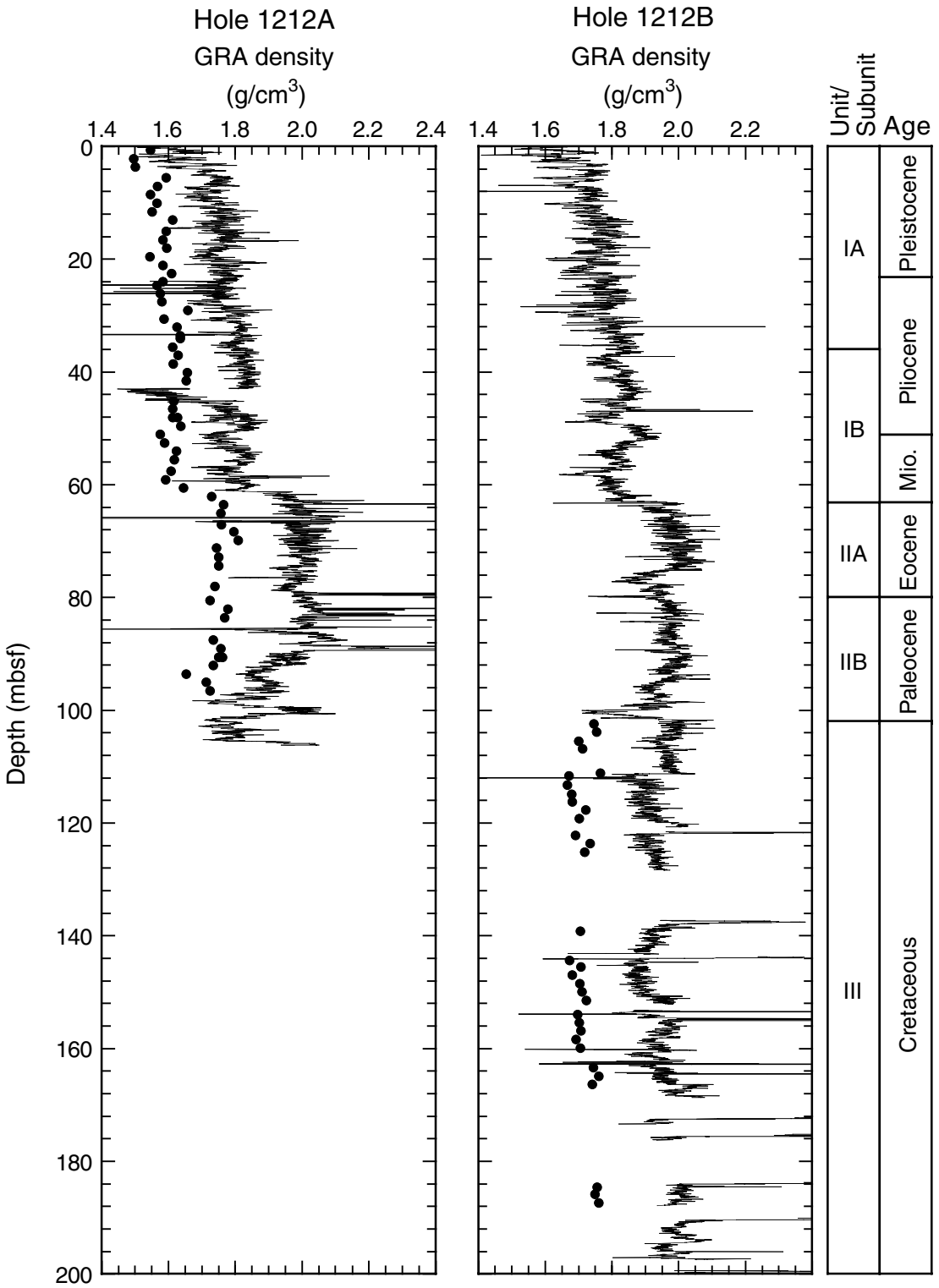

Figure F28. MST *P*-wave velocity (solid dots) measured in Holes 1212A and 1212B whole cores plotted vs. depth. For comparison, discrete *P*-wave velocity data (open circles) are also shown.

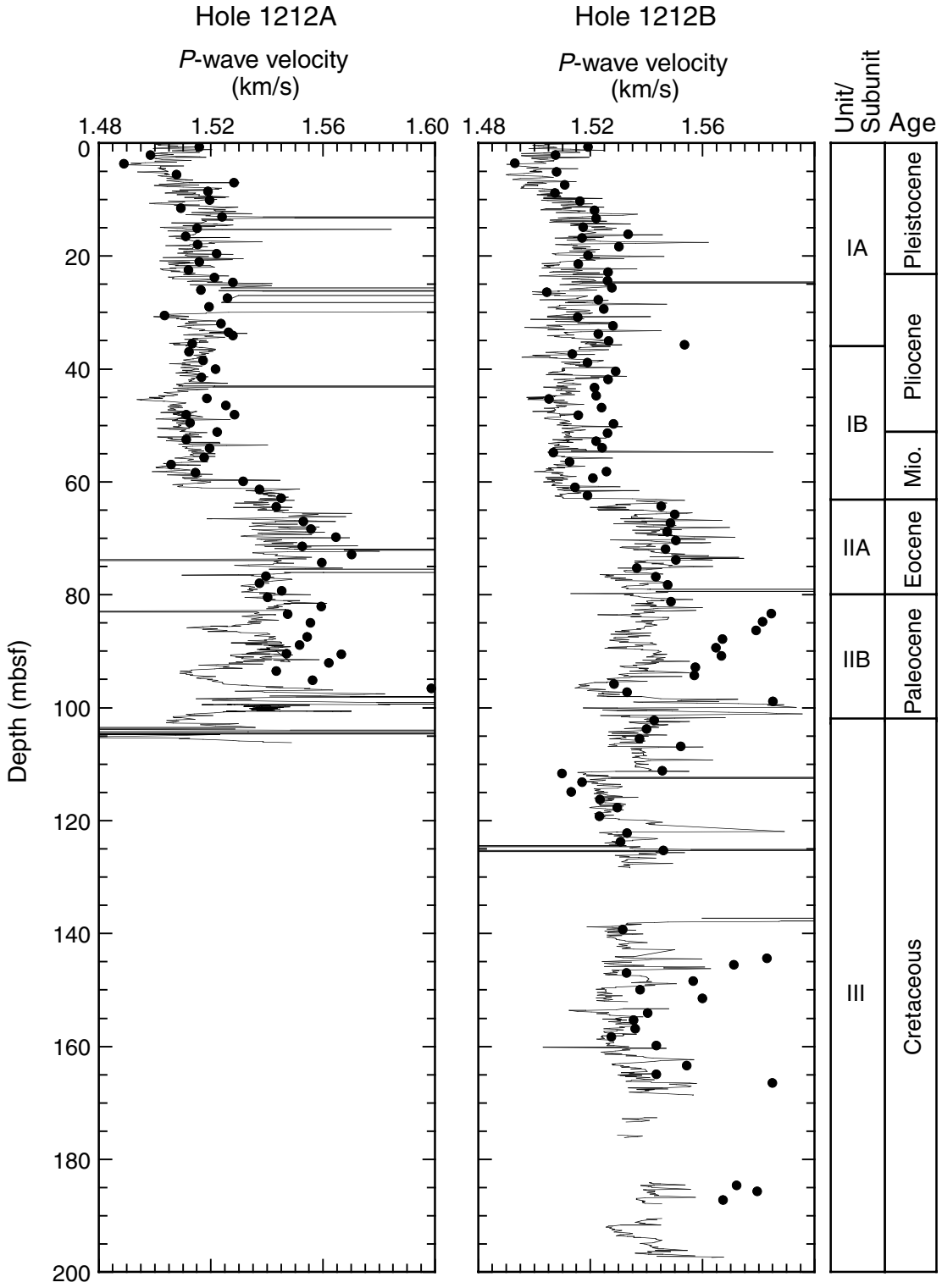

Figure F29. *P*-wave velocities for discrete samples from Holes 1212A and 1212B (see Table T13, p. 79, for data).

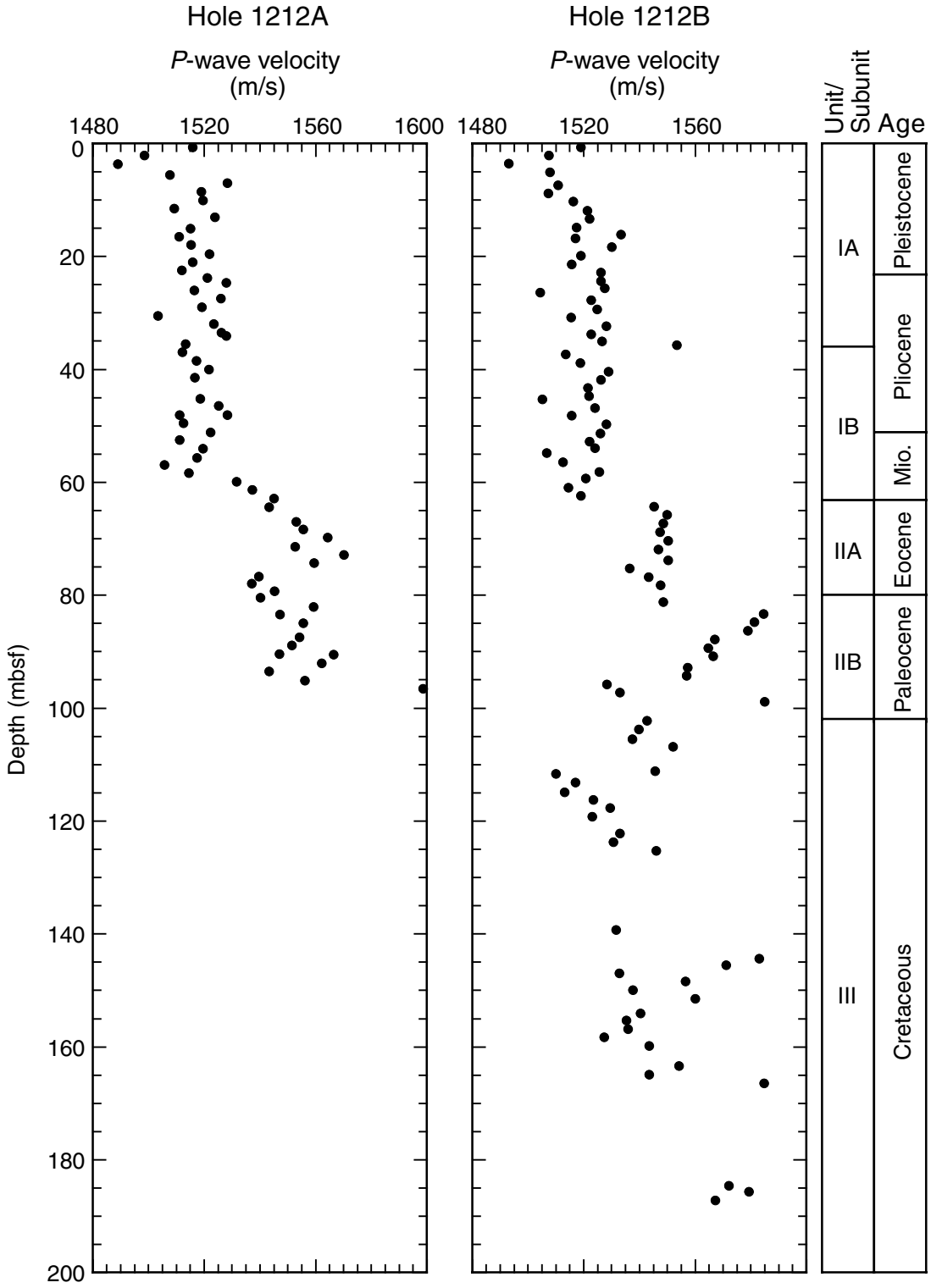

Figure F30. MST natural gamma radiation data for Hole 1212A plotted vs. depth.

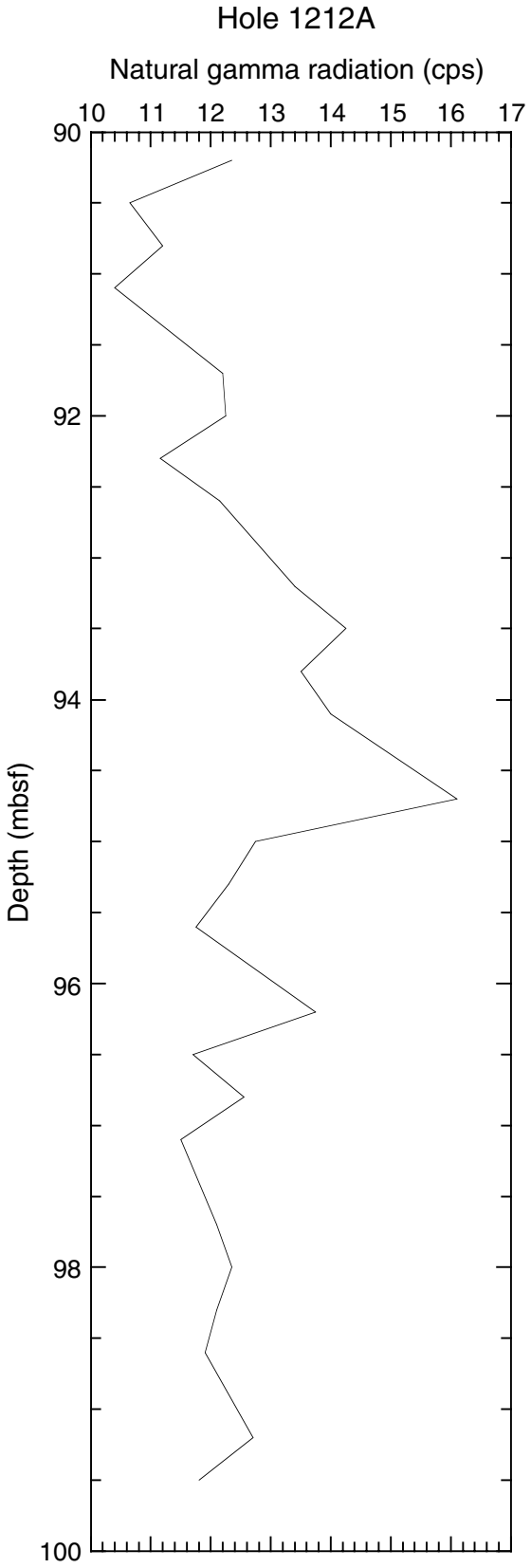

Figure F31. Discrete measurements of Hole 1212A (solid circles) and Hole 1212B (open circles) *P*-wave velocities plotted vs. discrete wet bulk density measurements at comparable stratigraphic horizons.

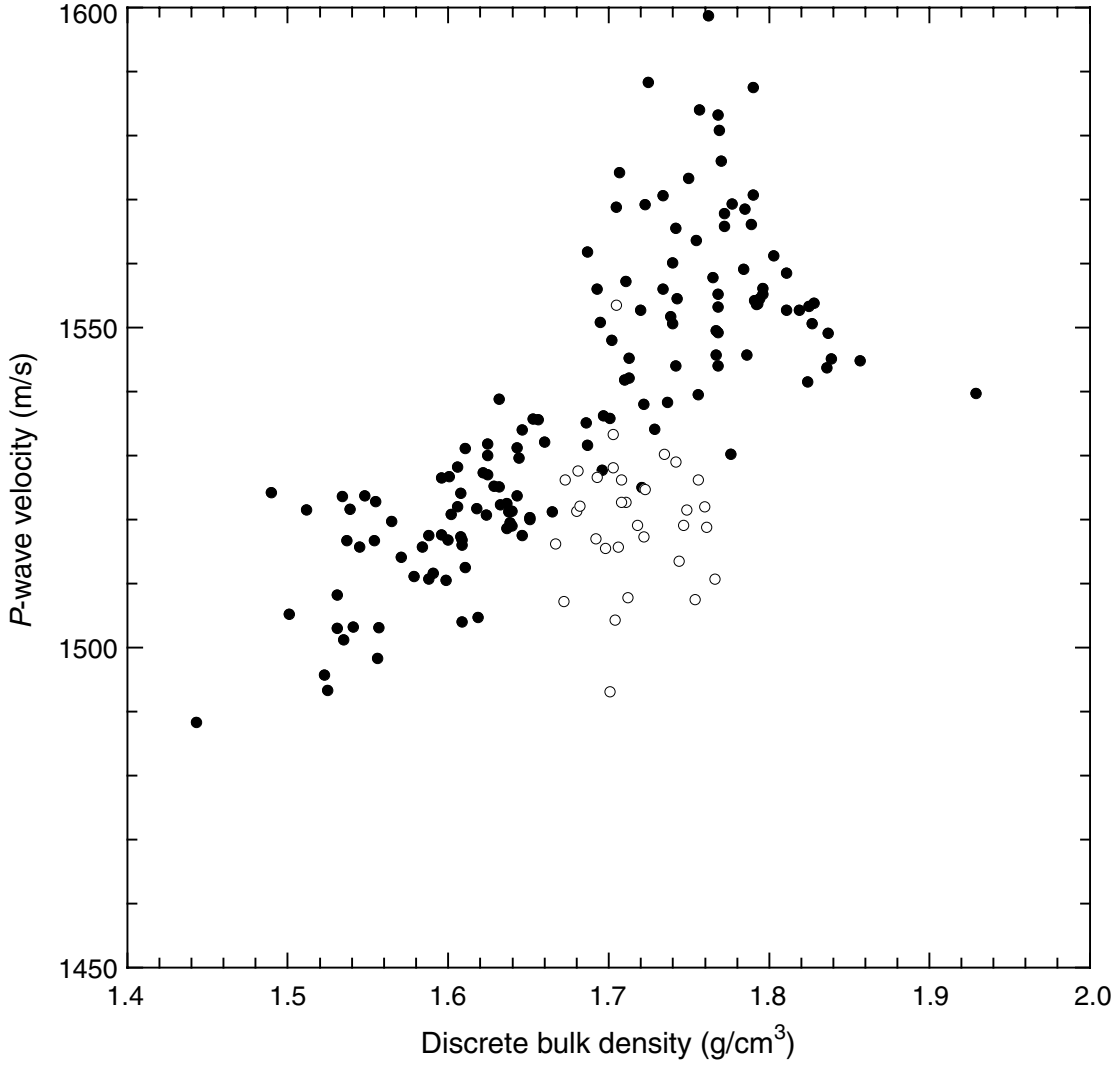

Figure F32. Water content (**A**) calculated relative to bulk sediment (circles) and solid phase (triangles), (**B**) porosity, and (**C**) void ratio determined for discrete samples from Hole 1212A (solid circles and triangles) and Hole 1212B (open circles and triangles) plotted vs. depth.

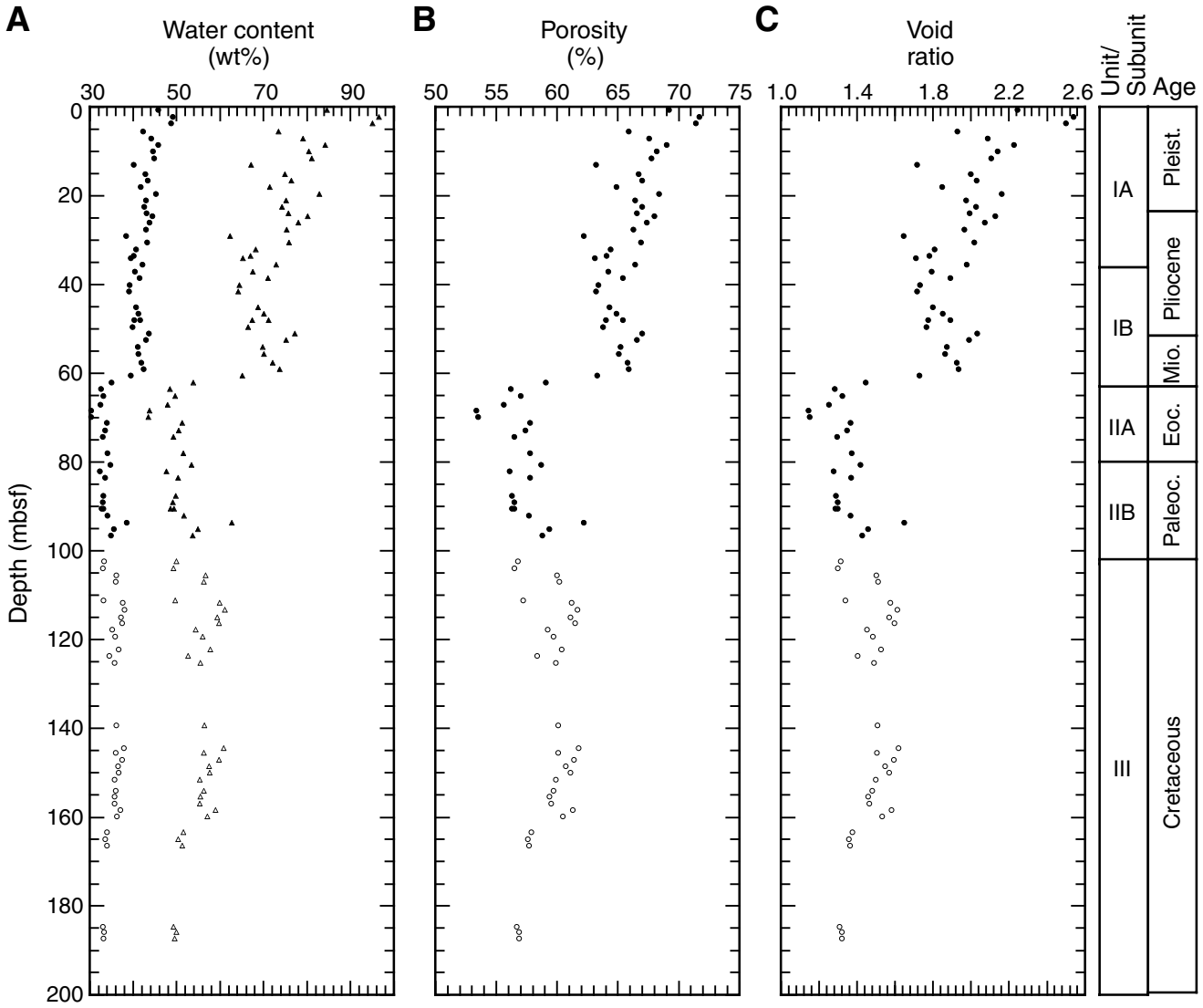

Figure F33. (A) Wet bulk density, (B) dry density, and (C) grain density determined for discrete samples from Hole 1212A (solid circles) and Hole 1212B (open circles) plotted vs. depth.

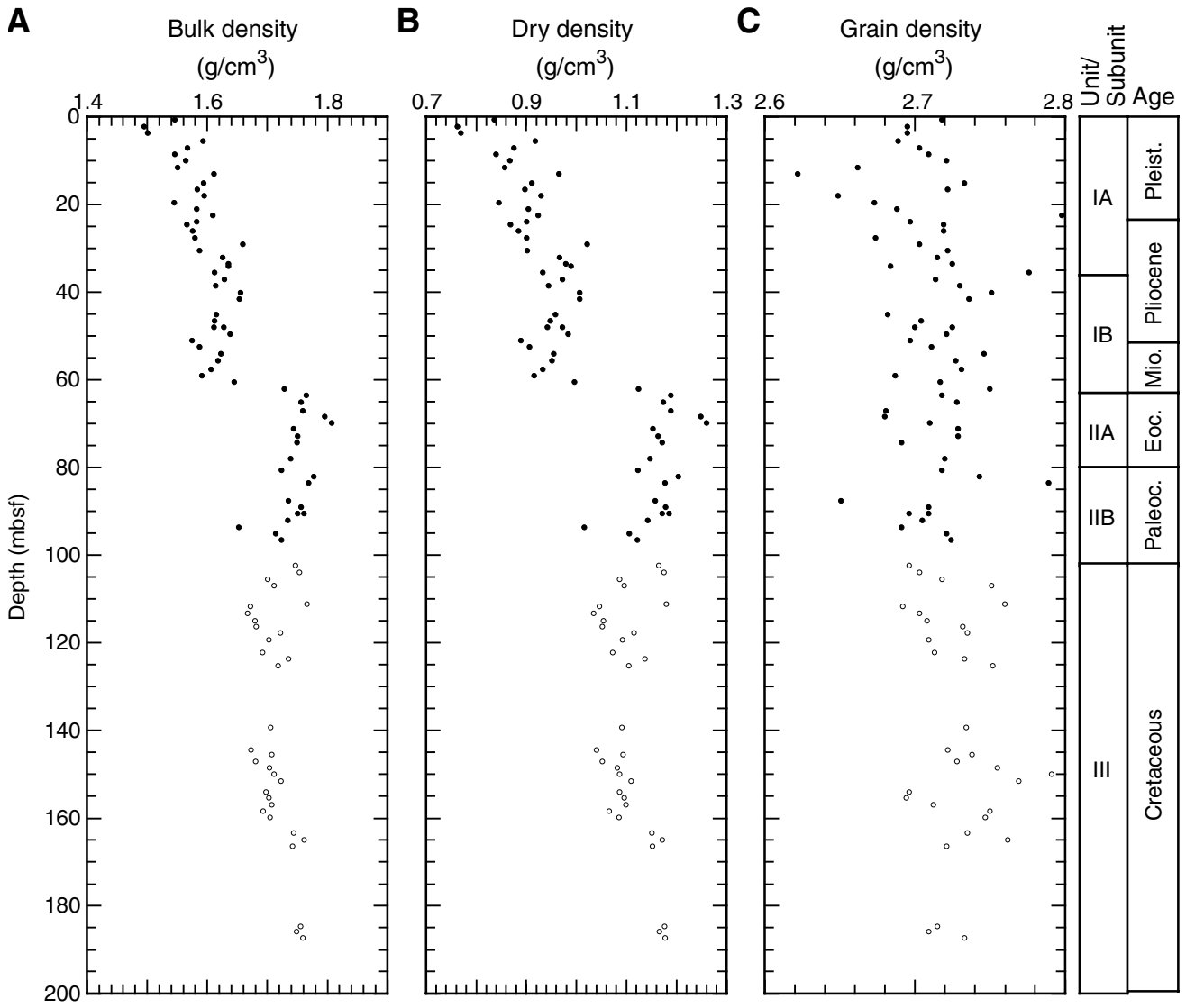

Table T1. Coring summary, Site 1212. (Continued on next page.)

Hole 1212A
Latitude: 32°26.9000′N
Longitude: 157°42.7016′E
Time on site (hr): 61.5 (1000 hr, 29 Sep–2330 hr, 1 Oct 2001)
Time on hole (hr): 29 (1000 hr, 29 Sep–1500 hr, 30 Sep 2001)
Seafloor (drill pipe measurement from rig floor, mbrf): 2693.6
Distance between rig floor and sea level (m): 11.1
Water depth (drill pipe measurement from sea level, m): 2682.5
Total depth (drill pipe measurement from rig floor, mbrf): 2795.2
Total penetration (mbsf): 101.6
Total length of cored section (m): 101.6
Total core recovered (m): 116.9
Core recovery (%): 115.1
Total number of cores: 13
Total number of drilled intervals: 0

Hole 1212B
Latitude: 32°26.9070′N
Longitude: 157°42.7002′E
Time on hole (hr): 32.5 (1500 hr, 29 Sep–2330 hr, 1 Oct 2001)
Seafloor (drill pipe measurement from rig floor, mbrf): 2691.8
Distance between rig floor and sea level (m): 11.2
Water depth (drill pipe measurement from sea level, m): 2680.6
Total depth (drill pipe measurement from rig floor, mbrf): 2899.4
Total penetration (mbsf): 207.6
Total length of cored section (m): 192.8
Total core recovered (m): 180.5
Core recovery (%): 93.6
Total number of cores: 27
Total number of drilled intervals: 10

Core	Date (2001)	Local time (hr)	Depth (mbsf) Top	Depth (mbsf) Bottom	Length (m) Cored	Length (m) Recovered	Recovery (%)
198-1212A-							
1H	29 Sep	1555	0.0	4.9	4.9	4.96	101.2
2H	29 Sep	1645	4.9	14.4	9.5	9.94	104.6
3H	29 Sep	1729	14.4	23.9	9.5	9.99	105.2
4H	29 Sep	1815	23.9	33.4	9.5	10.07	106.0
5H	29 Sep	1900	33.4	42.9	9.5	10.02	105.5
6H	29 Sep	1950	42.9	47.4	4.5	6.53	145.1
7H	29 Sep	2035	47.4	56.9	9.5	10.06	105.9
8H	29 Sep	2120	56.9	66.4	9.5	9.64	101.5
9H	29 Sep	2205	66.4	75.9	9.5	9.66	101.7
10H	29 Sep	2250	75.9	85.4	9.5	10.03	105.6
11H	29 Sep	2340	85.4	89.9	4.5	6.85	152.2
12H	30 Sep	0030	89.9	99.4	9.5	9.94	104.6
13H	30 Sep	0140	99.4	101.6	2.2	9.25	420.5
				Cored totals:	101.6	116.94	115.1
198-1212B-							
1H	30 Sep	0400	0.0	6.7	6.7	6.74	100.6
2H	30 Sep	0440	6.7	16.2	9.5	10.04	105.7
3H	30 Sep	0530	16.2	25.7	9.5	9.86	103.8
4H	30 Sep	0615	25.7	35.2	9.5	10.02	105.5
5H	30 Sep	0700	35.2	44.7	9.5	10.04	105.7
6H	30 Sep	0745	44.7	54.2	9.5	10.03	105.6
7H	30 Sep	0825	54.2	63.7	9.5	9.77	102.8
8H	30 Sep	0920	63.7	73.2	9.5	9.75	102.6
9H	30 Sep	1005	73.2	82.7	9.5	9.99	105.2
10H	30 Sep	1050	82.7	92.2	9.5	9.80	103.2
11H	30 Sep	1145	92.2	101.7	9.5	9.70	102.1
12H	30 Sep	1225	101.7	111.2	9.5	9.81	103.3
13H	30 Sep	1355	111.2	120.7	9.5	9.73	102.4
14H	30 Sep	1435	120.7	120.8	0.1	0.03	30.0
		*****Drilled from 120.8 to 121.5 mbsf*****					
15H	30 Sep	1615	121.5	131.0	9.5	7.12	74.9
16H	30 Sep	1735	131.0	135.2	4.2	0.00	0.0
		*****Drilled from 135.2 to 136.2 mbsf*****					
		*****Drilled from 136.2 to 136.4 mbsf*****					
		*****Drilled from 136.4 to 137.2 mbsf*****					

Table T1 (continued).

Core	Date (2001)	Local time (hr)	Depth (mbsf) Top	Depth (mbsf) Bottom	Length (m) Cored	Length (m) Recovered	Recovery (%)
17H	1 Oct	0150	137.2	143.7	6.5	6.43	98.9
18H	1 Oct	0245	143.7	153.2	9.5	9.11	95.9
19H	1 Oct	0415	153.2	162.7	9.5	9.64	101.5
20H	1 Oct	0630	162.7	172.2	9.5	6.33	66.6
21H	1 Oct	0730	172.2	173.2	1.0	1.38	138.0
		*****Drilled from 173.2 to 175.2 mbsf*****					
22H	1 Oct	0905	175.2	182.7	7.5	1.38	18.4
		*****Drilled from 182.7 to 183.7 mbsf*****					
23H	1 Oct	1025	183.7	189.0	5.3	4.41	83.2
		*****Drilled from 189.0 to 190.0 mbsf*****					
24H	1 Oct	1200	190.0	196.3	6.3	7.66	121.6
		*****Drilled from 196.3 to 199.3 mbsf*****					
25H	1 Oct	1350	199.3	201.0	1.7	0.63	37.1
		*****Drilled from 201.0 to 203.5 mbsf*****					
26H	1 Oct	1525	203.5	204.5	1.0	0.80	80.0
		*****Drilled from 204.5 to 207.1 mbsf*****					
27H	1 Oct	1655	207.1	207.6	0.5	0.30	60.0
				Cored totals:	192.8	180.50	93.6
				Drilled total:	14.8		
				Total:	207.6		

Table T2. Calcareous nannofossil datums, ages, and depths, Site 1212.

Datum	Zone/ Subzone (base)	Core, section, interval (cm)	Depth (mbsf)	Core, section, interval (cm)	Depth (mbsf)	Age (Ma)
		198-1212A-		198-1212B-		
LO *Pseudoemiliania lacunosa*	CN14b	1H-CC	4.91	1H-CC	6.69	0.46
LO *Discoaster brouweri*	CN13	3H-CC	24.34	2H-CC	16.69	1.95
LO *Discoaster pentaradiatus*	CN12d			3H-CC	26.01	2.52
LO *Reticulofenestra pseudoumbilicus*	CN12a	5H-CC	43.37	5H-CC	45.19	3.82
FO *Ceratolithus rugosus*	CN10c	6H-CC	49.38			5.1
LO *Triquetrorhabdulus rugosus*	CN10b			6H-CC	54.68	5.23
FO *Discoaster berggrenii*	CN9	8H-3, 5 cm	59.95	7H-6, 10	61.80	8.2
LO *Sphenolithus heteromorphus*	CN5	8H-3, 50 cm	60.4			13.523
FO *Sphenolithus heteromorphus*	CN3	8H-3, 130 cm	61.2	7H-6, 120	62.90	18.2
FO *Discoaster sublodoensis*	CP12	8H-CC	66.49	7H-CC	63.92	49.7
FO *Discoaster diastypus*	CP9a	9H-7, 30	75.52			55.0
FO *Discoaster multiradiatus*	CP8	10H-1, 140	77.3	9H-CC	83.14	56.2
FO *Heliolithus riedelii*	CP5	10H-CC	85.88			58.4
FO *Ellipsolithus macellus*	CP3	11H-CC	92.2	10H-CC	92.45	62.2
FO *Chiasmolithus danicus*	CP2	12H-5, 140	97.3			63.8
FO *Chiasmolithus tenuis*	CP1b			11H-4, 70	97.4	64.5
LO Cretaceous taxa	CP1a	12H-7, 60	99.5	11H-6, 70	100.4	65.0
FO *Micula prinsii*	CC26	13H-CC	106.33	11H-CC	101.85	65.4
LO *Reinhardtites levis*	CC25			17H-CC	143.42	69.2
LO *Eiffellithus eximius*	CC23			23H-CC	188.01	75.0
FO *Uniplanarius trifidum*	CC22			~24H-6	~197	76.0
FO *Marthasterites furcatus*	CC13			24H-6, 30	197.3	89.3
FO *Eiffellithus turriseiffelii*	NC10a			27H-CC	207.35	101.7

Note: FO = first occurrence, LO = last occurrence.

Table T3. Planktonic foraminiferal datums, ages, and depths, Site 1212.

Datum	Zone/ Subzone (base)	Core, section, interval (cm)	Depth (mbsf)	Core, section, interval (cm)	Depth (mbsf)	Age (Ma)
		198-1212A-		198-1212B-		
LO *Globigerinoides obliquus*		1H-CC	4.91			1.3
FO *Truncorotalia truncatulinoides*	N22	4H-CC	33.92	3H-CC	26.01	1.92
LO *Globigerinoides extremus*		3H-CC	24.34	3H-CC	26.01	1.98
FO *Truncorotalia tosaensis*	N21	5H-CC	43.37	3H-CC	26.01	3.35
LO *Dentoglobigerina altispira*		5H-CC	43.37	5H-CC	45.19	3.11
LO *Sphaeroidinellopsis seminulina*		6H-CC	49.38	5H-CC	45.19	3.11
LO *Globorotalia margaritae*		4H-CC	33.92	5H-CC	45.19	3.85
FO *Truncorotalia crassaformis*		5H-CC	43.37	5H-CC	45.19	4.31
LO *Globoturborotalita nepenthes*		7H-CC	57.36			4.39
FO *Globorotalia tumida*	N18	5H-CC	43.37	5H-CC	45.19	5.82
FO *Globorotalia margaritae*		7H-CC	57.36	5H-CC	45.19	6.09
LO *Paragloborotalia mayeri*	N15					10.49
FO *Globoturborotalita nepenthes*	N14	7H-CC	57.36			11.19
FO *Orbulina universa*	N9	7H-CC	57.36	7H-6, 118–120	62.88	15.1
FO *Praeorbulina sicana*	N8					16.4
FO *Globoquadrina dehiscens*	M1b			7H-6, 118–120	62.88	23.2
LO *Subbotina angiporoides*						30.0
LO *Pseudohastigerina* spp.	P19					32.0
LO *Hantkenina* spp.						33.7
LO *Globigerinatheka index*						34.3
LO *Acarinina primitiva*		8H-CC	66.49			39.0
LO *"Orbulinoides" beckmanni*	P14					40.1
FO *"Orbulinoides" beckmanni*	P13					40.5
LO *Acarinina bullbrooki*		8H-CC	66.49			40.5
FO *Turborotalia pomeroli*						
LO *Morozovella aragonensis*	P12	8H-CC	66.49	7H-6, 135–137	63.05	43.6
FO *Globigerinatheka kugleri*	P11					45.8
FO *Hantkenina* spp.	P10					49.0
LO *Morozovella formosa*	P8					50.8
FO *Acarinina pentacamerata*		8H-CC	66.49	7H-CC	63.92	50.8
FO *Morozovella aragonensis*	P7	8H-CC	66.49	7H-CC	63.92	52.3
LO *Morozovella aequa*						53.6
FO *Morozovella formosa*	P6b					54.0
LO *Morozovella velascoensis*	P6a	10H-CC	85.88	9H-5, 42–43	79.62	54.7
FO *Morozovella gracilis*		9H-CC	75.78			54.7
FO *Morozovella subbotinae*		9H-CC	75.78			55.9
LO *Globanomalina pseudomenardii*	P5			9H-5, 72–73	79.93	55.9
LO *Acarinina mckannai*				9H-CC	83.14	56.3
FO *Acarinina mckannai*				9H-CC	83.14	59.1
FO *Globanomalina pseudomenardii*	P4a					59.2
FO *Morozovella velascoensis*		8H-CC	66.49	9H-CC	83.14	60.0
FO *Morozovella conicotruncata*		12H-CC	99.79	10H-CC	92.45	60.9
FO *Morozovella angulata*		12H-CC	99.79	10H-CC	92.45	61.0
FO *Igorina pusilla*						61.0
FO *Praemurica uncinata*	P2					61.2
FO *Praemurica inconstans*		12H-CC	99.79			63.0
LO *Parvularugoglobigerina eugubina*	P1a	12H-7, 58–59	99.48			64.7
FO *Parvularugoglobigerina eugubina*	P1α	12H-7, 72–73	99.62	11H-7, 23–24	101.43	64.97
LO *Abathomphalus mayaroensis*		12H-CC, 6–7	99.71	11H-CC	101.85	65.0
FO *Abathomphalus mayaroensis*	KS31			15H-CC	128.57	68.6
FO *Racemiguembelina fructicosa*						69.6
FO *Contusotruncana contusa*				17H-CC	143.42	69.6
FO *Globotruncanita atlantica*	KS26			24H-4, 26–28	194.76	79.5
FO *Contusotruncana fornicata*				24H-6, 32–33	197.32	88.0
FO *Dicarinella concavata*	KS23			24H-6, 32–33	197.32	89.5
FO *Rotalipora globotruncanoides*	KS17			24H-6, 44–46	197.44	99.1
FO *Costellagerina libyca*				25H-1, 42–44	199.72	99.6
FO *Planomalina buxtorfi*				27H-1, 25–30	207.35	99.8
FO *Rotalipora appenninica*	KS 16			27H-1, 25–30	207.35	100.4

Note: FO = first occurrence, LO = last occurrence.

Table T4. Distribution of Cenozoic and Cretaceous benthic foraminifers, Hole 1212A. (Continued on next page.)

Core, section	Depth (mbsf)	Nannofossil zone/ subzone	Size fraction (µm)	Preservation	Benthic abundance	Trocospiral forms																		Other forms														Buliminids							
						Oridorsalis umbonatus	*Nuttallides truempyi*	*Osangularia velascoensis*	*Gavelinella beccariiformis*	*Gyroidinoides globosus*	*Gyroidinoides* spp.	*Conorbinoides hillebrandti*	*Quadrimorphina profunda*	*Clinapertina complanata*	*Oridorsalis tener*	*Anomalinoides globulosus*	*Pullenia quinqueloba*	*Pullenia bulloides*	*Cibicidoides mundulus*	*Cibicidoides wuellerstorfi*	*Gyroidinoides girardanus*	*Cibicidoides bradyi*	*Cibicidoides incrassatus*	*Cibicidoides subhaidingeri*	*Aragonia velascoensis*	*Lenticulina* spp.	*Aragonia ouezzanensis*	*Dentalina* spp.	*Nodosaria* spp.	*Neoflabellina semireticulata*	*Pleurostomella* spp.	*Pyrgo murrhina*	*Chrysalogonium longicostatum*	*Quadrimorphina* spp.	*Pyrgo lucernula*	*Sphaeroidina bulloides*	*Bulimina velascoensis*	*Buliminella grata*	*Quadratobuliminella pyramidalis*	*Bulimina trinitatensis*	*Bulimina jarvisi*	*Bulimina impendens*	*Bulimina striata*
198-1212A-																																												
1H-CC	4.91	CN14b	>250	VG	F										R			F	F	T		R	R	T								R			R								R
3H-CC	24.34	CN13	>250	G	F										C			F		F	T							T			R		R									
5H-CC	43.37	CN12a	>250	G	F										R			R		C											R	T	R									
6H-CC	49.38	CN10c	>250	G	F										T			R	R	A											F											
7H-CC	57.36	CN9c	>250	G	A										R	R	R	R										R		R	F											
8H-CC	66.49	CP12	>125	M	T–R		R							R	T													R								A	T			
9H-CC	75.78	u.CP8	>125	M	T	R	A						R												T			T	R	T	T						T				
10H-CC	85.88	CP5	>125	M	C	F	F				R	R														R	T	R	R	T											
11H-CC	92.20	CP3	>125	M	R	F	R			R		R														T	T	R	T								T	R			
12H-CC	99.79	CP2	>125	M	A	C	R	R	T	R	R														C	T	T	T							R	T				
13H-CC	106.33	CC26	>125	G	F	F	R	T																	T	T	T	T												

Notes: Preservation: VG = very good, G = good, M = moderate. Abundance: A = abundant, C = common, F = few, R = rare, T = trace.

Table T4 (continued).

Core, section	Depth (mbsf)	Nannofossil zone/ subzone	Size fraction (µm)	Preservation	Benthic abundance	Stilostomellids				Uvigerinids				Agglutinated									
						Stilostomella spp.	*Stilostomella subspinosa*	*Stilostomella abyssorum*	*Stilostomella gracillima*	*Uvigerina hispidocostata*	*Uvigerina hispida*	*Uvigerina spinicostata*	*Uvigerina peregrina*	*Tritaxia globulifera*	*Tritaxia rugolosa*	*Tritaxia* spp.	*Gaudryina pyramidata*	*Spiroplectammina spectabilis*	*Spiroplectammina jarvisi*	*Marssonella trochoides*	*Karreriella bradyi*	*Martinottiella* sp.	*Eggerella bradyi*
1H-CC	4.91	CN14b	>250	VG	F					T	R		T										
3H-CC	24.34	CN13	>250	G	F					R	R	T											R
5H-CC	43.37	CN12a	>250	G	F					T												R	
6H-CC	49.38	CN10c	>250	G	F			F	R												T	R	
7H-CC	57.36	CN9c	>250	G	A		C	A	F												F	F	
8H-CC	66.49	CP12	>125	M	T–R																		
9H-CC	75.78	u.CP8	>125	M	T																		
10H-CC	85.88	CP5	>125	M	C	R										C			T	R			
11H-CC	92.20	CP3	>125	M	R	R									C	F			R				
12H-CC	99.79	CP2	>125	M	A									R		C	R	T	R				
13H-CC	106.33	CC26	>125	G	F									R	R	R	R		T				

Table T5. Distribution of Cenozoic and Cretaceous benthic foraminifers, Hole 1212B. (Continued on next page.)

						Trochospiral															Other forms																	
Core, section	Depth (mbsf)	Nannofossil zone/ subzone	Size fraction (µm)	Preservation	Benthic abundance	*Gyroidinoides infracretaceus*	*Protosangularia albiana*	*Conorotalites aptiensis*	*Gavelinella* spp.	*Hanzawaia compressa*	*Gyroidinoides globosus*	*Protosangularia cenomaniana*	*Osangularia mexicana*	*Anomalinoides* spp.	*Nuttallides truempyi*	*Gyroidinoides* spp.	*Oridorsalis umbonatus*	*Conorbinoides hillebrandti*	*Sliterella lobulata*	*Nuttallinella florealis*	*Ramulina tetrahedralis*	*Saracenaria* spp.	*Astacolus* spp.	*Marginulina inaequalis*	*Tristix excavata*	*Pleurostomella* spp.	*Ramulina tappanae*	*Dentalina* spp.	*Lenticulina* spp.	*Nodosaria* spp.	*Aragonia velascoensis*	*Bulimina* spp.	*Quadrimorphina allomorphinoides*	*Aragonia ouezzanensis*	*Buliminella grata*	*Pyramidina szajnochae*	*Bulimina velascoensis*	*Quadratobuliminella pyramidalis*
10H-CC	92.45	u.CP3	>125	G	F										T		C			R								T	T					R	T		R	R
12H-CC	111.46	CC25c	>125	G	F						R				R	T	C			T								R	R	R				F		F		
13H-CC	120.88	CC25c	>125	G	F						R					R	F			R								F	R		C			R	T			
15H-CC	128.57	CC25	>125	M	R										T	T	C			T								F	R					R		R		
18H-CC	152.34	CC23	>125	M	R									R	F	R	R											R	R	T	F	T	T					
20H-CC	168.98	CC23	>125	M	F						R				F		F		C	T							T		R	T		T			T			
21H-CC	173.53	CC23	>125	M	R										C	R	R	R		T						T		R	R	T		R	T	C				
23H-CC	188.01	CC23	>125	M	R						T			R	R		R	F	T	F						T		R	T			T		R	T			
24H-CC	197.61	CC14-16	>125	G	F			A	R	A	R		C	R	T	R	R									R		R	R	T	T							
25H-CC	199.90	NC10a	>125	G	A		C			A	R	R											T	T	R	F		R	R									
27H-1	207.35	NC10a	>125	G	C	R	C	R	T	A	F										T	T	T	T	T	C	T	F	R	R								

Notes: Preservation: G = good, M = moderate. Abundance: A = abundant, C = common, F = few, R = rare, T = trace.

Table T5 (continued).

Core, section	Depth (mbsf)	Nannofossil zone/ subzone	Size fraction (µm)	Preservation	Benthic abundance	Agglutinated																
						Praedorothia praehauteriviana	*Pseudoclavulina* sp.	*Spiroplectinella excolata*	*Dorothia gradata*	*Marssonella oxycona*	*Rhizammina* spp.	*Tritaxia globulifera*	*Spiroplectammina* sp.	*Tritaxia* spp.	*Spiroplectammina jarvisi*	*Gaudryina pyramidata*	*Marssonella trochoides*	*Tritaxia rugolosa*	*Spiroplectammina spectabilis*
10H-CC	92.45	u.CP3	>125	G	F							R		F				T	
12H-CC	111.46	CC25c	>125	G	F							R		R		F	R	R	
13H-CC	120.88	CC25c	>125	G	F										T	R			
15H-CC	128.57	CC25	>125	M	R							T		R	R		R		
18H-CC	152.34	CC23	>125	M	R										T	R	R		T
20H-CC	168.98	CC23	>125	M	F									R	T	C	F	R	
21H-CC	173.53	CC23	>125	M	R									R			T		
23H-CC	188.01	CC23	>125	M	R							T			T	T	T		
24H-CC	197.61	CC14-16	>125	G	F				R	R	T	R	R	R					
25H-CC	199.90	NC10a	>125	G	A			R	R	R	T	F	R	R					
27H-CC	207.35	NC10a	>125	G	C	R	R	R	F	R	T	R							

Table T6. Composite depth section, Site 1212.

Core	Depth (mbsf)	Offset (m)	Depth (mcd)
198-1212A-			
1H	0.0	0.15	0.15
2H	4.9	3.15	8.05
3H	14.4	3.49	17.89
4H	23.9	3.49	27.39
5H	33.4	3.79	37.19
6H	42.9	3.79	46.69
7H	47.4	7.27	54.67
8H	56.9	7.85	64.75
9H	66.4	9.45	75.85
10H	75.9	11.05	86.95
11H	85.4	11.67	97.07
12H	89.9	9.57	99.47
13H	99.4	9.57	108.97
198-1212B-			
1H	0.0	0.00	0.00
2H	6.7	0.00	6.70
3H	16.2	1.03	17.23
4H	25.7	1.60	27.30
5H	35.2	1.60	36.80
6H	44.7	4.03	48.73
7H	54.2	6.02	60.22
8H	63.7	7.44	71.14
9H	73.2	7.69	80.89
10H	82.7	8.28	90.98
11H	92.2	7.78	99.98
12H	101.7	7.78	109.48
13H	111.2	7.78	118.98
14H	120.7	7.78	128.48
15H	121.5	7.78	129.28
16H	131.0	7.78	138.78
17H	137.2	7.78	144.98
18H	143.7	7.78	151.48
19H	153.2	7.78	160.98
20H	162.7	7.78	170.48
21H	172.2	7.78	179.98
22H	175.2	7.78	182.98
23H	183.7	7.78	191.48
24H	190.0	7.78	197.78
25H	199.3	7.78	207.08
26H	203.5	7.78	211.28
27H	207.1	7.78	214.88

Table T7. Splice tie points, Site 1212.

Core, section, interval (cm)	Depth (mbsf)	Depth (mcd)		Core, section, interval (cm)	Depth (mbsf)	Depth (mcd)
198-				198-		
1212B-1H-5, 42	6.42	6.42	Append	1212B-2-H-1, 0	6.70	6.70
1212B-2-H-7, 60	16.30	16.30	Tie to	1212A-2-H-6, 75	13.15	16.30
1212A-2-H-7, 36	14.26	17.41	Tie to	1212B-3-H-1, 18	16.38	17.41
1212B-3-H-6, 117	24.87	25.90	Tie to	1212A-3-H-6, 51	22.41	25.90
1212A-3-H-7, 57	23.97	27.46	Tie to	1212A-4-H-1, 6	23.97	27.46
1212A-4-H-7, 51	33.41	36.90	Tie to	1212B-5-H-1, 9	35.30	36.90
1212B-5-H-7, 57	44.77	46.37	Tie to	1212A-5-H-7, 18	42.58	46.37
1212A-5-H-7, 60	43.00	46.79	Tie to	1212A-6-H-1, 9	43.00	46.79
1212A-6-H-5, 72	49.12	52.91	Tie to	1212B-6-H-3, 117	48.88	52.91
1212B-6-H-6, 108	53.28	57.31	Tie to	1212A-7-H-2, 114	50.04	57.31
1212A-7-H-7, 57	56.97	64.24	Tie to	1212B-7-H-3, 102	58.22	64.24
1212B-7-H-7, 9	63.29	69.31	Tie to	1212A-8-H-4, 6	61.46	69.31
1212A-8-H-7, 24	66.14	73.99	Tie to	1212B-8-H-2, 135	66.55	73.99
1212B-8-H-7, 48	73.18	80.62	Tie to	1212A-9-H-4, 45	71.17	80.62
1212A-9-H-7, 39	75.61	85.06	Tie to	1212B-9-H-3, 117	77.37	85.06
1212B-9-H-5, 75	79.95	87.64	Tie to	1212A-10-H-1, 69	76.59	87.64
1212A-10-H-7, 129	85.69	96.74	Tie to	1212B-10-H-4, 126	88.46	96.74
1212B-10-H-7, 48	92.18	100.46	Tie to	1212B-11-H-1, 48	92.68	100.46
1212B-11-H-7, 48	101.68	109.46	Append	1212B-12-H-1, 0	101.70	109.48
1212B-12-H-7, 60	111.30	119.08	Tie to	1212B-13-H-1, 9	111.30	119.08
1212B-13-H-7, 63	120.71	128.49				

Table T8. Linear sedimentation rate segments used to calculate mass accumulation rates, as well as average accumulation rates for bulk sediment, carbonate, and noncarbonate fractions.

	Depth (mbsf)		Age (Ma)			Average accumulation rate (g/cm²/k.y.)		
Segment	Top	Bottom	Top	Bottom	Age	Bulk sediment	Carbonate	Noncarbonate
1	0.00	24.10	0.00	1.73	Pleistocene	1.2	0.9	0.4
2	24.10	30.40	1.73	2.83	late Pliocene	1.4	NA	NA
3	30.40	46.50	2.83	3.82	early Pliocene–late Pliocene	1.6	1.5	0.2
4	46.50	58.70	3.82	6.76	late Miocene–early Pliocene	0.4	0.3	0.1
5	60.70	63.00	13.52	15.10	middle Miocene	0.2	0.1	0.0
6	63.00	79.40	43.60	54.70	early Eocene–middle Eocene	0.2	0.2	0.0
7	79.40	100.80	54.70	65.00	Paleocene	0.2	0.2	0.0
8	100.80	192.80	65.00	75.00	Campanian–Maastrichtian	1.0	1.0	0.0

Note: NA = no data available.

Table T9. Concentrations of CH_4 in headspace gas, Hole 1212A.

Core, section, interval (cm)	Depth (mbsf)	CH_4 (ppmv)
198-1212A-		
1H-3, 0–5	3.0	1.9
2H-5, 0–5	10.9	1.8
3H-5, 0–5	20.4	2.0
4H-5, 0–5	29.9	2.1
5H-5, 0–5	39.4	2.1
6H-4, 0–5	47.4	1.8
7H-5, 0–5	53.4	2.0
8H-3, 0–5	59.9	1.8
11H-3, 0–5	88.4	2.0

Table T10. Carbonate content, Site 1212.

Core, section, interval (cm)	Depth (mbsf)	Total inorganic carbon (wt%)	$CaCO_3$ (wt%)
198-1212A-			
1H-1, 4–5	0.04	8.4	70.0
1H-1, 140–141	1.40	6.4	52.9
1H-4, 48–49	4.48	10.7	88.9
2H-4, 28–29	9.68	7.5	62.5
2H-4, 102–103	10.42	10.3	86.0
2H-5, 123–124	12.13	9.8	81.7
3H-1, 54–55	14.94	9.8	81.6
3H-2, 35–36	16.25	7.7	64.1
3H-4, 67–68	19.57	6.8	57.0
5H-2, 38–39	35.28	8.8	73.1
5H-6, 74–75	41.64	10.8	90.0
6H-3, 16–17	46.06	8.7	72.7
6H-3, 66–67	46.56	10.4	87.0
7H-2, 70–71	49.60	10.7	89.4
7H-4, 70–71	52.60	9.7	81.0
7H-7, 56–57	56.96	7.9	65.4
8H-3, 71–72	60.61	10.1	83.8
8H-3, 144–145	61.34	6.9	57.3
8H-6, 70–71	65.10	11.4	95.3
9H-2, 70–71	68.42	11.4	95.0
9H-5, 70–71	72.92	11.6	96.5
10H-2, 73–74	78.13	11.5	96.1
10H-6, 73–74	83.63	11.4	95.0
11H-2, 71–72	87.61	11.6	96.6
11H-4, 71–72	90.61	11.5	95.8
13H-1, 91–92	100.31	11.7	97.1
198-1212B-			
12H-4, 74–75	106.94	11.6	96.7
13H-1, 8–9	111.28	11.6	96.7
13H-3, 89–90	114.97	11.7	97.4
15H-1, 73–74	122.23	11.5	96.1
15H-2, 73–74	123.73	11.6	96.4
17H-2, 72–73	139.26	11.6	96.5
18H-1, 71–72	144.41	11.6	96.7
18H-4, 72–73	148.55	11.6	96.9
19H-1, 78–79	153.98	11.6	96.6
20H-1, 72–73	163.42	11.6	96.7
23H-2, 70–71	185.85	11.6	96.5

Table T11. Geochemical data collected, Site 1212.

Core, section, interval (cm)	Depth (mbsf)	pH	Alkalinity (mM)	Salinity	Cl^- (mM)	SO_4^{2-} (mM)	Na^+ (mM)	Mg^{2+} (mM)	Ca^{2+} (mM)	K^+ (mM)	H_4SiO_4 (µM)	NH_4^+ (µM)	HPO_4^{2-} (µM)	Sr^{2+} (µM)	Fe^{2+} (µM)	Mn^{2+} (µM)	Li^+ (µM)	Ba^{2+} (µM)	B_3OH_3 (µM)
198-1212A-																			
1H-2, 145–150	2.95	7.63	2.7	35.0	557	27.7	473	52.9	11.5	12.5	552	5	2.1	95	30	16	30	0.2	381
2H-4, 145–150	10.85	7.51	2.8	35.0	558	25.9	473	50.7	12.6	12.5	648	34	0.7	152	42	10	16	0.2	375
3H-4, 145–150	20.35	7.45	2.6	35.0	556	25.1	473	48.9	12.5	12.7	660	46	0.5	239	16	4	18	0.3	374
4H-4, 145–150	29.85	7.39	2.7	34.5	561	23.6	474	48.6	13.7	11.6	631	70	0.5	280	15	2	18	0.2	396
5H-4, 145–150	39.35	7.37	2.6	34.5	560	23.6	473	48.2	13.9	11.3	590	60	0.4	270	13	1	19	0.2	373
6H-3, 145–150	47.35	7.40	2.5	34.5	563	22.5	478	46.4	13.9	11.1	581	68	0.4	272	14	1	17	0.4	388
7H-4, 145–150	53.35	7.42	2.5	34.5	561	23.0	476	47.0	14.0	11.0	515	77	0.2	219	4	2	18	0.3	336
8H-2, 145–150	59.85	7.40	2.5	34.5	559	22.7	475	46.5	13.7	10.8	434	79	0.2	269	4	4	20	0.4	392
11H-2, 145–150	88.35	7.46	2.4	34.0	563	22.3	477	46.5	14.1	10.6	237	101	0.1	274	2	2	23	0.3	424
198-1212B-																			
13H-4, 145–150	117.03	7.44	2.3	34.0	560	22.0	472	46.9	15.0	9.6	156	118	0.2	284	3	1	22	0.6	366
17H-3, 145–150	141.49	ND	ND	34.5	556	22.6	ND	46.9	14.8	9.4	160	169	ND	ND	ND	ND	ND	ND	ND
19H-4, 140–150	159.10	7.43	2.2	34.5	558	21.6	471	46.4	14.7	9.4	144	130	ND	285	2	2	22	0.2	366
23H-2, 140–150	186.55	7.51	2.6	34.5	557	22.1	469	47.0	15.5	9.2	154	118	ND	293	2	2	22	0.2	367

Note: ND = not detected.

Table T12. Discrete index properties measurements, Site 1212.(Continued on next page.)

Core, section, interval (cm)	Depth (mbsf)	Water content (wt%)		Density (g/cm^3)			Porosity (%)	Void ratio
		Bulk mass	Dry mass	Bulk	Dry	Grain		
198-1212A-								
1H-1, 70–72	0.70	45.8	84.6	1.55	0.84	2.72	69.2	2.25
1H-2, 70–72	2.20	49.1	96.5	1.50	0.76	2.70	71.7	2.54
1H-3, 70–72	3.70	48.7	95.1	1.50	0.77	2.70	71.4	2.50
2H-1, 70–72	5.60	42.3	73.4	1.59	0.92	2.69	65.9	1.93
2H-2, 70–72	7.10	44.2	79.1	1.57	0.88	2.70	67.6	2.09
2H-3, 70–72	8.60	45.7	84.2	1.55	0.84	2.71	69.0	2.23
2H-4, 70–72	10.10	44.6	80.5	1.57	0.87	2.72	68.2	2.14
2H-5, 70–72	11.60	44.8	81.1	1.55	0.86	2.66	67.8	2.11
2H-6, 70–72	13.10	40.1	67.1	1.61	0.97	2.62	63.2	1.72
3H-1, 70–72	15.10	42.8	74.9	1.59	0.91	2.73	66.7	2.00
3H-2, 70–72	16.60	43.3	76.4	1.58	0.90	2.72	67.0	2.03
3H-3, 70–72	18.10	41.7	71.4	1.60	0.93	2.65	64.9	1.85
3H-4, 70–72	19.60	45.3	82.9	1.55	0.85	2.67	68.4	2.16
3H-5, 70–72	21.10	42.9	75.2	1.58	0.90	2.69	66.4	1.97
3H-6, 70–72	22.60	42.6	74.2	1.61	0.92	2.80	67.0	2.03
3H-7, 64–66	24.04	43.1	75.7	1.58	0.90	2.70	66.6	1.99
4H-1, 76–78	24.66	44.5	80.2	1.57	0.87	2.72	68.0	2.13
4H-2, 70–72	26.10	43.8	78.0	1.58	0.89	2.72	67.4	2.07
4H-3, 70–72	27.60	43.0	75.3	1.58	0.90	2.67	66.3	1.97
4H-4, 70–72	29.10	38.4	62.3	1.66	1.02	2.70	62.2	1.65
4H-5, 70–72	30.60	43.2	75.9	1.59	0.90	2.72	66.9	2.02
4H-6, 70–72	32.10	40.6	68.2	1.63	0.97	2.72	64.4	1.81
4H-7, 70–72	33.60	40.1	67.0	1.64	0.98	2.73	64.1	1.78
5H-1, 70–72	34.10	39.5	65.3	1.64	0.99	2.68	63.1	1.71
5H-2, 70–72	35.60	42.2	72.9	1.61	0.93	2.78	66.4	1.98
5H-3, 70–72	37.10	40.4	67.6	1.63	0.97	2.71	64.2	1.79
5H-4, 70–72	38.60	41.5	71.0	1.61	0.94	2.73	65.4	1.89
5H-5, 70–72	40.10	39.2	64.5	1.66	1.01	2.75	63.4	1.73
5H-6, 70–72	41.60	39.1	64.2	1.65	1.01	2.74	63.2	1.72
6H-2, 80–82	45.20	40.7	68.7	1.62	0.96	2.68	64.3	1.80
6H-3, 70–72	46.60	41.2	70.1	1.61	0.95	2.70	64.9	1.85
6H-4, 70–72	48.10	41.6	71.1	1.61	0.94	2.73	65.4	1.89
7H-1, 70–72	48.10	40.3	67.4	1.63	0.97	2.70	64.0	1.78
7H-2, 70–72	49.60	39.9	66.4	1.64	0.98	2.72	63.8	1.77
7H-3, 70–72	51.10	43.6	77.2	1.58	0.89	2.70	67.0	2.03
7H-4, 70–72	52.60	42.9	75.2	1.59	0.91	2.71	66.6	1.99
7H-5, 70–72	54.10	41.1	69.9	1.62	0.96	2.75	65.2	1.87
7H-6, 70–72	55.60	41.2	70.1	1.62	0.95	2.73	65.1	1.87
8H-1, 70–72	57.60	41.9	72.2	1.61	0.93	2.73	65.8	1.93
8H-2, 71–73	59.11	42.4	73.7	1.59	0.92	2.69	65.9	1.93
8H-3, 70–72	60.60	39.4	65.1	1.65	1.00	2.72	63.3	1.73
8H-4, 70–72	62.10	35.0	53.9	1.73	1.12	2.75	59.1	1.45
8H-5, 70–72	63.60	32.6	48.4	1.77	1.19	2.72	56.2	1.29
8H-6, 70–72	65.10	33.2	49.7	1.76	1.17	2.73	57.0	1.32
9H-1, 70–72	67.10	32.4	47.9	1.76	1.19	2.68	55.6	1.25
9H-2, 70–72	68.42	30.4	43.7	1.80	1.25	2.68	53.4	1.15
9H-3, 70–72	69.92	30.3	43.5	1.81	1.26	2.71	53.5	1.15
9H-4, 50–52	71.22	33.9	51.3	1.74	1.15	2.73	57.8	1.37
9H-5, 70–72	72.92	33.6	50.5	1.75	1.16	2.73	57.4	1.35
9H-6, 70–72	74.42	33.0	49.3	1.75	1.17	2.69	56.5	1.30
10H-2, 70–72	78.10	34.1	51.6	1.74	1.15	2.72	57.8	1.37
10H-4, 70–72	80.60	34.8	53.5	1.72	1.12	2.72	58.7	1.42
10H-5, 70–72	82.10	32.3	47.7	1.78	1.20	2.74	56.1	1.28
10H-6, 70–72	83.60	33.5	50.3	1.77	1.18	2.79	57.8	1.37
11H-2, 70–72	87.60	33.2	49.8	1.74	1.16	2.65	56.3	1.29
11H-3, 70–72	89.10	33.0	49.1	1.76	1.18	2.71	56.5	1.30
11H-4, 70–72	90.60	32.7	48.6	1.76	1.19	2.71	56.3	1.29
12H-1, 70–72	90.60	33.1	49.4	1.75	1.17	2.70	56.5	1.30
12H-2, 70–72	92.10	34.1	51.7	1.73	1.14	2.71	57.7	1.37
12H-3, 70–72	93.60	38.5	62.7	1.65	1.02	2.69	62.2	1.65
12H-4, 67–69	95.07	35.5	54.9	1.71	1.11	2.72	59.4	1.46
12H-5, 70–72	96.60	34.9	53.7	1.72	1.12	2.72	58.8	1.43
198-1212B-								
12H-1, 70–72	102.40	33.3	49.9	1.75	1.17	2.70	56.8	1.31
12H-2, 70–72	103.90	33.0	49.2	1.75	1.18	2.70	56.5	1.30
12H-3, 80–82	105.50	36.1	56.6	1.70	1.09	2.72	60.0	1.50

Table T12 (continued).

Core, section, interval (cm)	Depth (mbsf)	Water content (wt%)		Density (g/cm³)			Porosity (%)	Void ratio
		Bulk mass	Dry mass	Bulk	Dry	Grain		
12H-4, 70–72	106.90	36.0	56.2	1.71	1.10	2.75	60.2	1.51
12H-7, 50–52	111.20	33.2	49.7	1.77	1.18	2.76	57.2	1.34
13H-1, 50–52	111.70	37.5	59.9	1.67	1.05	2.69	61.2	1.57
13H-2, 70–72	113.28	37.9	61.1	1.67	1.03	2.70	61.7	1.61
13H-3, 84–86	114.92	37.2	59.3	1.68	1.05	2.71	61.1	1.57
13H-4, 70–72	116.28	37.4	59.8	1.68	1.05	2.73	61.5	1.60
13H-5, 70–72	117.78	35.2	54.4	1.72	1.12	2.74	59.2	1.45
13H-6, 70–72	119.28	35.9	56.0	1.70	1.09	2.71	59.7	1.48
15H-1, 70–72	122.20	36.6	57.7	1.69	1.07	2.71	60.4	1.53
15H-2, 70–72	123.70	34.5	52.6	1.74	1.14	2.73	58.4	1.40
15H-3, 70–72	125.20	35.7	55.5	1.72	1.11	2.75	59.9	1.49
17H-2, 70–72	139.24	36.1	56.4	1.71	1.09	2.73	60.1	1.51
18H-1, 70–72	144.40	37.8	60.8	1.67	1.04	2.72	61.8	1.62
18H-2, 70–72	145.53	36.0	56.3	1.71	1.09	2.74	60.1	1.51
18H-3, 70–72	147.03	37.4	59.8	1.68	1.05	2.73	61.4	1.59
18H-4, 70–72	148.53	36.5	57.5	1.70	1.08	2.76	60.7	1.55
18H-5, 70–72	150.03	36.6	57.6	1.71	1.09	2.79	61.1	1.57
18H-6, 70–72	151.53	35.6	55.4	1.72	1.11	2.77	59.9	1.50
19H-1, 78–80	153.98	36.0	56.2	1.70	1.09	2.70	59.7	1.48
19H-2, 70–72	155.40	35.7	55.5	1.70	1.10	2.69	59.4	1.46
19H-3, 70–72	156.90	35.6	55.4	1.71	1.10	2.71	59.5	1.47
19H-4, 70–72	158.40	37.1	58.9	1.69	1.07	2.75	61.3	1.58
19H-5, 70–72	159.90	36.3	57.1	1.71	1.09	2.75	60.5	1.53
20H-1, 70–72	163.40	34.0	51.5	1.74	1.15	2.74	57.9	1.38
20H-2, 70–72	164.90	33.5	50.4	1.76	1.17	2.76	57.6	1.36
20H-3, 70–72	166.40	33.9	51.3	1.74	1.15	2.72	57.7	1.36
23H-1, 98–100	184.68	33.0	49.3	1.76	1.18	2.72	56.7	1.31
23H-2, 70–72	185.85	33.3	50.0	1.75	1.17	2.71	56.9	1.32
23H-3, 70–72	187.35	33.1	49.5	1.76	1.18	2.73	56.9	1.32

Table T13. Discrete measurements of *P*-wave velocity, Site 1212.

Core, section, interval (cm)	Depth (mbsf)	Velocity (m/s)
198-1212A-		
1H-1, 66	0.66	1515.8
1H-2, 67	2.17	1498.5
1H-3, 65	3.65	1489.0
2H-1, 66	5.55	1507.8
2H-2, 66	7.05	1528.3
2H-3, 65	8.55	1519.0
2H-4, 66	10.06	1519.6
2H-5, 66	11.56	1509.3
2H-6, 66	13.06	1523.9
3H-1, 66	15.06	1515.1
3H-2, 66	16.56	1511.1
3H-3, 65	18.05	1515.3
3H-4, 66	19.56	1522.0
3H-5, 66	21.06	1515.9
3H-6, 65	22.55	1512.1
3H-7, 43	23.83	1521.2
4H-1, 82	24.72	1527.9
4H-2, 67	26.07	1516.5
4H-3, 65	27.55	1526.0
4H-4, 65	29.05	1519.3
4H-5, 66	30.56	1503.4
4H-6, 65	32.05	1523.5
4H-7, 65	33.55	1526.3
5H-1, 66	34.06	1527.9
5H-2, 66	35.56	1513.3
5H-3, 65	37.05	1512.2
5H-4, 66	38.56	1517.2
5H-5, 66	40.06	1521.7
5H-6, 65	41.55	1516.6
6H-2, 86	45.26	1518.6
6H-3, 65	46.55	1525.3
6H-4, 76	48.16	1511.3
7H-1, 75	48.15	1528.4
7H-2, 67	49.57	1512.6
7H-3, 76	51.16	1522.3
7H-4, 66	52.56	1511.3
7H-5, 67	54.07	1519.6
7H-6, 76	55.66	1517.6
8H-1, 67	57.57	1505.8
8H-2, 67	59.07	1514.5
8H-3, 67	60.57	1531.6
8H-4, 65	62.05	1537.3
8H-5, 65	63.55	1545.0
8H-6, 66	65.06	1543.4
9H-1, 67	67.07	1553.0
9H-2, 66	68.38	1555.7
9H-3, 66	69.88	1564.5
9H-4, 71	71.43	1552.6
9H-5, 67	72.89	1570.2
9H-6, 67	74.39	1559.6
10H-1, 81	76.71	1539.6
10H-2, 58	77.98	1537.2
10H-3, 45	79.35	1545.3
10H-4, 58	80.48	1540.3
10H-5, 73	82.12	1559.4
10H-6, 58	83.48	1547.3
10H-7, 60	85.00	1555.6
11H-2, 57	87.47	1554.2
11H-3, 59	88.99	1551.6
11H-4, 56	90.46	1547.0
12H-1, 60	90.50	1566.5
12H-2, 73	92.13	1562.1
12H-3, 69	93.59	1543.3
12H-4, 73	95.13	1556.3
12H-5, 69	96.59	1598.6
12H-6, 66	98.06	1639.7
12H-7, 57	99.47	1655.7
198-1212B-		
1H-1, 69	0.69	1519.1
1H-2, 64	2.14	1507.5
1H-3, 60	3.60	1493.1
1H-4, 64	5.14	1507.9
2H-1, 70	7.40	1510.8
2H-2, 63	8.83	1507.3
2H-3, 64	10.34	1516.3
2H-4, 70	11.90	1521.4
2H-5, 67	13.36	1522.1
2H-6, 65	14.85	1517.4
2H-7, 47	16.17	1533.4
3H-1, 67	16.87	1517.0
3H-2, 65	18.35	1530.2
3H-3, 67	19.87	1519.1
3H-4, 70	21.40	1515.7
3H-5, 70	22.90	1526.3
3H-6, 67	24.37	1526.2
3H-7, 42	25.62	1527.6
4H-1, 76	26.45	1504.4
4H-2, 63	27.83	1522.8
4H-3, 66	29.36	1524.8
4H-4, 65	30.85	1515.5
4H-5, 70	32.40	1528.1
4H-6, 69	33.89	1522.7
4H-7, 42	35.12	1526.6
5H-1, 56	35.76	1553.5
5H-2, 66	37.35	1513.5
5H-3, 71	38.91	1518.9
5H-4, 71	40.41	1529.0
5H-5, 70	41.90	1526.3
5H-6, 61	43.31	1521.5
5H-7, 50	44.70	1522.0
6H-1, 62	45.32	1505.3
6H-2, 67	46.87	1524.0
6H-3, 59	48.29	1515.7
6H-4, 59	49.79	1528.2
6H-5, 70	51.40	1526.1
6H-6, 62	52.82	1522.1
6H-7, 25	53.95	1524.1
7H-1, 63	54.83	1506.7
7H-2, 75	56.45	1512.7
7H-3, 95	58.15	1525.7
7H-4, 67	59.37	1520.8
7H-5, 78	60.98	1514.6
7H-6, 77	62.47	1519.0
8H-1, 62	64.32	1545.3
8H-2, 63	65.83	1550.0
8H-3, 63	67.33	1548.6
8H-4, 66	68.86	1547.4
8H-5, 67	70.37	1550.4
8H-6, 72	71.92	1546.9
9H-1, 64	73.84	1550.4
9H-2, 61	75.31	1536.6
9H-3, 67	76.86	1543.4
9H-4, 59	78.29	1547.6
9H-6, 58	81.28	1548.7
10H-1, 62	83.32	1584.5
10H-2, 63	84.83	1581.3
10H-3, 66	86.36	1579.0
10H-4, 65	87.85	1567.1
10H-5, 68	89.38	1564.7
10H-6, 61	90.81	1566.6
11H-1, 64	92.84	1557.4
11H-2, 64	94.34	1557.0
11H-3, 60	95.80	1528.4
11H-4, 59	97.29	1533.1
11H-5, 66	98.86	1585.1
12H-1, 57	102.27	1542.8
12H-2, 57	103.77	1539.9
12H-3, 85	105.55	1537.5
12H-4, 66	106.86	1552.2
12H-7, 45	111.15	1545.6
13H-1, 45	111.65	1510.0
13H-2, 65	113.22	1517.1
13H-3, 91	114.99	1513.1
13H-4, 75	116.33	1523.4
13H-5, 65	117.73	1529.6
13H-6, 65	119.23	1523.1
15H-1, 77	122.27	1533.1
15H-2, 78	123.78	1530.7
15H-3, 77	125.27	1546.1
17H-2, 76	139.30	1531.6
18H-1, 65	144.35	1583.0
18H-2, 67	145.50	1571.3
18H-3, 66	146.99	1532.9
18H-4, 66	148.49	1556.7
18H-5, 67	150.00	1537.7
18H-6, 64	151.47	1560.0
19H-1, 86	154.06	1540.4
19H-2, 67	155.37	1535.3
19H-3, 66	156.86	1535.9
19H-4, 66	158.36	1527.5
19H-5, 66	159.86	1543.5
20H-1, 74	163.44	1554.3
20H-2, 76	164.96	1543.5
20H-3, 75	166.45	1584.8
23H-1, 95	184.65	1572.1
23H-2, 59	185.74	1579.4
23H-3, 60	187.25	1567.2